# SOLUTIONS OF INVERSE CONVECTION PROBLEMS BY A PREDICTOR-CORRECTOR TECHNIQUE

## BY JOSEPH R VANDERVEER

A dissertation submitted to the

Graduate School—New Brunswick

Rutgers, The State University of New Jersey

in partial fulfillment of the requirements

for the degree of

Doctor of Philosophy

Graduate Program in Mechanical and Aerospace Engineering

Written under the direction of

Dr. Yogesh Jaluria

and approved by

_____

_____

_____

_____

New Brunswick, New Jersey

October, 2014

**ABSTRACT OF THE DISSERTATION**

# Solutions of Inverse Convection Problems by a Predictor-Corrector Technique

### by Joseph R VanderVeer
### Dissertation Director: Dr. Yogesh Jaluria

A predictor-corrector technique for solving inverse convection problems was developed, tested, and refined. The methodology was tested against three inverse problems: inverse plume in a crossflow, inverse jet in a crossflow, and inverse plume in a cavity. The goal of the inverse plume in a crossflow was to solve for the strength and location (x, y) of the source. After refinement, the methodology was able to predict all three goals, utilizing three sample points to within 2.5%. Error analysis demonstrated that three sample points was unable to tolerate any simulation-experimental error. Therefore, when handling experimental data, an increase in the number of sample points is required, to a minimum of five. The error analysis also showed that the methodology, with five or more sample points, is remarkably stable in its prediction capability. The location prediction was minimally affected, less than 0.1%, by an artificial error of 10%. The goal of the inverse jet in a crossflow was to solve for the strength (velocity and temperature) and location (x, y) of the source. After testing, the methodology was not able to predict all four goals. The elevation location of the jet needed to be known to adequately solve the inverse problem. The methodology was able to predict the source velocity and temperature to within 10% and 3.3% respectively. The goal of the inverse plume in a cavity was to find the strength and location (x, y) of the source.

Sensitivity analysis demonstrate it is very difficult, if not impossible, to resolve source location using this methodology. The method was able to predict the source strength within 5% using only one sample point. With future work, this approach could be extended to applied areas of interest, such as environmental flows, room fires, and thermal management systems.

# Acknowledgements

I want to thank those that have made this possible. William Doig for his insistent questions of when I'm graduating, it always pushed me a little more. Kevin Gomes for helping me with my classes. John Petrowski for his unrelenting encouragement and assistance. Dr. Rhee for pushing me to want to continue with my studies. Dr. Jaluria for allowing me to work under his tutelage. Thank you April Barillari for proof reading the endless nonsense that eventually made this comprehensible.

The work contained in this text was previously published in [43–45]. The bulk of which is presented in chapters 3 to 5.

# Dedication

To the ones whom lifted my spirits when all seemed lost, Bill and April.

# Table of Contents

# List of Tables

# List of Figures

# Nomenclature

Latin Letters

| | |
|---|---|
| $\alpha, Re_t, R_k, R_\omega, \sigma_k, \sigma_\omega, R_\beta, \beta_i$ | $k - \omega$ model coefficients |
| $\boldsymbol{r}$ | vector location of sampled points |
| $\Gamma_2, \Gamma_1, \Gamma_0$ | model parameters |
| $a$ | number of sample points used in the predictor stage |
| $b, m$ | model parameters |
| $C_1, C_2, C_{1\epsilon}, C_\mu, \sigma_k, \sigma_\epsilon$ | $k - \epsilon$ model coefficients |
| $C_P$ | specific heat at constant pressure |
| $D$ | jet width |
| $d$ | number of simulations |
| $E$ | thermal energy |
| $F$ | minimization function for temperature |
| $f_{\nu 1}, f_{\nu 2}, \chi, C_{\nu 1}, C_{b1}, C_{b2}, C_{w1}, C_{w2}, C_{w3}, \kappa$ | Spalart Allmaras model coefficients |
| $G$ | minimization function for velocity |
| $Gr$ | Grashof number |
| $I$ | turbulence intensity |
| $k$ | turbulence kinetic energy |
| $l$ | turbulence length scale |
| $M_W$ | molecular weight |
| $n$ | number of sample locations |
| $P$ | pressure |
| $P_{rt}$ | turbulent Prandtl number |
| $R^2$ | coefficient of determination |
| $Ra$ | Rayleigh number |
| $Re$ | Reynolds number |
| $Ri$ | Richardson number |
| $S, \Omega$ | rate of strain tensor and vorticity tensor |
| $T$ | temperature |
| $t$ | time |
| $U$ | free stream velocity |
| $u, v$ | velocity components |
| $X, Y$ | normalized coordinates |
| $x, y$ | coordinates |
| Bi-CGM | bi-conjugate gradient method |
| CFD | computational fluid dynamics |
| CGM | conjugate gradient method |
| DDDAS | dynamic data driven application systems |
| DNS | direct numerical simulation |

| | |
|---|---|
| GA | genetic algorithm |
| IBVC | initial value, boundary condition |
| IHTP | inverse heat transfer problem |
| NIST | national institue of standards and technology |
| RANS | Reynolds averaged Navier-Stokes |
| TSVD | truncated singluar value decomposition |
| XPS | extruded polystyrene |

**Greek Letters**

| | |
|---|---|
| $\boldsymbol{\delta}$ | vector distance between actual sampled location and the current test location |
| $\Delta$ | relative difference between the first sampled point and other sampled points |
| $\epsilon$ | error or turbulence dissipation rate |
| $\lambda$ | thermal conductivity |
| $\mu$ | dynamic viscosity |
| $\mu_t$ | eddy viscosity |
| $\Omega_\mu$ | collision integral for viscosity |
| $\phi$ | cell value or normalized temperature $\phi = \frac{T - T_\infty}{T_S - T_\infty}$ |
| $\rho$ | density |
| $\sigma, \epsilon/k$ | Lennard-Jones parameters for the Chapman-Enscog equations |

**Superscripts**

| | |
|---|---|
| $\prime$ | instantaneous |
| $-$ | ensemble averaged |
| $*$ | predictor stage, alternative heat flux eqn. |

**Subscripts**

| | |
|---|---|
| $0, 1, 2$ | sample point indexes |
| $\infty$ | free stream |
| $A, B$ | data set A,B |
| $f$ | face |
| $i, j, k$ | index |
| $j$ | jet |
| $mod$ | modified |
| $o$ | optimized |
| $P$ | predicted |
| $S$ | source |
| $T$ | temperature |
| $U$ | velocity |

# Chapter 1

# Introduction

Modern thermal systems are more complicated than ever before. Whether these systems are building ventilation units or internal combustion engines, understanding the internal physical phenomena is paramount to high energy efficiency and safety. From new experimental diagnostics to concurrent computer simulation-experiment methods have been developed to enhance our understanding of the underlying physics of thermal systems [20, 24].

Traditional heat transfer problems are forward type, but many thermal problems are of the inverse heat transfer type. These problems often require novel means of finding a solution. One such example of an inverse heat transfer problem is determination of the wall temperature of an optical fiber draw tower furnace.

Issa et al. [23] wanted to determine the internal wall temperature of an optical fiber draw tower furnace. Measuring the wall temperature directly is difficult due to limited accessibility, geometry, and high temperatures. The only easily accessible furnace location is where the optical fiber is drawn, the centerline of the cylindrical furnace. An instrumented ceramic rod was set to measure the centerline temperature. This, however, is an inverse heat transfer problem. Knowing the centerline temperature, Issa et al. [23] was able to use a regularization technique to accurately predict the boundary conditions (i.e. the furnace wall temperature) [23].

## 1.1 Ideal Inverse Heat Transfer Solution

A traditional forward heat transfer problem solves the energy equation in a direct fashion, utilizing initial conditions and boundary values. The inverse problem uses incomplete or limited information about the problem domain, boundary conditions,

and/or initial conditions to solve for the complete boundary conditions and/or the initial conditions. This situation is ill-posed and traditional mathematics fail [41].

In 1902, Jacques Hadamard defined the well-posed problem as a problem with a continuous unique solution [14]. Other than a very firm mathematical definition this definition remains unchanged [42]. Tikhonov and Arsenin [41] defines a well-posed problem as: for $y = F(x)$

1. for every $x$ there must exist a solution $y$

2. the solution is unique

3. the problem is stable on the space $F$

Any problem not strictly adhering to these rules is considered ill-posed [41], which is often also the case with the inverse heat transfer problem. The ideal inverse heat transfer solution is a direct consequence of the ill-posed nature of the problem.

The ideal inverse heat transfer solution would have a methodology applicable to 100% of cases, converting the ill-posed problem into a well-posed problem utilizing one data point within the domain or on the domain boundary. This extreme idealization should not be seen as a goal, but a motivation.

## 1.2  Engineering Motivation

The inverse heat transfer problem (IHTP) is of interest to many engineering disciplines. Such problems include: estimation of heat source strength in a forced convection duct, estimation of the temperature of a heat shield during space vehicle atmospheric reentry, estimation of heat generation due to friction, etc... [37]

Unfortunately, the ideal inverse heat transfer solution does not exist. There are many methods to solving IHTPs, and they are classified into fifteen categories or combination of categories [37]. There have been many books written on the subject [36, 37, 41, 42]. Two popular categories are Tikhonov regularization and conjugate gradient method ([4, 8–10, 34]).

The inverse heat convection problem, covers topics such as: determining the location of fires in rooms, locating a fire in a vehicular tunnel, tracking pollutants back to their source, tracking fires in an urban environment, etc... [6, 7, 19, 36].

## 1.3   Previous Work

Examining previous work starts with an investigation into a relatively new capability made available due to the ever increasing processing power of computers, dynamic data driven application systems. Powerful modern computers open a new realm of investigation, a combined experimental-numerical solution brought together intelligently using parameters and suggestions from previous iterations. The new technique is "Dynamic Data Driven Application Systems" or DDDAS. The topic of interest for Ma et al. [29] was the inverse jet in a crossflow problem.

Laser light at $761\,nm$ is absorbed by oxygen at a rate, which is a function of the oxygen temperature within the flow. Utilizing this knowledge the linearly integrated temperature can be determined within the wind tunnel by passing light from a diode laser through the wind tunnel and measuring the resulting intensity on the other side [29].

The methodology was to select a series of monitored locations within the simulation set. A response surface model would be generated based upon the monitored location simulation data. A small subset of monitored locations would be chosen for experimental monitoring. Using the response surface model, the source velocity and temperature would be predicted. From the prediction, a new set of experimental monitoring locations would be determined, and a new set of predictions would occur. More experimental monitoring locations may be used if necessary, however, during the process Knight et al. [25] did not proceed passed a second iteration.

Using this method Knight et al. [25] were able to predict the jet velocity to within the experimental accuracy. However the jet temperature proved a little more elusive, with error of the first pass jet temperature prediction of 9% and the second pass of 23%. This method demonstrates its fundamental capabilities while showing its flaws. That

being said, many capable methods exist for solving the inverse heat transfer problem, all of which have a list pro et contra

### 1.3.1  Literature Survey

Inverse heat transfer is a relatively new field in engineering, but that does not mean there is a shortage of methods and solutions to the inverse problems. Methods start with a mathematical model designed to solve inverse problems, then force the physics to fit the model. Alternatively, some methods start with the physics and attempt to massage a mathematical model onto the physics.

Many solution methods have been developed for the solution of the inverse heat transfer problems. For example, Beck et al. [4] compared the capabilities of the function specification method, Tikhonov's regularization, iterative regularization, and Green's functions for the case of an inverse conduction problem. The setup consists of a symmetric system with a central mica heater covered with a carbon-carbon composite layer and a thick ceramic insulation. The goal was to calculate the transient input heat flux with two thermocouples located at the heater - composite layer and at the composite - insulation layer. They note that each of the methods tested were equally capable in effectively predicting the time varying heat flux, but differed vastly when considering the computation time. The function specification method was marginally quicker, and vastly easier to program than the iterative regularization method. The iterative regularization method and Tikhonov's regularization method proved to be equally difficult to program, but the iterative method was between two and four times faster. The Green's functions were significantly slower and more difficult to program than all the other methods.

Similarly, Erturk et al. [9] tested several methods developed for the solution of inverse radiation problems. The methods they tested were the conjugate gradient method or CGM, biconjugate gradient method or Bi-CGM, and truncated singular value decomposition or TSVD. The methods were used to solve a set of Fredholm equations of the first kind, a known ill-posed problem. CGM and the truncated singular value decomposition tended to be quicker, less memory intensive, easier to program, and more

accurate than the Bi-CGM. However, CGM and the TSVD would fail in certain cases where the Bi-CGM would usually give meaningful results.

CGM was applied to the inverse boundary conditions of a thermometry test bed by Erturk et al. [10]. The test bed consists of an axi-symmetric vacuum chamber designed to reproduce the rapid thermal process used in silicon wafer processing. Due to the vacuum environment and thermal conductivity insulation the problem is primarily thermal radiation only. The inverse predictions were less than 3.5% error of the boundary condition temperature.

Continuing with the conjugate gradient theme, it is a very popular and effective means for solving inverse convection problems as well (e.g. [17, 28, 38, 49]). Zhao et al. [49] used CGM to solve the IHTP of a slot vented differentially heated enclosure with mixed mode heat transfer. They were able to accurately predict the input heat flux, but had difficulty resolving the solution when the Reynolds number or Richardson number became large. Follow up work by Liu et al. [28] refined the effective limits to a Grashoff number below $10^{10}$.

Hong et al. [17] used CGM to solve the IHTP of a differentially heated enclosure with constant temperature walls. They showed that even within the small confines of the problem $(0.1\,m \times 0.1\,m)$, that at least nine samples were needed to accurately resolve the input heat flux. However, even for the case of nine samples the accuracy of the method went down, because the samples were further away from the heat source.

Park and Chung [38] used CGM to attempt to solve a convection IHTP with a transient heat flux source in an enclosure. They were able to accurately resolve the transient source, but the solution required 400 sample points and as many as 100 iterations.

An alternative to the already mentioned methods is the artificial neural network, which was used successfully by Ghosh et al. [13], and Kumar and Balaji [26]. Ghosh et al. [13] inversely solved for both the source strength and location of a circular source within a rectangular cavity. The only a priori knowledge was temperature from four thermocouples located near each corner.

Kumar and Balaji [26] demonstrated that the artificial neural network could be

applied to inverse convection problems as well. The inverse convection problem was a differentially heated rectangular enclosure with unknown heat flux in and a constant temperature wall. The neural network required many simulation sets to train the three layers of twenty neurons each network and a set of 124 thermal sample points within the domain. The major advantage this method has over the alternatives is that after the neural network is thoroughly trained, it is a non-iterative solver and thus, is generally quicker.

## 1.4  Present Work

The overall goal of this work is to develop a method for solving inverse convection problems where the location of the source is unknown. To eventually make the method most useful for finding and tracking fires, it must use a limited amount of sampled data, a limited amount of simulation data, handle experimental error, and lastly work "far" downstream of the source.

The work focus's on the development, progress, optimization, and lastly, testing of the methodology. The development starts with a simpler case than previously used, but with the goal of finding the location as well. The methodology is applied three separate, but similar inverse convection problems. Some of the methodologies' capabilities and limitations are demonstrated and discussed.

### 1.4.1  Chapter Layout

The next chapter covers the inverse heat transfer problem in a general sense. The chapter covers the difficulties of inverse heat transfer problems as well as a few of the broad approaches successfully used previously.

Chapter 3 covers the complete development of the methodology from the very beginning to its final form. The optimization of the search shape is covered in chapter 4.

Three example problems demonstrate the capability of the methodology. The plume in a crossflow is described in chapter 5. Chapter 6 covers the jet in a crossflow. Lastly, chapter 7 describes the plume in a sealed chamber.

Chapter 8 is the last of the main text covering the conclusions.

The appendix starts with the equations and setup of the computation fluid dynamics used in appendix A. Next, is a chapter on the calibration of the experimental apparatus in appendix B. Appendix C covers the data acquisition hardware and software. In appendix D describes the options and configurations of the Matlab genetic algorithm used in the methodology. The last chapter in the text is appendix E and covers experimental plume data. The last pages are of the bibliography.

# Chapter 2

# The Inverse Heat Transfer Problem and Solutions

The problem with inverse solutions arises from the forward problem's mathematical model of the underlying physics. Simpler mathematical models allow one to rewrite the equation such that a discrete inverse solution is easily (or relatively so) attainable. Such as:

$$y = f(x) \tag{2.1}$$

$$x = f^{-1}(y) \tag{2.2}$$

Where $f^{-1}$ is defined as the inverse of $f$. For the more complicated case of differential equations, the exact equation $f^{-1}$ is impossible to solve for without initial values and boundary conditions. Even with the initial values and boundary conditions known, it is still unlikely to be possible to solve for the exact solution $f^{-1}$. Often we must settle for an approximate solution to the inverse problem.

## 2.1 Infinite Solutions

To make matters worse, the inverse solution (if it can be found) may have an infinite number of solutions to the initial values and boundary conditions. This results in an ill-posed problem. Fortunately, mathematicians have been working on this problem for many decades.

## 2.2 Fifteen Options

Ozisik and Orlande [37] determined that there are fourteen effective (loosely grouped) methods for solving inverse heat transfer problems. A newer method should be added to their list, that being the artificial neural network. The rapid development of faster

computers has spurred research into the areas needing more computational processing power, such as iterative regularization or genetic algorithm. The methodology proposed in this text utilizes features from many of these options, making it difficult to classify. The basis of the inversion is an interpolation of a polynomial, but requires an additive term like that of the Tikhonov's regularization. However, the minimization occurs via a genetic algorithm and for this this method must be classified into the genetic algorithm regularization option.

1. Integral Equation Approach

2. Integral Transform Technique

3. Series Solution Approach

4. Polynomial Approach

5. Hyperbolization of the Heat Conduction Equation

6. Numerical Methods (Finite Difference, Finite Element, etc...)

7. Space marching Techniques

8. Iterative Filtering Techniques

9. Steady State Techniques

10. Beck's Sequential Function

11. Levenberg-Marquardt Method

12. Tikhonov's Regularization

13. Iterative Regularization

14. Genetic Algorithm Regularization

15. Artificial Neural Network

## 2.3 Regression Analysis

The basis of many of the inverse heat transfer methods, including Tikhonov's regularization and genetic algorithm regularization, is a form of regression analysis. Regression analysis is the statistical method for determining the relationship between variables. An M - estimator is a type of regression analysis method for minimizing (although originally developed for maximizing) residuals of a function. Probably the most well known and most used M - estimator is the least squares method, which is a minimization of the square of residuals. A paper by Zhang [48] discusses several M - estimators and other regression analysis methods, their effectiveness and their robustness. Table 2.1 shows a few sampled regression algorithms.

Classical statistical methods tend to have problems accurately fitting data with outliers. Even as little as one outlier can adversely affect the outcome. The field of robust statistics is a field of statistics specifically developed to minimize the affects of outliers [30].

| Regression Method | Formula | Comment |
|---|---|---|
| least squares | $min \sum_i (r_i^2)/2$ | not robust, but stable |
| least absolute | $min \sum_i |r_i|$ | not stable |
| Cauchy | $min \sum_i \frac{c^2}{2} log \left( 1 + (r_i/c)^2 \right)$ | theory errors |
| least median of squares | $min \, median_i \, r_i^2$ | stable, robust, poor variance |

Table 2.1: Regression analysis methods

The least squares method is by far the most common, but demonstrates a very poor response to outliers. However, it is extremely stable and since it does not discard any data, is useful for very small sets of data.

The least absolute method is very robust, but unfortunately the method is unstable due to its discontinuity in its first derivative. This may cause the solution to become indeterminate. The Cauchy method is extremely stable and robust. However, the Cauchy method's weighting function tends to be more lenient on very bad outliers and thus may have a large effect on the result.

The least median of squares method is stable, robust, and tends to do poorly with extremely noisy data sets. This poor result is due to the nature of the median function and discards a significant amount of information.

Due to the requirements of having as minimal sampled data as possible the least squares method will be used, since it is stable and does not throw out any data. If the quantity of data needs to increase it may be prudent to consider alternative options, such as the least median of squares.

## 2.4    Conjugate Gradient Method (cgm)

The conjugate gradient method is a special form of an iterative regularization, which deserves brief special attention as it is an especially effective method for solving the inverse heat transfer problem. CGM was originally developed to solve a system of linear equations, similar to the Gaussian elimination. The major benefit of CGM is its ability to solve the equations quickly and accurately, even if the set of linear equations was exceptionally large. The method monotonically approaches the solution with each advancing iteration, which permits solutions as accurate as needed. This is in contrast to the Gaussian elimination, which does not monotonically approach the solution and thus needs to be solved completely to have an accurate result [15].

The conjugate gradient method utilizes a stepping method in orthogonal directions. The length of the step is the location where the gradient becomes zero in the direction of the step. At which point the method makes a new step orthogonal to the previous. This process repeats until the step is a very small value.

While it is relatively easy to program CGM, it requires both the the function and the first derivative of the function of which you are interested in searching. The inverse convection problems of interest we have neither and thus CGM cannot be used.

## 2.5    Regularization Parameters

Tikhonov's regularization uses a parameter to assist in determining the inverse solution. The regularization parameter is related to the subset of all possible solutions, not just

the correct solution. Determining said parameter is difficult often requiring knowledge of the correct solution a priori. If similar inverse problems arise the parameter may be used again.

In this case however, it is easier to use the genetic algorithm to make guesses at possible solutions, than actually trying to determine the regularization parameter. Luckily the exact value of the parameter has no bearing on the methodology of which will be explained in the next chapter.

# Chapter 3

# Methodology

For the methodology to be useful, it needs to accurately solve the inverse heat transfer problem in a variety of conditions. The problem the methodology was developed for is the inverse plume in a crossflow. The only information known a priori is the free stream velocity and temperature, which means the plume location ($\boldsymbol{r}_S$) and plume strength ($T_S$) are unknown. The flow configuration is briefly shown here in figure 3.1, all dimensions are in millimeters. The depth into the page is $305\,mm$ and the flow is upto a maximum of $5.0\,m/s$. The heated section has a maximum temperature of $450\,K$. A full description of the problem and experimental setup is explained in chapter 5.

## 3.1 Initial Development

The development of the methodology starts with the assumption that we can neglect variations in density and thermal buoyancy effects in the energy equation[1]. Due to this

---

[1]A significant portion of this chapter was rewritten from [44]
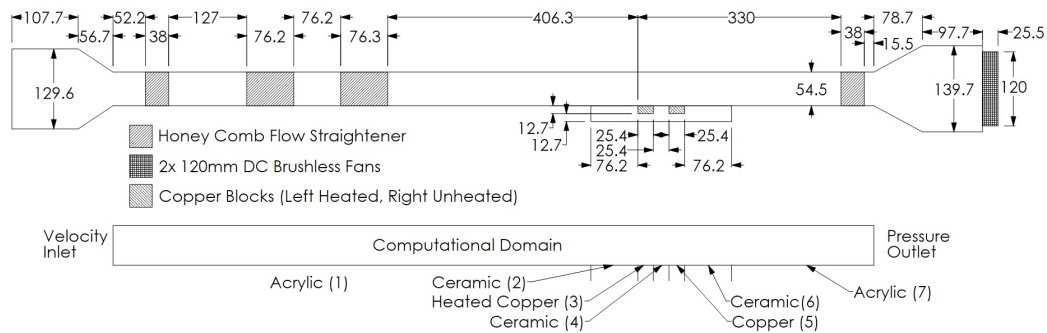


Figure 3.1: Schematics of the wind tunnel and the computational domain [43]

assumption, the energy equation becomes decoupled from the continuity and momentum equations. The net result is that the relation between the source temperature and the local static temperature becomes linear if thermal radiation is negligible. Equation (3.1a) demonstrates this relation. $m$ and $b$ are inverse interpolation functions and are defined in equations (3.1b) and (3.1c), where $A$ and $B$ indicate different simulation conditions. While $m$ and $b$ are linear regression parameters for $T_S$ and $T(\boldsymbol{r})$, the values for each location $\boldsymbol{r}$ can vary significantly. An example of how the functions $m(\boldsymbol{r})$ and $b(\boldsymbol{r})$ vary is shown in figures 3.2 and 3.3. The equations are all vector based and the methodology was originally developed with only two dimensions in mind, such as equation (3.1d).

$$T_S = m\left(\boldsymbol{r}\right)T\left(\boldsymbol{r}\right) + b\left(\boldsymbol{r}\right) \tag{3.1a}$$

$$m\left(\boldsymbol{r}\right) = \frac{T_{SA} - T_{SB}}{T_A\left(\boldsymbol{r}\right) - T_B\left(\boldsymbol{r}\right)} \tag{3.1b}$$

$$b\left(\boldsymbol{r}\right) = T_{SA} - m\left(\boldsymbol{r}\right)T_A\left(\boldsymbol{r}\right) \tag{3.1c}$$

$$\boldsymbol{r} = r\left(x, y\right) \tag{3.1d}$$

$$\boldsymbol{r}_i = \boldsymbol{r}_0 + \boldsymbol{\Delta}_i \tag{3.1e}$$

The assumption of neglecting variations in density and thermal buoyancy is reasonable if the resulting relationship between source temperature and local static temperature is linear. A sensitivity analysis was performed with constant source temperature versus the local static temperature at various free stream velocities. The results at a random location within the flow $\boldsymbol{r} = (50\,mm,\, 4\,mm)$ can be seen in figure 3.4. While this plot is of one particular location, all locations within the domain have a coefficient of determination of $R^2 = 1 - 10^{-6}$ or better. This indicates a near perfect linear regression across the entire domain, thus justifying the original assumption.

## 3.2    Development of Unknown Location

The application of equation (3.1a) lets you solve the inverse problem directly if you know the location of the heat source with respect to the location of the sampled local
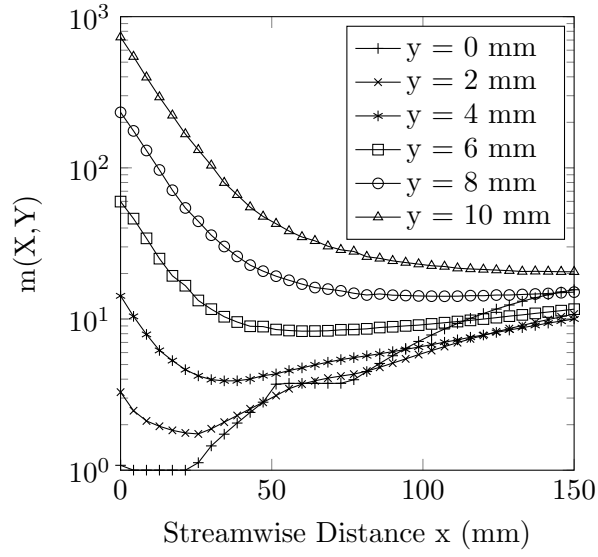
Figure 3.2: Function $m(x,y)$ along the stream-wise direction, for $T_S = 425\,K$, $U_\infty = 0.6\,m/s$
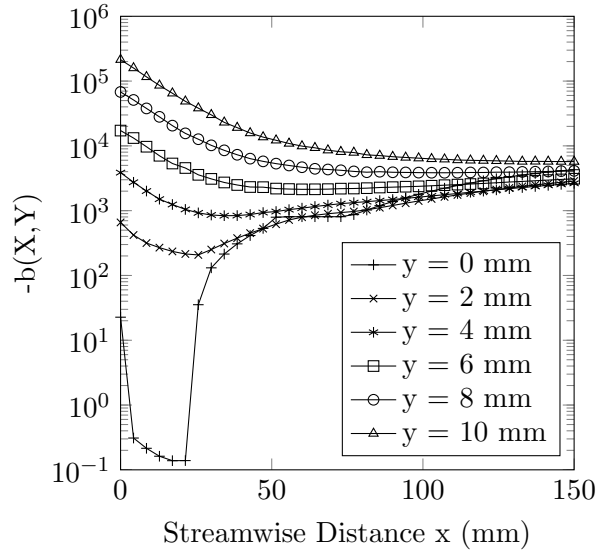


Figure 3.3: $Function - b(x,y)$ along the stream-wise direction, for $T_S = 425\,K$, $U_\infty = 0.6\,m/s$
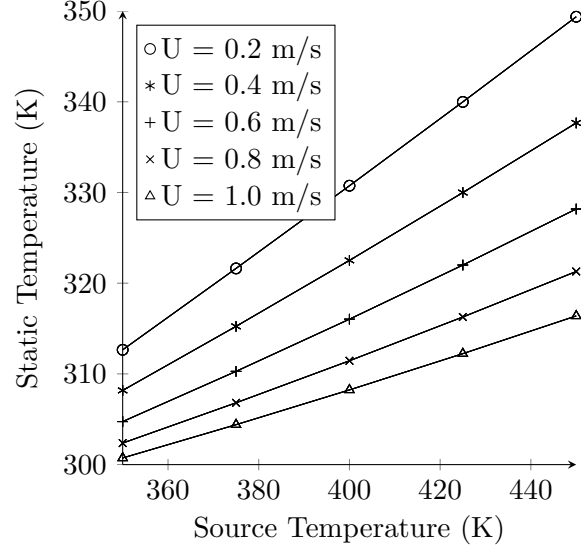
Figure 3.4: Sensitivity analysis: Constant source temperature vs local temperature at $x = 50\,mm$, $y = 4\,mm$

temperature. However, if the location is not known, then the problem becomes more difficult. To clarify the following text, a few definitions are needed.

- sample point: local static temperature from within the domain at a particular location

- datum point: a selected sample point whose location will be defined as $\boldsymbol{\Delta}_0 = (0\,mm,\ 0\,mm)$

- search shape: relative location and pattern between a set of sample points and a datum point

- error map: source temperature error as a function of datum point location

- source strength: temperature of a plume, or temperature and velocity of a jet

**Conjecture 1** *If a domain is not self-similar in local static temperature, then a search shape of sufficient size has only one location where that pattern predicts the same source temperature for all sample points.*

This conjecture is mathematically very difficult to solve, however, evidence based proof will be demonstrated along with the procedure to apply it. The easiest way to demonstrate how this idea may work is that we can look at the error associated with source temperature when we predict a wrong location, i.e. an error map. A sample error map for a single sample point is in figure 3.5. The error is calculated using equation (3.2). From this figure we can see that there are several locations where the error decrease significantly and indicate a local solution. Since the goal is to converge on the correct solution, we try adding more sample points in an attempt to reach that goal. How an error map is calculated is discussed in detail in section 4.2.

$$error_{temp}(\%) = \frac{T_{SP} - T_S}{T_S - T_\infty} \times 100 \tag{3.2}$$

Figure 3.6 shows a new error map with two sample points. The multitude of false local solutions was not reduced, however, the error near these local solutions has significantly increased. This decreases the likelihood that these solutions will be converged to. This is better than the error map shown in figure 3.5, but still not guaranteeing a unique solution. If we take this to the next logical step of three sample points, we end up with figure 3.7. At three sample points the number of local solutions is decreased slightly. Four sample points (figure 3.8) significantly reduces the number of possible solutions (three in this case). Five points typically results in a unique solution, however this is not always the case. In this particular case, as shown in figure 3.9, there is a small second point of convergence possible, and thus the solution is not completely unique. The error map for six and seven data points was not particularly useful as the contour plot was too small to be readable. However, the results were that with seven data points, a unique solution was always possible in the domain of interest.

Thus far, nothing has been said about the shape of the "search shape". The preceding figures all used the same search shape. That shape is in the form of an 'L' with $1\,mm$ spacing, as shown in figure 3.10. The methodology was originally developed with this search shape. The topic is discussed further in chapter 4.
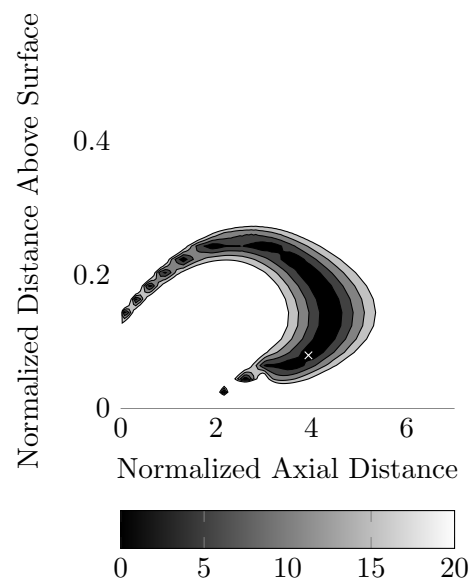
Figure 3.5: Contours of source prediction error, utilizing 1 point of information indicated by the 'x' (% error)
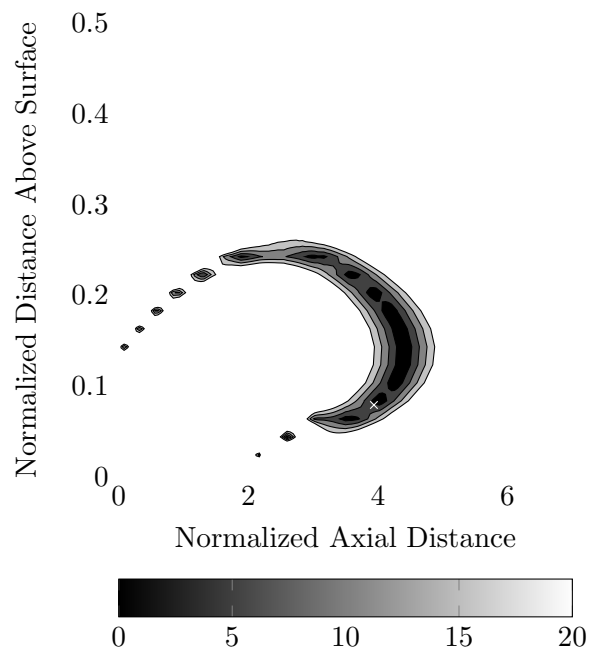


Figure 3.6: Contours of source prediction error, utilizing 2 sample points, 'x' indicating the datum point (% error)
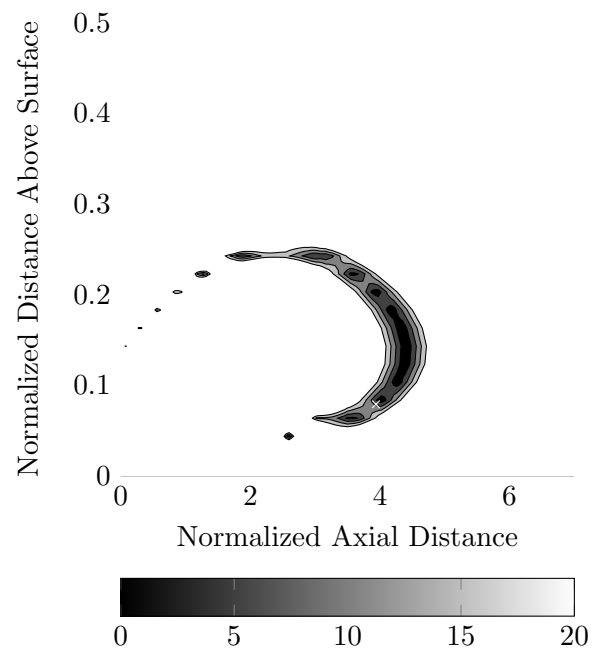
Figure 3.7: Contours of source prediction error, utilizing 3 sample points, 'x' indicating the datum point (% error)
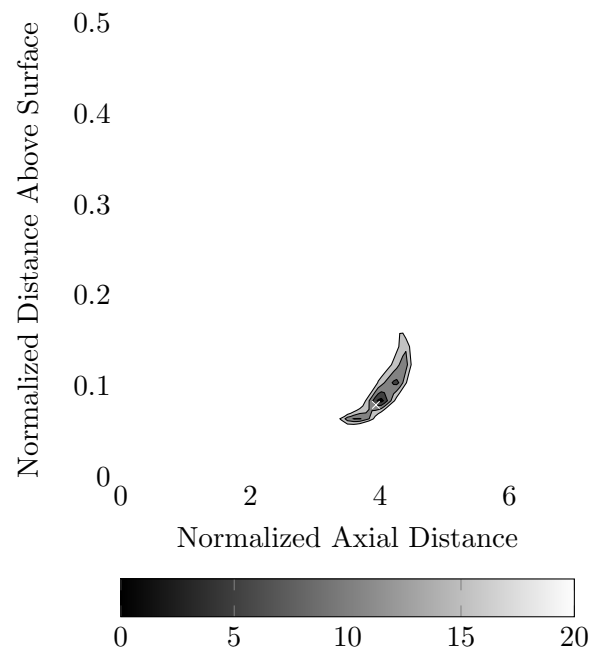


Figure 3.8: Contours of source prediction error, utilizing 4 sample points, 'x' indicating the datum point (% error)
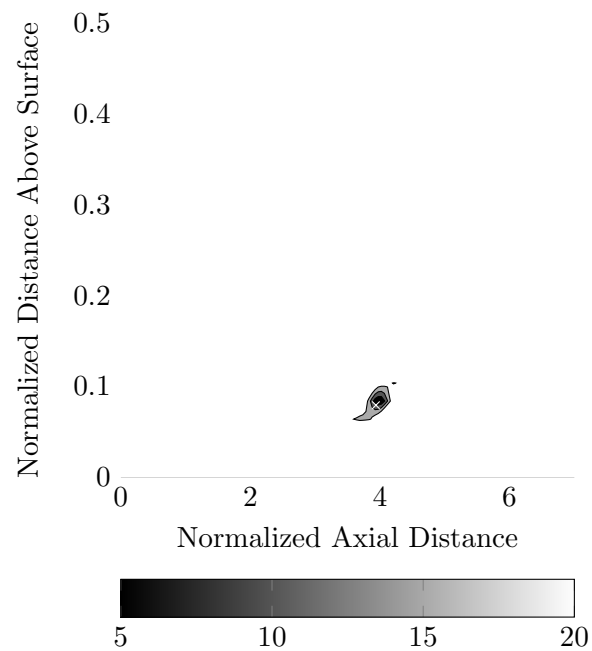
Figure 3.9: Contours of source prediction error, utilizing 5 sample points, 'x' indicating the datum point (% error)
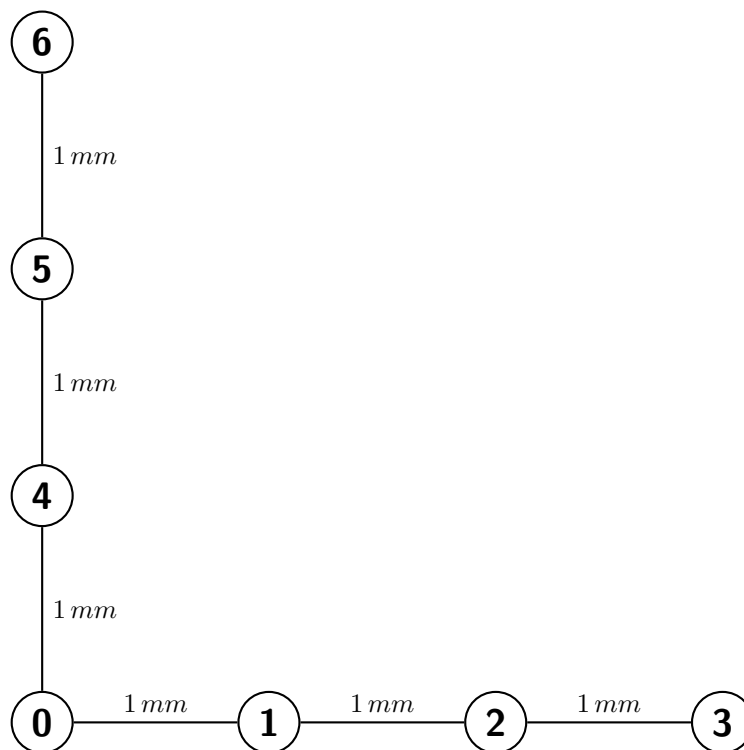


Figure 3.10: Original search shape

## 3.3    Predictor - Corrector Approach

In an effort to reduce the total number of sample points $n$, the methodology was divided into two steps, the predictor and the corrector steps. This approach first utilizes a set of $a$ sample points to determine an approximate source temperature. The corrector step then utilizes the rest of the sample points $n - a$ to "correct" the source temperature and predict the source location.

The predictor step starts by minimizing equation (3.3). The solution to the minimization of equation (3.3) happens to be the mathematical description of conjecture 1. Since the possibility of local minimums is significant, a global minimization method must be used, such as the genetic algorithm [35]. Using the intermediate location, $\boldsymbol{r}_{SP}^*$, we can use equation (3.4) to solve for the intermediate source temperature $T_{SP}^*$. Equation (3.4) is nothing more than a sample averaged version of equation (3.1a).

The equation (3.3) is then modified to handle the new information from the predictor step, resulting in equation (3.5). The corrector step then utilizes $T_{SP}^*$ to find the solution to the minimization of equation (3.5), which should be the source location $r_{SP}$. Finally, to solve for the source temperature a similarly modified equation (3.6) may be used.

$$F\left(\boldsymbol{r}\right) = \sum_{i=1}^{a}[m\left(\boldsymbol{r} + \boldsymbol{\Delta}_i\right)T\left(\boldsymbol{r}_i\right) + b\left(\boldsymbol{r} + \boldsymbol{\Delta}_i\right) - m\left(\boldsymbol{r}\right)T\left(\boldsymbol{r}_0\right) - b\left(\boldsymbol{r}\right)]^2 \qquad (3.3)$$

$$T_{SP}^* = \frac{1}{a}\{\sum_{i=0}^{a}[m\left(\boldsymbol{r}_{SP}^* + \boldsymbol{\Delta}_i\right)T\left(\boldsymbol{r}_i\right) + b\left(\boldsymbol{r}_{SP}^* + \boldsymbol{\Delta}_i\right)]\} \qquad (3.4)$$

$$F_{mod}\left(\boldsymbol{r}\right) = \sum_{i=a}^{n}[m\left(\boldsymbol{r} + \boldsymbol{\Delta}_i\right)T\left(\boldsymbol{r}_i\right) + b\left(\boldsymbol{r} + \boldsymbol{\Delta}_i\right) - T_{SP}^*]^2 \qquad (3.5)$$

$$T_{SP} = \frac{1}{n - a}\{\sum_{i=a}^{n-a}[m\left(\boldsymbol{r}_{SP} + \boldsymbol{\Delta}_i\right)T\left(\boldsymbol{r}_i\right) + b\left(\boldsymbol{r}_{SP} + \boldsymbol{\Delta}_i\right)]\} \qquad (3.6)$$

## 3.4    Procedure

The procedure starts with acquiring $n$ sample points from the domain. From there, the sample points are divided into two groups of size $a$ and $n - a$. A datum point is arbitrarily chosen from the first set of sample points and is given the identifier '0'. A set of $d$ simulations need to be performed, spanning the thermal domain of interest. Once
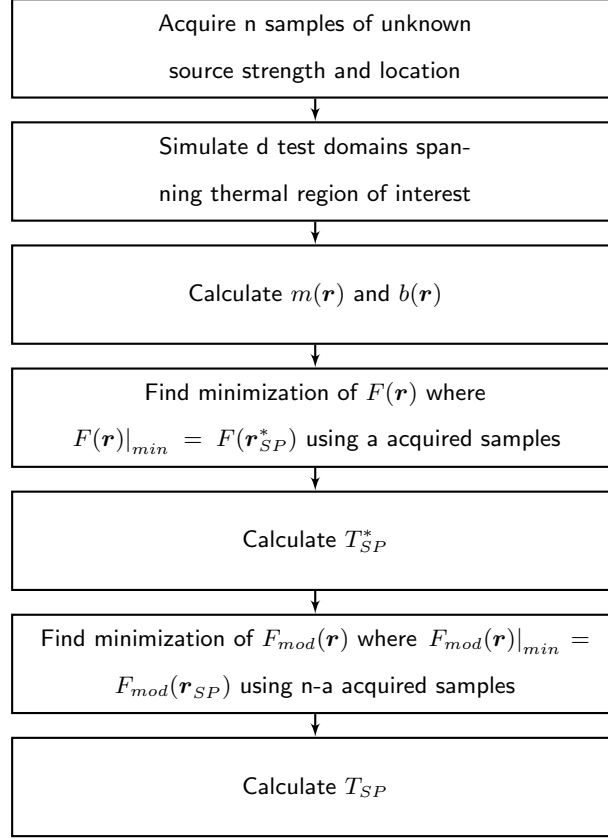
Figure 3.11: Flow chart of the predictor - corrector methodology

this is achieved, we can calculate the inverse interpolation functions $m(\boldsymbol{r})$ and $b(\boldsymbol{r})$ for the entire physical domain. The size of the groups is typically such that $a = n - a$, to ensure that both the predictor and corrector halves always have data to work with.

We can then use the predictor - corrector approach previously described. First, find the solution to the minimization of equation (3.3), followed by calculating the intermediate source temperature from equation (3.4). Then, find the solution to the minimization of equation (3.5), which should be the source location. Lastly, calculate the source temperature from equation (3.6).

A simple flow chart depicting these steps is presented in figure 3.11.

# Chapter 4

# Search Shape

The search shape as defined previously is the relative location and pattern between a set of sample points and a datum point. The search shape effectively determines the accuracy and capabilities of the described methodology, and as such, a significant effort went into determining what is the most effective search shape. Unfortunately, intuition does not indicate what should be chosen for the search shape, other than some form of separation in all dimension wishing to be resolved. The simplest place to start would be to do a sensitivity analysis.

## 4.1 Sensitivity Analysis

A simple sensitivity analysis was performed, comparing the number of sample points and spacing versus the strength and location error of the solution[1]. Figure 4.1 is a plot of perpendicular spacing versus error in the plume source strength. Figure 4.2 is nearly identical, but with axial spacing. The predicted source temperature error tends to be larger in the perpendicular case than it is in the axial case. This trend led the use of a axial arrangement of sample points for predicting the source temperature.

Figures 4.3 and 4.4 are similar to the previous two figures, but these are for the error in location prediction. The location prediction error in the axial direction is very erratic, which led to the decision to use the perpendicular direction even though the axial direction may give slightly better results.

From the figures 4.1 to 4.4, the decision was made to use four sample points in the axial direction at $1\,mm$ spacing, and four sample points in the perpendicular direction

---

[1]A significant portion of this section was rewritten from [43]
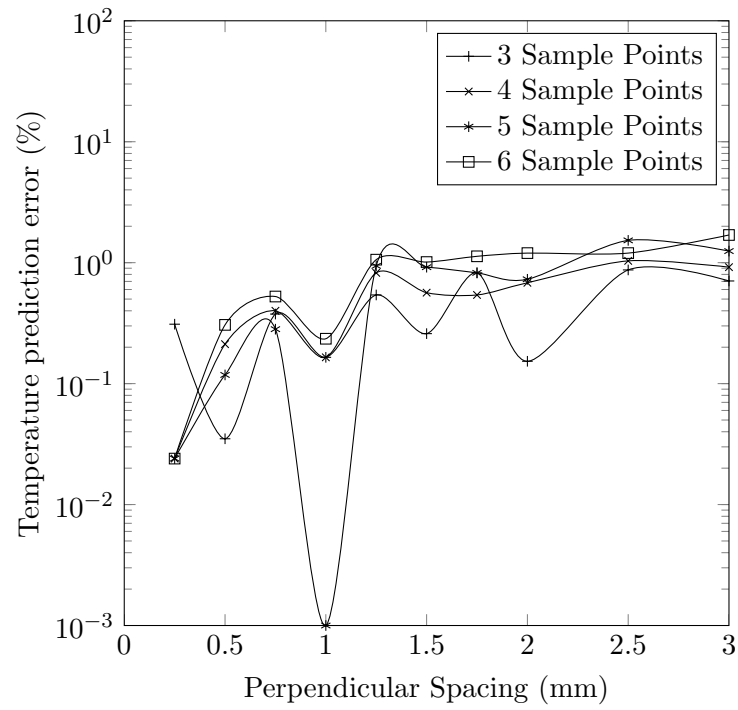
Figure 4.1: Temperature prediction error vs perpendicular spacing between samples
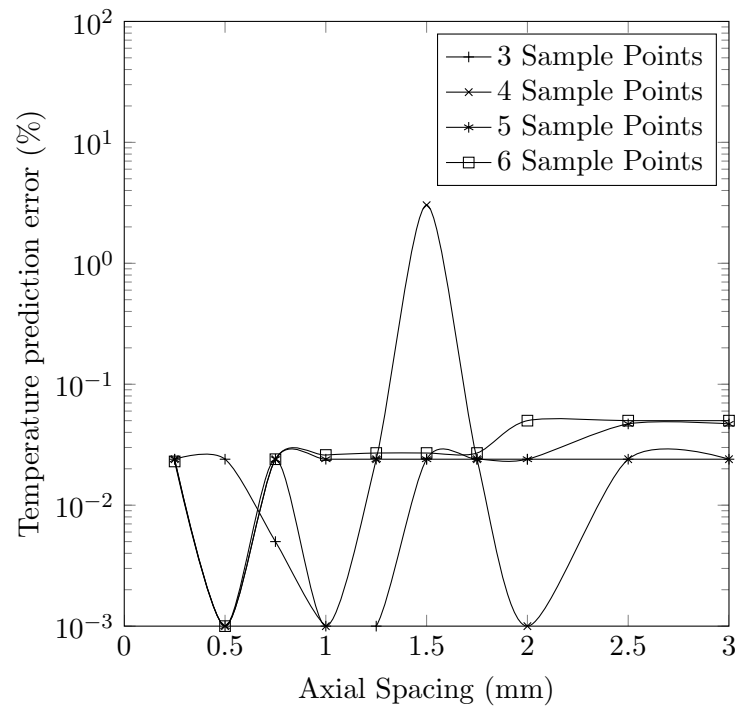


Figure 4.2: Temperature prediction error vs axial spacing between samples
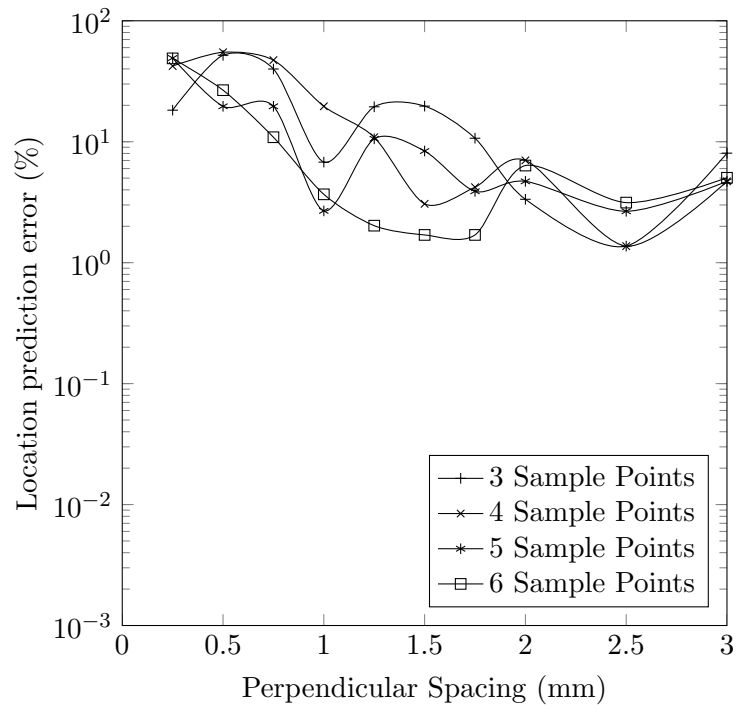
Figure 4.3: Location prediction error vs perpendicular spacing between samples
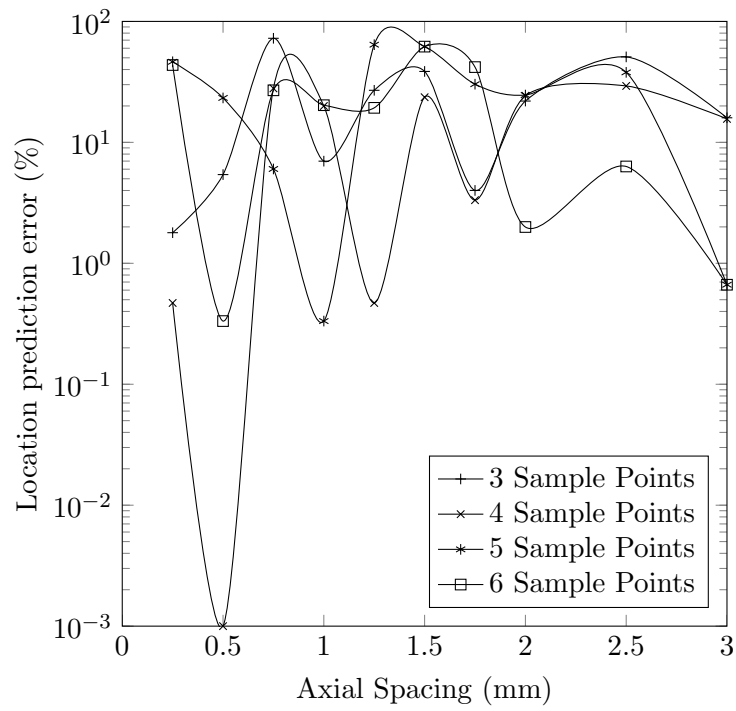


Figure 4.4: Location prediction error vs axial spacing between samples

at $1.5\,mm$ spacing for correcting the location. However, the spacing of $1.5\,mm$ ran into experimental boundary issues (with the plume case chapter 5) and it was decided to use $1\,mm$ spacing instead. Since the datum point calculations are easier if that sample point is reused, the search shape shown in figure 4.5 was settled upon. This is the same result shown earlier. That is to say four horizontal and four vertical, with the intersection sample point being reused, for a total of seven sample points.
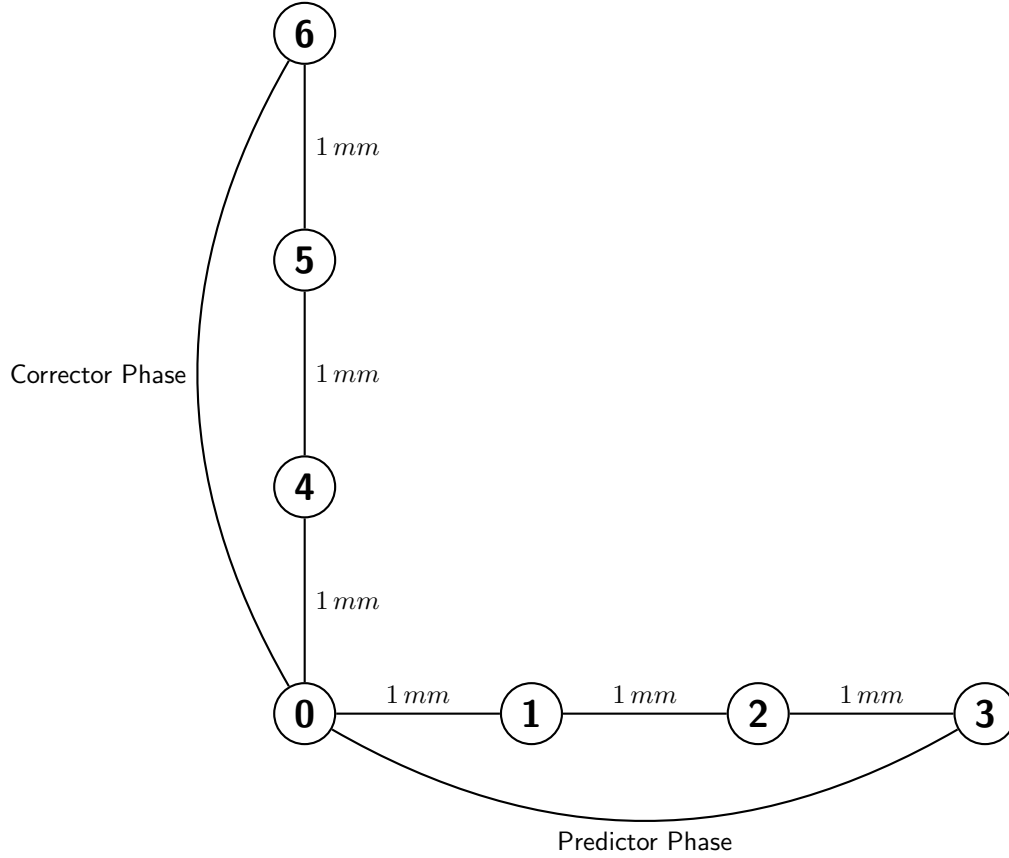


Figure 4.5: Original search shape

The source temperature prediction error was calculated using equation (4.1) and the source location prediction error was calculated using equation (4.2).

$$error_{temp}(\%) = \frac{T_{SP} - T_S}{T_S - T_\infty} \times 100 \qquad (4.1)$$

$$error_{location}(\%) = \frac{\|\boldsymbol{r}_{SP} - \boldsymbol{r}_S\|}{\boldsymbol{r}_S} \qquad (4.2)$$

The range of parameters used to create these sensitivity analysis is shown in table 4.1.

| Parameter | Value |
|---|---|
| axial range $(mm)$ | $0 - 80$ |
| perpendicular range $(mm)$ | $0 - 10$ |
| $T_\infty\,(K)$ | $293$ |
| $P_\infty\,(kPa)$ | $101.32$ |
| $T_{Smin},\,T_{Smax}\,(K)$ | $350,\,450$ |

Table 4.1: Parameters for original sensitivity analysis

It was quickly identified that using the described seven sample points could be reduced to three horizontal and three vertical without significantly increasing the error. Actually, in the case of the perpendicular direction, the error is reduced, which is something that was initially missed. A more robust method for determining the search shape is needed.

## 4.2   Optimization

In an effort to decrease the total number of sample points, decrease the error, and increase the range, a method was developed to determine an optimum search shape[2]. The development of this method starts with identifying the objective function. The predictor step sets the stage for the accuracy of the rest of the algorithm and thus minimizing the error of the predictor step will reduce the overall error. Thus we need to minimize the error associated with equation (3.4), which is rewritten here with some modifications as equation (4.3). Equation (4.3) is used to create error maps.

$$T_{SO} = \frac{1}{n}\{\sum_{i=0}^{n}[m\,(\boldsymbol{r}_0 + \boldsymbol{\Delta}_i + \boldsymbol{\delta})\,T\,(\boldsymbol{r}_0 + \boldsymbol{\Delta}_i) + b\,(\boldsymbol{r}_0 + \boldsymbol{\Delta}_i + \boldsymbol{\delta})]\} \qquad (4.3)$$

The vector $\boldsymbol{r}_{SP}^*$ is changed to $\boldsymbol{r}_0$, indicating that $\boldsymbol{r}_0$ is fixed prior to the optimization. To force the search shape to stay the same during each step of the optimization process, $\boldsymbol{\Delta}$ is included in the local temperature function. The addition of $\boldsymbol{\delta}$ allows the search shape to be used to calculate the error spatially throughout the entire domain.

---

[2]A significant portion of this section was rewritten from [45]

Equation (4.3) does not actually calculate the error that is calculated in equation (4.4), where $\varepsilon$ is the percent error. The effectiveness of a sample point in determining the source temperature is given by the area defined by equation (4.4) at a specified error level. This is due to the desire to reduce the error at the test location, but increase the error everywhere else, increasing the gradient of the convergence.

$$\left| \frac{T_{SO} - T_S}{T_S - T_\infty} \right| \times 100 = \varepsilon \tag{4.4}$$

### 4.2.1 Optimization Methodology

The optimization methodology attempts to minimize the area enclosed by equation (4.4) at a specified error level $\varepsilon$. To perform the optimization, an initial point is selected as $\boldsymbol{r}_0$, which yields the next sample point, $\boldsymbol{r}_1$. This method repeats, yielding the next sample point $\boldsymbol{r}_2$. To increase the accuracy of the inverse methodology, this optimization may be repeated indefinitely, yielding as needed. In the particular case of the plume in a crossflow only three total sampling points were needed to achieve the desired accuracy of 2%, which is better than the accuracy of the experiment. Many iterations were performed, varying $U_\infty$, $T_S$, and $\boldsymbol{r}_0$ to cover the domain. Table 4.2 is a list of the parameters covered, which total to 1050 optimization conditions.

| Parameter | Minimum | Maximum | Increments |
|-----------|---------|---------|------------|
| $U_\infty \ (m/s)$ | 0.0 | 1.0 | 0.2 |
| $T_S \ (K)$ | 350 | 450 | 25 |
| $r_{axial} \ (mm)$ | 0 | 150 | 25 |
| $r_{perp} \ (mm)$ | 0 | 10 | 2.5 |

Table 4.2: Variable domain parameters used for optimization

This optimization process is non-linear with multiple local solutions, therefore a stochastic method is recommended to ensure a global solution. The genetic algorithm from the Mathworks Matlab[32] optimization toolkit was utilized. The Matlab function utilizes standard genetic algorithm methods, such as elitists, crossovers, and mutations. The parameters used are shown in table 4.3. Other parameters were kept at their Matlab

default values. The population size was kept small to reduce computation time. The computation time required approximately 2 weeks running on a twin processor, twelve core computer at 3.2GHz with 32GB of RAM.

| Parameter | Value |
|---|---|
| PopulationSize | 60 |
| Generations | 200 |

Table 4.3: Genetic algorithm parameters

The sample point relative locations from each iteration were averaged in a closest fit averaging method. The datum point is always at the same location, $\mathbf{\Delta}_0 = (0, 0)$. Sample point 1 and sample point 2 relative locations are swapped to maintain a minimum of standard deviation of the relative location average. That is to say, from equation (4.5), if $S_1 > S_2$, then sample point 1 and sample point 2 were swapped.

$$S_1 = \left|\mathbf{\Delta}_1 - \overline{\Delta_1}\right| + \left|\mathbf{\Delta}_2 - \overline{\mathbf{\Delta}_2}\right| \tag{4.5a}$$

$$S_2 = \left|\mathbf{\Delta}_1 - \overline{\Delta_2}\right| + \left|\mathbf{\Delta}_1 - \overline{\mathbf{\Delta}_2}\right| \tag{4.5b}$$

A flow chart of the search shape optimization methodology is shown in figure 4.6.

## 4.2.2 Results and Error Maps

The end result of all of the optimization is to have three points in the odd arrangement listed in table 4.4 and displayed graphically in figure 4.7.

| Sample Point | $\mathbf{\Delta}\,(mm)$ |
|---|---|
| 0 | (0.0, 0.0) |
| 1 | (1.7, 3.5) |
| 2 | (2.8, 0.6) |

Table 4.4: Search shape results of averaging over the domain

The error maps for the optimized search shape show a remarkable improvement over the original search shape. Figure 4.8 is an error map utilizing only one sample
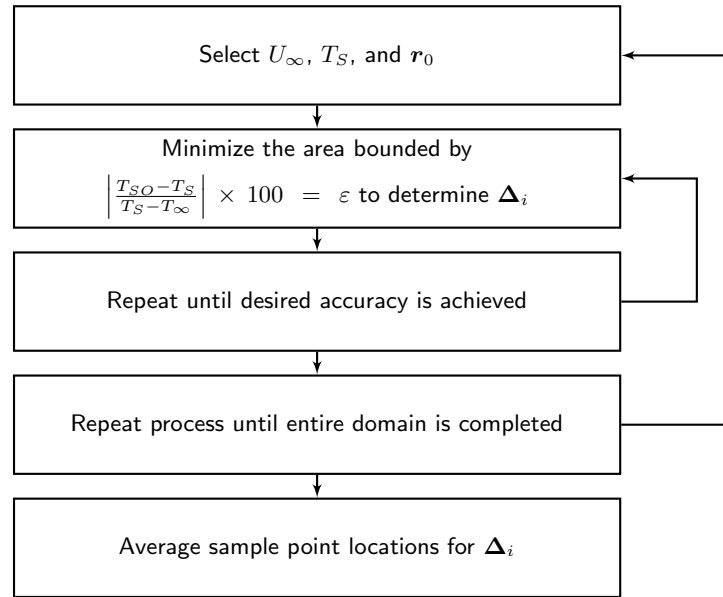
Figure 4.6: Flow chart of the search shape optimization methodology
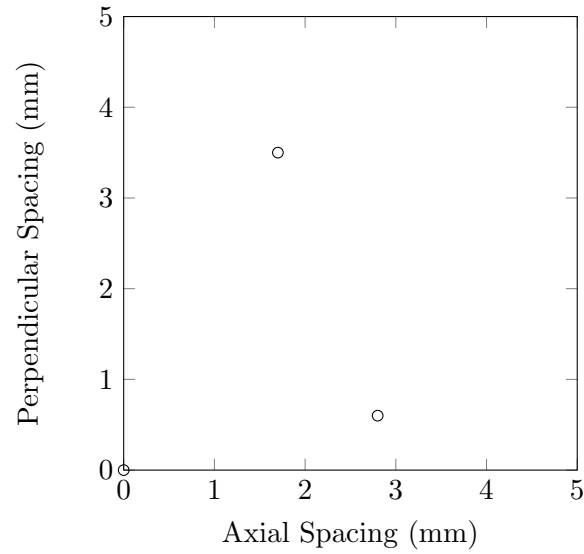


Figure 4.7: Optimized search shape

point, which will be identical to the previous one sample point error map figure 3.5. Figure 4.9 is an error map consisting of two sample points, and figure 4.10 is an error map consisting of three sample points. It should be noted that the three sample point error map is similar in gradient to that of the original search shape at five sample points. One key difference between them would be that the optimized search shape does not have any alternative local minimums, which means the inverse solver does not require the use of a stochastic optimization algorithm.
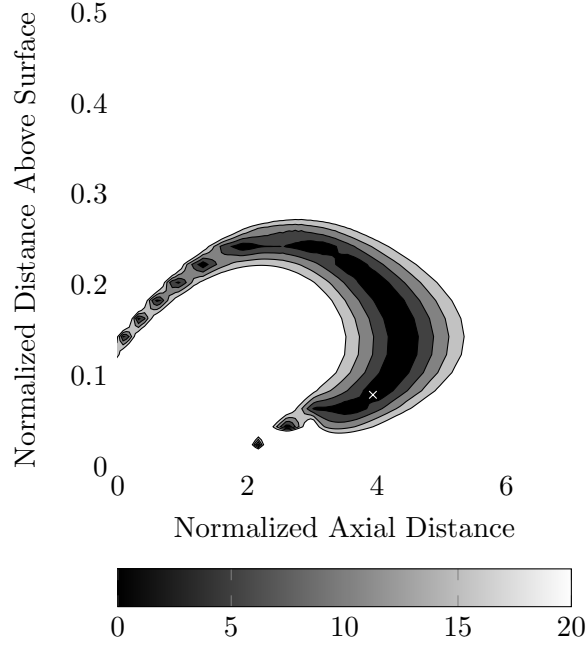


Figure 4.8: Contours of source prediction error, utilizing 1 sample point of information indicated by the 'x'

### 4.2.3  Experimental Concerns

During testing of the optimized search shape, the method functioned as expected. When the sample points exactly correlate to the simulated data then the predictions are accurate. That is to say the methodology can in essence solve three equations for three unknowns ($T_S$, $x_S$, $y_S$). If there is any error present in the sample data, then the problem becomes insurmountable with only three sample points. For this reason more sample points were needed for the experimental data. Nine optimized sample points
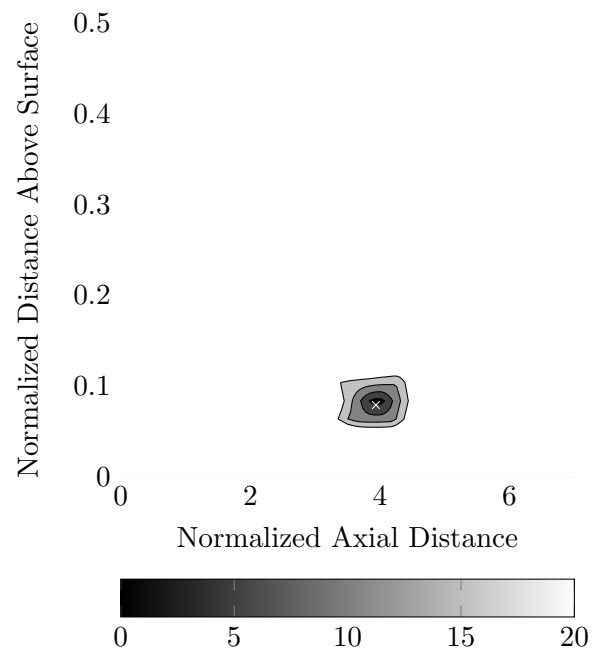
Figure 4.9: Contours of source prediction error, utilizing 2 sample points from the optimized search shape
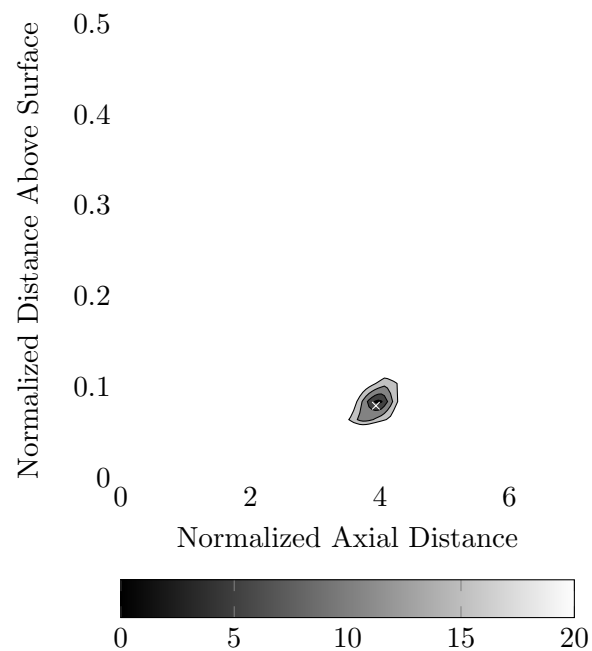


Figure 4.10: Contours of source prediction error, utilizing 3 sample points from the optimized search shape

were determined and are listed in table 4.5. The experimental results did not benefit from using all nine sample points and is discussed further in chapter 5.

| Sample Point | $\Delta\,(mm)$ |
|:---:|:---:|
| 0 | (0.0, 0.0) |
| 1 | (1.7, 3.5) |
| 2 | (2.8, 0.6) |
| 3 | (0.5, 1.1) |
| 4 | (2.1, 1.0) |
| 5 | (2.3, 2.0) |
| 6 | (1.2, 0.8) |
| 7 | (3.1, 0.7) |
| 8 | (0.8, 2.1) |

Table 4.5: Search shape results of averaging over the domain with increasing the sample size to 9

# Chapter 5

# Example Problem: Plume in a Crossflow

## 5.1   Introduction

A plume in a crossflow is as exactly as it sounds; a thermal plume (constant temperature or constant heat flux) rises from a surface and a free stream flow, perpendicular to the plume bends, the plume in the direction of the free stream. The plume in a crossflow of interest has relatively strong crossflow velocity compared to the plume velocity $(U_{plume}/U_infty)$, therefore the plume tends to form a boundary layer close to the surface[1].

Several engineering problems may be interpreted, at least simplistically, as a plume in a crossflow. Some such applications are: environmental flows[7, 33], fires in urban environments[19], fires in tunnels[6] and thermal management systems[39]. The goal of this particular inverse problem is to solve for the location and the strength of the source using only a small set of sample points down stream.

### 5.1.1   Physics of the Forward Problem

The possible flow regimes are governed via several non-dimensional numbers. A list of the important non-dimensional parameters is shown in table 5.1. A thorough explanation of the flow parameters is in appendix A.1. From this we can determine that the flow is usually in the transitional turbulent regime. The flows are too slow to fall into the compressible regime. Lastly, viscous effects must be modeled to allow turbulence to develop, propagate, and dissipate.

---

[1]A significant portion of this chapter was rewritten from [44]

| Non-Dimensional Parameter | Symbol | Range | Flow Regime |
|---|---|---|---|
| Grashoff no. | $Gr$ | $\approx 10^5 - 10^6$ | ratio of buoyancy to viscous forces |
| Rayleigh no. | $Ra$ | $\approx 10^7$ | plume stability |
| Reynolds no. | $Re$ | $\approx 10^3 - 3 \times 10^3$ | ratio of inertial to viscous forces |
| Richardson no. | $Ri$ | $\approx 0.1 - 4$ | ratio of buoyancy to inertial forces |

Table 5.1: Non-dimensional parameters for plume in a crossflow
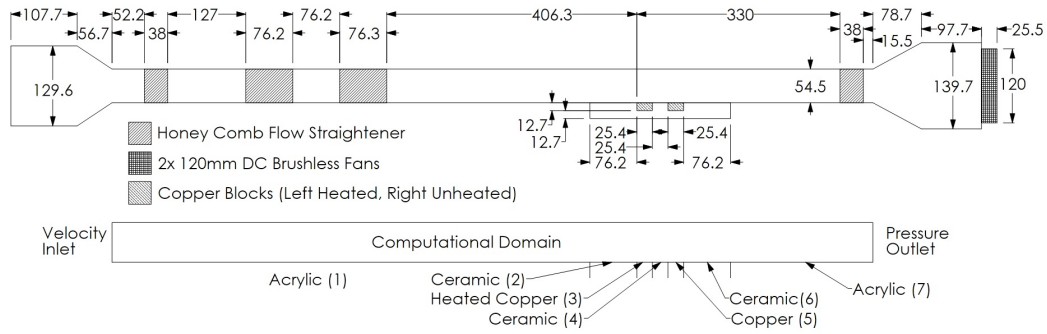


Figure 5.1: Schematics of the wind tunnel and the computational domain [43]

## 5.2 Experimental Apparatus

The primary experimental apparatus is the wind tunnel with test section dimensions of $54.5 \times 305 \times 254\,mm$ ($H \times D \times L$). Due to the large aspect ratio of the wind tunnel ($\approx 5 : 1$), a two dimensional flow may be assumed. A diagram of the apparatus and the simulated domain is shown in figure 5.1. All dimensions are in millimeters and the depth into the page is $305\,mm$. The flow is from left to right in the diagram and is generated by a pair of 12 Volt DC brushless fans. The fans are located at the anterior of the tunnel to reduce the turbulence induced by the spinning blades. In an attempt to generate uniform flow, four flow straighteners are used. Three straighteners are upstream and one downstream. The velocity range is $0 - 5.0\,m/s$.

The heated section is a copper block heated with a resistance type electric heater. The high thermal conductivity of the copper block encourages a uniform heated surface

$25.4\,mm$ wide. Material properties limit the temperature of the copper block to $T_S \leq 450\,K$. This limitation creates a new limitation on the maximum velocity of the wind tunnel. Above $1.0\,m/s$, the plume gets overwhelmed by the free stream. That is to say the thermal plume blends into the flow boundary layer and is difficult to detect using the thermocouple probe describe here.

The free stream velocity is measured via a Pitot-static tube and a differential pressure sensor. The pressure sensor is the NIST traceable sensor from Omega (PX655-0.1DI), which has full scale reading of 0.1 inches of water. The pressure sensor has an error of 0.05% of full scale reading, which results in a maximum of 3% error with at most $0.018\,m/s$ error across the range of applicable velocities.

The local temperatures are measured using a K-type thermocouple probe of 40 gauge wire mounted on a two-dimensional stage for motion within the plane of the diagram. Sampling over several days indicate a maximum error of 7% outside the plume and 2% error within the plume. The origin of the domain is located at the upstream edge of the heat source on the surface. Ambient temperature was measured using both a K-type thermocouple with error of approximately $\pm 2.0\,K$ and a calibrated mercury glass bulb thermometer with an error of $\pm 0.5\,K$.

The calibration of the thermocouples, two dimensional translation stages, and the hot-wire anemometer are described in appendix B. The data acquisition hardware and software is described in appendix C.

## 5.3   Methodology

The methodology described in chapter 3 is applied here in incremental steps. The steps start with the simplest case of known location and end with source location and source strength unknown. In an effort to determine the error of the algorithm, the data sets are simulation based only. Each step was repeated with the optimized search shape to show the effect that the optimized search shape has on the prediction error. The results of this incremental stepping is shown at the end of this chapter in section 5.6.

## 5.4    Simulation

The simulations were performed using the software package Ansys Fluent version 13 [2]. The Navier-Stokes equations were solved using a three-dimensional, steady-state, realizable $k - \epsilon$ model with enhanced wall effects. The exact governing equations solved is documented in appendix A.8.3. The three-dimensional model is employed due to a limitation of Fluent, which is solid-solid conduction is not modeled in two-dimensional conjugate heat transfer problems.

The origin is located at the upstream edge of the heated surface. The axial downstream direction is $+x$. Normal to the heated surface is $+y$. Gravity acts in the $-y$ direction.

The working fluid is air and is modeled as an ideal gas at atmospheric pressure. Fluid properties such as viscosity were calculated according to the model described in appendix A.5.

The boundary conditions at the free stream inlet are described as:

$$u = U_\infty, v = 0, T = T_\infty, P = P_\infty, l = 4mm, I = 5\% \tag{5.1a}$$

$$k = \frac{3}{2} \left( U_\infty I \right)^2 \tag{5.1b}$$

$$\epsilon = C_\mu^{3/4} \frac{k^{3/2}}{l} \tag{5.1c}$$

The upper boundary was chosen to be symmetric to reduce the possibility of errors introduced by the experimentally accurate no-slip condition. This is acceptable since the upper boundary is very far from the plume and thus should have negligible effect on the numerical result. The exit boundary is a simple pressure outflow set to $P_\infty$.

The bottom boundary consists of seven zones. The geometric boundaries of the zones are shown in figure 5.1, from left to right: acrylic, ceramic, heated copper, ceramic, unheated copper, ceramic, and acrylic. All solid material properties are set as constant. The ceramic is in actuality a composite material made from an aerogel and ceramic. It has an effective density of $2330\, kg/m^3$. The composite has a specific heat of $1138\, J/(kg - K)$. It also has a thermal conductivity of $0.1\, W/(m - K)$. The density was determined by weighing the mould before and after the composite was added, and

knowing the mould volume. The specific heat is that of the ceramic obtained by the manufacturer(Coitronics), as it makes up most of the mass and volume. Lastly, the thermal conductivity was determined via an approximation between the ceramic and the aero-gel.

All solid boundaries are simulated with conjugate heat transfer with an effective layer width of $25.4\,mm$, except of the acrylic walls which has a width of $12\,mm$. All external solid boundary conditions are iso-thermal with a temperature of $T_\infty$. Similarly, the external solid-boundary of the heated copper region is $T_S$.

## 5.5    Simulation Validation

As with all simulations, they mean nothing unless you can verify they accurately model the experiment. There are several ways to accomplish the verification, each having varying degrees of validness. Various flow models can give significantly different results, a consensus may be used to validate the simulation. Grid independence is an absolute must, as the solution can not ever be a function of the discretization of the simulation. A comparison against a benchmark solution may be used. A comparison against experimental results may also be used. If possible it is best to perform all of the above, to ensure the best validation. The conditions in the following validation tests are shown in table 5.2.

| Parameter | Value |
|---|---|
| $U_\infty\,(m/s)$ | 0.6 |
| $T_\infty\,(K)$ | 294.5 |
| $P_\infty\,(kPa)$ | 101.6 |
| $T_S\,(K)$ | 433 |

Table 5.2: Validation test conditions [43]

### 5.5.1 Flow Model

Three flow models have been used to help validate the simulation. The three are Spalart-Allmaras, $k - \epsilon$, and $k - \omega$. The methods and solved equations are described in appendix A.8. Two figures are used to demonstrate the flow models response. The data contained therein is normalized using equation (5.2). The two slices of the temperature domain are at $X = 1.6$ and $X = 2.25$ and shown in figure 5.4 and figure 5.5 respectively.

$$\phi = \frac{T - T_\infty}{T_S - T_\infty} \tag{5.2a}$$

$$X = \frac{x}{L} \tag{5.2b}$$

$$Y = \frac{y}{L} \tag{5.2c}$$

$$V = \frac{U}{U_\infty} \tag{5.2d}$$

Both of the figures show good agreement between $k - \epsilon$ and $k - \omega$, with Spalart-Allmaras varying slightly. The Spalart-Allmaras model has difficulties solving this type of problem and is expected to deviate from the other models. The relatively close agreement of all three models gives credence to the simulations.

### 5.5.2 Grid Independence

The simplest way to demonstrate grid independence is to show that the solution does not vary with cell count[47]. This is exactly what is shown in table 5.3. Cell count and location is varied with the results of the temperature tabulated. With the temperature varying only a fraction of a percent over the range of cell counts, it is inferred that the solution is independent of the grid. The grid here is an unstructured, hexagonal mesh with an emphasis near the plume source and down stream of the plume.

### 5.5.3 Iterative Convergence

Iterative convergence is achieved through increasing the residual requirements to typically absurd values and comparing. In this case absurd is $10^{-7}$ for all parameters. In reality, only the continuity residual is needed to be modified, as this always sets the
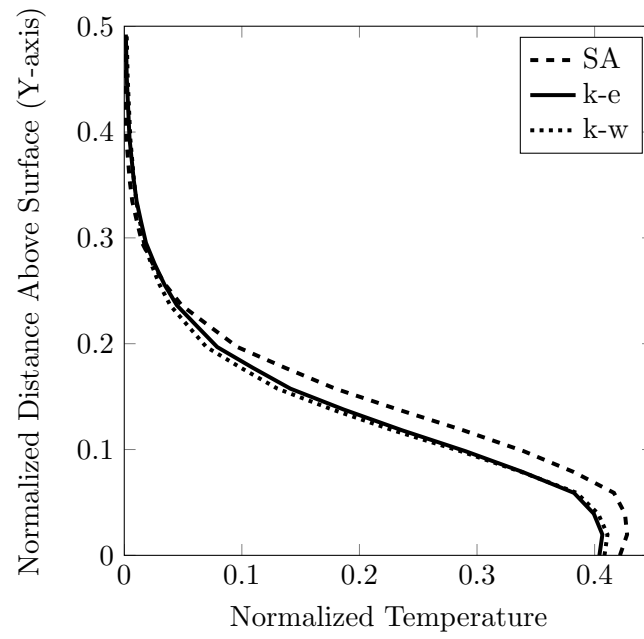
Figure 5.2: Validation of the simulation: local temperature using three flow models at $X = 1.6$
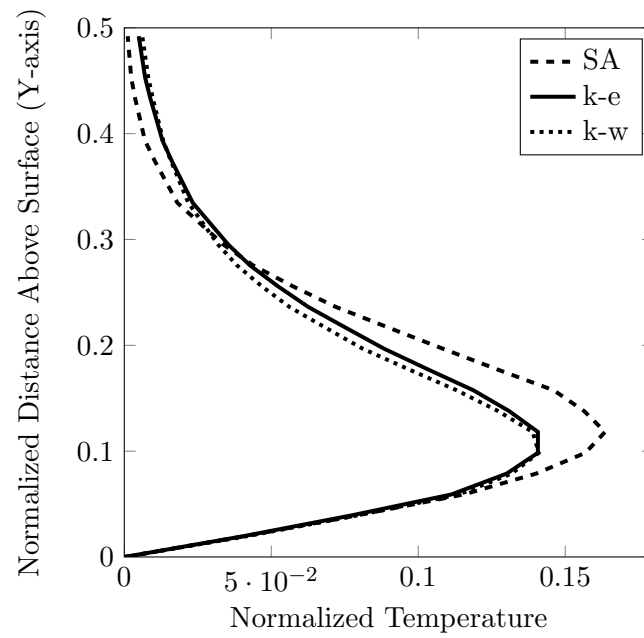


Figure 5.3: Validation of the simulation: local temperature using three flow models at $X = 2.25$

| Location (x,y) (mm) | 30,2 | 35,3 | 40,1 | 50,10 |
|---|---|---|---|---|
| Cell Count | | | | |
| 67399 | 360.3 | 338.5 | 352.9 | 295.6 |
| 94378 | 360.2 | 338.6 | 352.7 | 295.6 |
| 130292 | 360.2 | 338.5 | 352.7 | 295.6 |
| 153290 | 360.1 | 338.8 | 352.6 | 295.8 |

Table 5.3: Grid Independence Study [43], local static temperature (K)

convergence requirement. Similarly to the flow models comparison, two slices of the domain are used. In this case, the absurd case is subtracted from the other residual cases so that the small differences are more discernible. Again, the location of the slices are normalized using equation (5.2) and are at $X = 1.6$ and $X = 2.25$ in figure 5.4 and figure 5.5. Both figures show small differences between the residual cases. Even at the normal $10^{-3}$, case the error compared to a residual of $10^{-7}$ is only $0.005\,K$. The plots do not cover the entire domain because the values identically correlate with the $10^{-7}$ case, and therefore the result is 0 and cannot be plotted on a logarithmic plot. Barring further evidence, it is safe to assume iterative convergence has been achieved.

### 5.5.4 Comparison to Experiment

The last test of the simulation is comparison against experimental results. Two slices of the comparison of local temperatures are shown in figures 5.6 and 5.7. The figures are normalized using equation (5.2). The simulation tends to overshoot the experimental results by a small margin 2%, but typically less. The conditions of the comparisons are listed in table 5.4.

Another comparison against the experiment may be done. Hot-wire anemometer data may be compared against the simulation with no thermal plume. This comparison is made in figure 5.8, with the only significant error at $1\,mm$ above the plate of 36% error. This near wall error is expected, because near wall conditions are difficult to simulate and difficult to model perfectly.
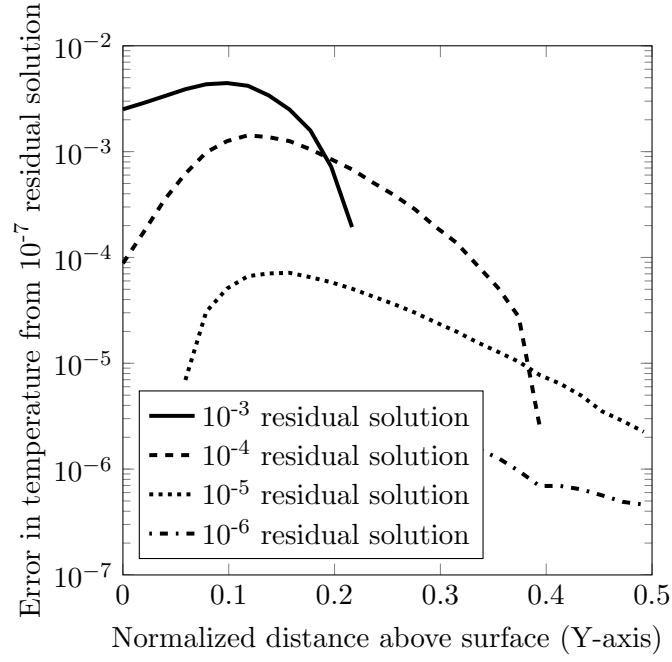
Figure 5.4: Validation of the simulation: local temperature error vs residuals set to $10^{-7}$ at $X = 1.6$
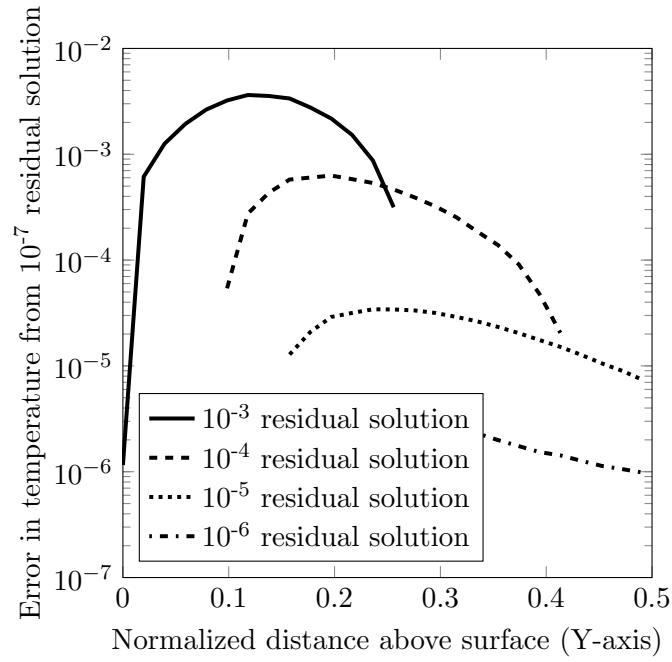


Figure 5.5: Validation of the simulation: local temperature error vs residuals set to $10^{-7}$ at $X = 2.25$
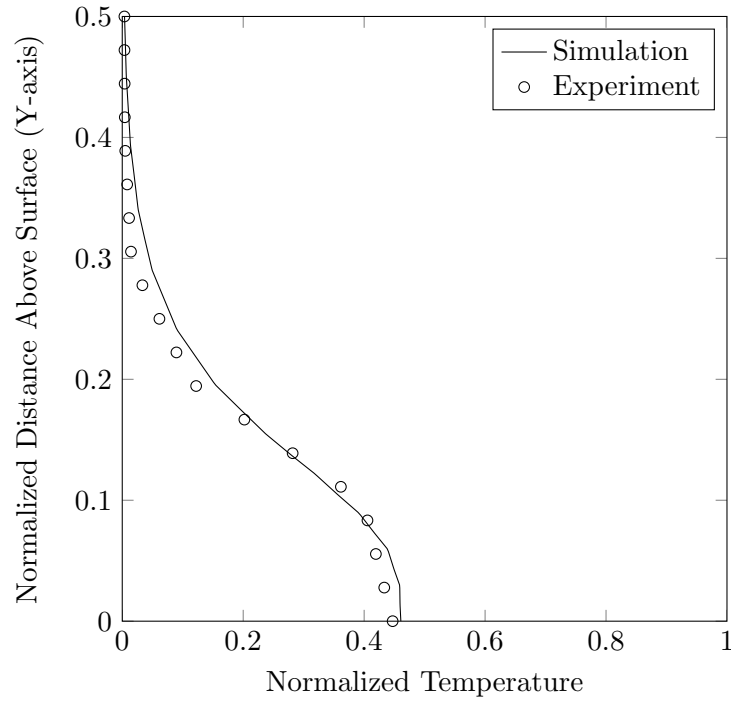
Figure 5.6: Validation of the simulation: local temperature - experiment versus simulation at $X = 1.6$ [44]
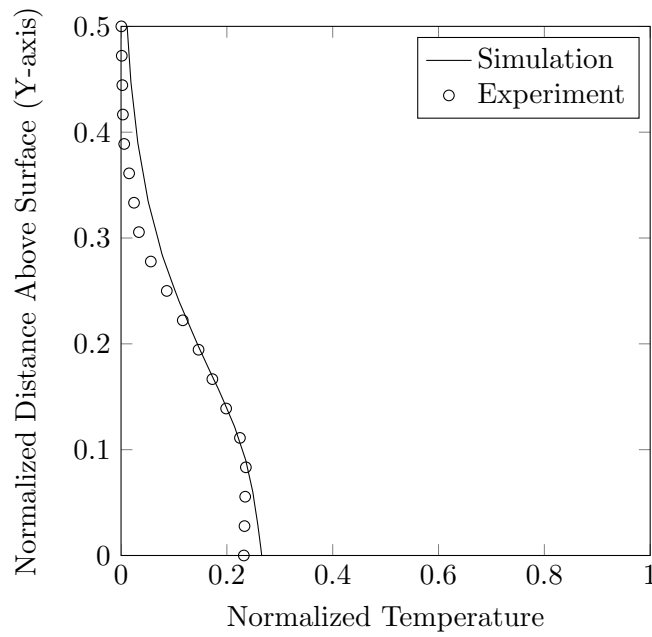


Figure 5.7: Validation of the simulation: local temperature - experiment versus simulation at $X = 2.25$ [44]
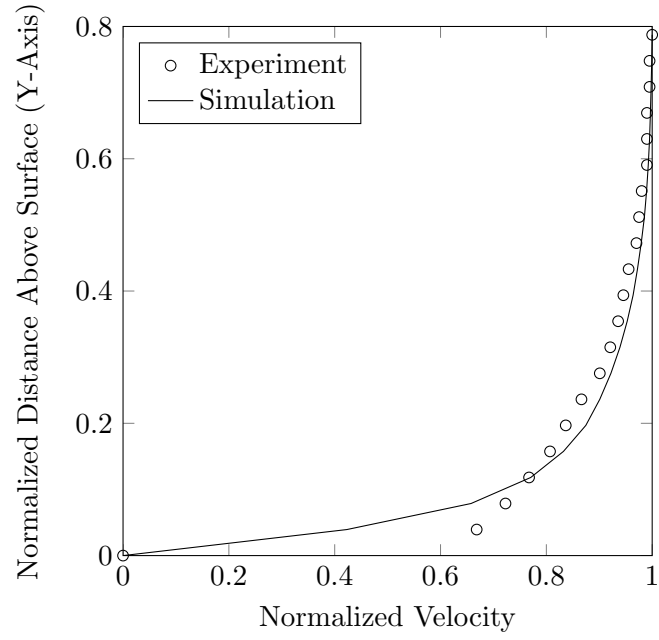
Figure 5.8: Validation of the simulation: velocity - experiment versus simulation, no thermal plume

| Parameter | Value |
| --- | --- |
| $U_\infty \, (m/s)$ | $0.6 \pm 0.15$ |
| $T_\infty \, (K)$ | $294.5 \pm 0.5$ |
| $P_\infty \, (kPa)$ | $101.6 \pm 0.2$ |
| $T_S \, (K)$ | $433 \pm 2.0$ |

Table 5.4: Validation Test [43]

## 5.6  Results

The previously described methodology is applied in a step-by-step fashion. The error associated with each step is calculated using equation (5.3). The location vector is decomposed into $X$ and $Y$ to make it easier to demonstrate.

$$error_{temp}(\%) = \frac{|T_{SP} - T_S|}{T_S - T_\infty} \times 100 \tag{5.3a}$$

$$error_{x-location}(\%) = \frac{|x_{SP} - x_S|}{x_S} \times 100 \tag{5.3b}$$

$$error_{y-location}(\%) = \frac{|y_{SP} - y_S|}{y_S} \times 100 \tag{5.3c}$$

### 5.6.1  Source Location Known

This step is the "source location is known" step and only the source strength is unknown. That is to say $\boldsymbol{r}_S$ is known while $T_S$ is not known. Examining equation (3.1), substituting in a constant $\boldsymbol{r}$ results in a dramatic simplification of the equation. If the temperature at one location is known, equation (3.1) can be used to directly calculate the source strength.

There are twenty-four selected cases labeled A-X. The conditions are shown in table 5.5. Case J for example, has a free stream velocity of $U_\infty = 0.6\,m/s$, source temperature of $T_S = 425\,K$, and a datum location of $\boldsymbol{r}_0 = (60\,mm,\,1\,mm)$. The non-varying simulation conditions are listed in table 5.6.

The results presented here in figure 5.9 requires only one sample point, which is listed. The prediction error of the source temperature is negligible for all cases within the plume. The small error most likely consists of machine error and neglecting variations in density and buoyancy, although this was not verified. Since this table was generated using only simulated data, other error such as radiation was not considered.

### 5.6.2  Source Elevation and Strength Known

This incremental step is both a step forward and backwards to achieving the goal of location and strength unknown. Axial location is unknown, but the source strength is

| $U_\infty$ $(m/s)$ | 0.6 | 0.6 | 1.0 | 1.0 |
|---|---|---|---|---|
| $T_S$ $(K)$ | 375 | 425 | 375 | 425 |
| Location (x,y) | | | | |
| 40 mm, 1 mm | A | B | C | D |
| 40 mm, 2 mm | E | F | G | H |
| 60 mm, 1 mm | I | J | K | L |
| 60 mm, 2 mm | M | N | O | P |
| 80 mm, 1 mm | Q | R | S | T |
| 80 mm, 2 mm | U | V | W | X |

Table 5.5: Several sampled case parameters

| Parameter | Value |
|---|---|
| $T_\infty$ $(K)$ | 293 |
| $P_\infty$ $(kPa)$ | 101.3 |

Table 5.6: Simulation test conditions
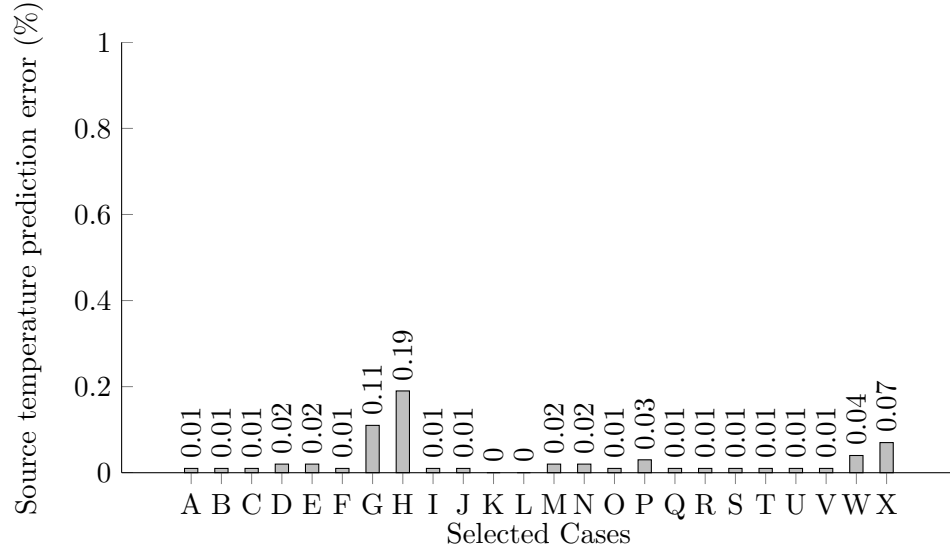


Figure 5.9: Error in the prediction of $T_S$ from several sampled cases within the plume with $\boldsymbol{r}_S$ known

known. If the source strength is known a priori, then the methodology breaks down to only the corrector half. Figure 5.10 is a similar plot to the previous, and follows the same cases shown in table 5.5. The plot is of the percent error in predicting the axial location of the source, utilizing a pre-optimized search shape of 5 sample points. Even with the pre-optimized search shape, the error is less than 1.0% for all cases. Figure 5.11 is the exact same plot utilizing the optimized search shape. The optimized search shape reduces the error to 0.1% or less in all test cases.
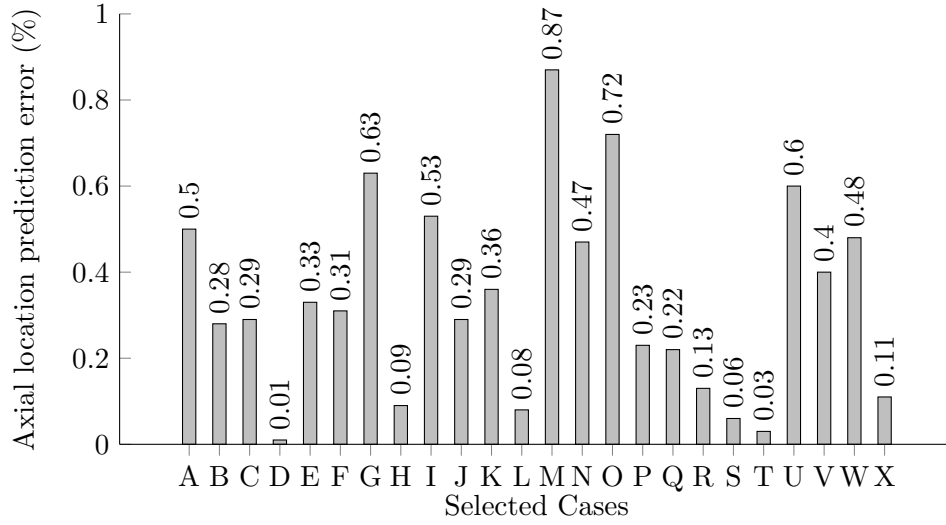


Figure 5.10: Error in the prediction of axial location from several sampled cases within the plume with $T_S$ and elevation known, pre-optimized search shape

### 5.6.3 Source Strength Known

This step is conceptually no different than the previous one. The methodology is reduced to the corrector half only. As might be expected, the error shown in figure 5.12 is similar to that shown in the previous step, figure 5.10. The elevation prediction error shown in figure 5.13 is larger, as might be anticipated because it is more sensitive than the axial direction and the values are numerically smaller. Both of these figures show the error using the pre-optimization search shape.
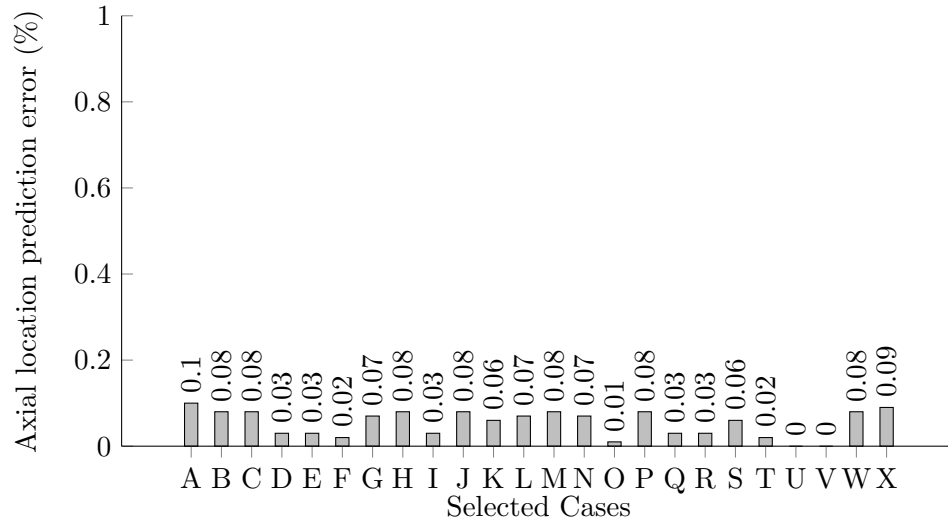
Figure 5.11: Error in the prediction of axial location from several sampled cases within the plume with $T_S$ and elevation known, optimized search shape
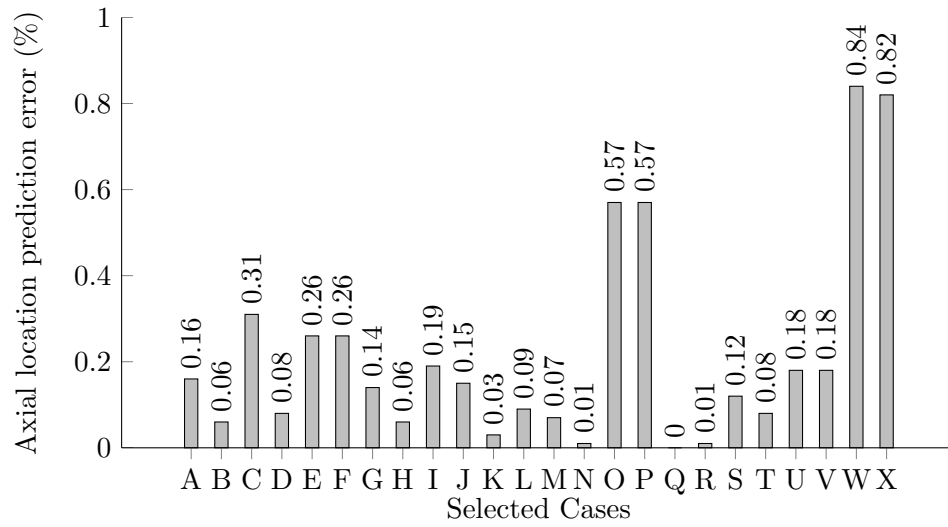


Figure 5.12: Error in the prediction of axial location from several sampled cases within the plume with $T_S$ known, pre-optimized search shape
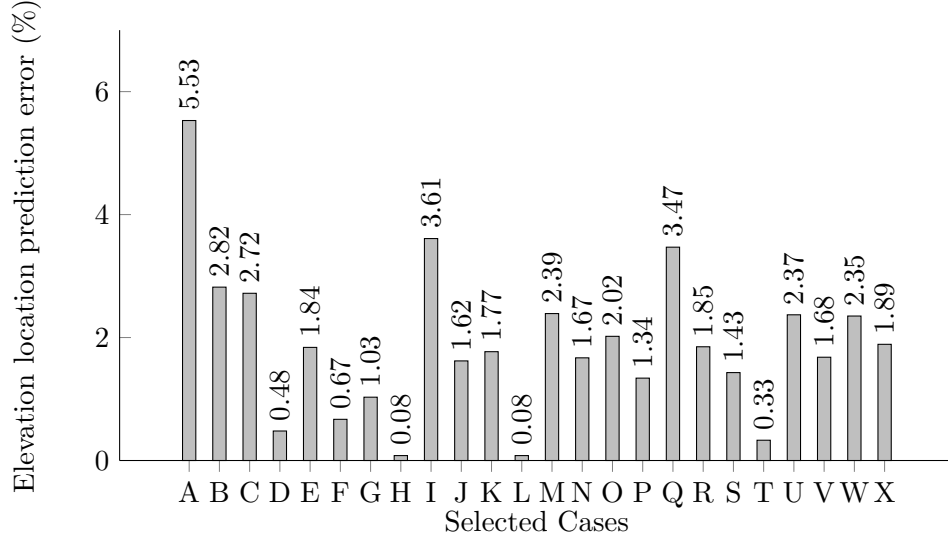
Figure 5.13: Error in the prediction of elevation location from several sampled cases within the plume with $T_S$ known, pre-optimized search shape

### 5.6.4 Source Strength and Source Location Unknown

This step assumes no a priori knowledge. The first set of figures(figures 5.14 to 5.16) are the errors associated with the prediction of the source location and strength utilizing the pre-optimized search shape. While the second set of figures(figures 5.17 to 5.19) utilized the optimized search shape. All of the figures utilize the same configuration shown in table 5.5.

The errors between the pre-optimized and optimized search shape are of similar order, but usually favors the optimized case. Just to re-iterate, the major benefit of the optimized search shape was to reduce the number of sample points required, while reducing the number of local minimums existing in the search space. The optimized search shape does generally improve accuracy, but it was not the goal of the optimization.

A plot of actual source temperature and predicted source temperature is shown in figure 5.20. The line of zero error is plotted for reference. The data in figure 5.20 consists of more sets than shown in the previous plots, and is demonstrative of the capabilities of the methodology.
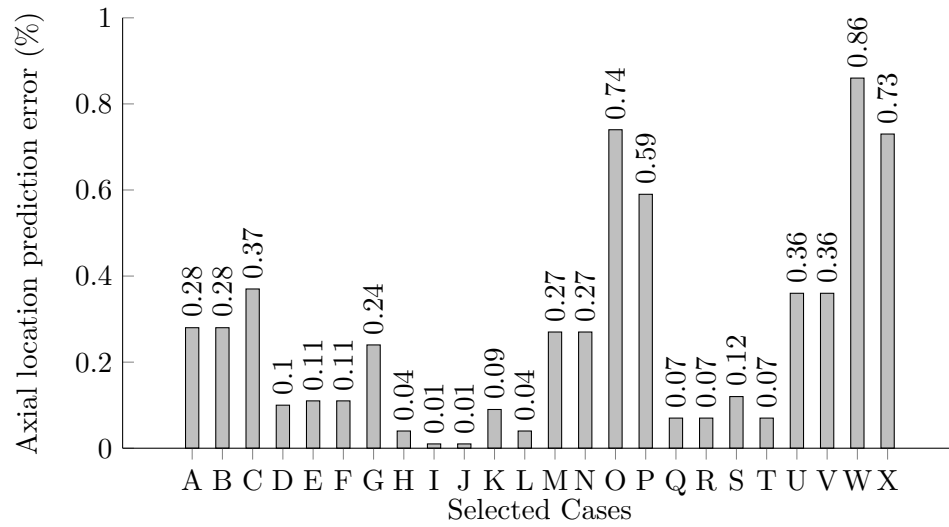
Figure 5.14: Error in the prediction of axial location from several sampled cases within the plume, pre-optimized search shape
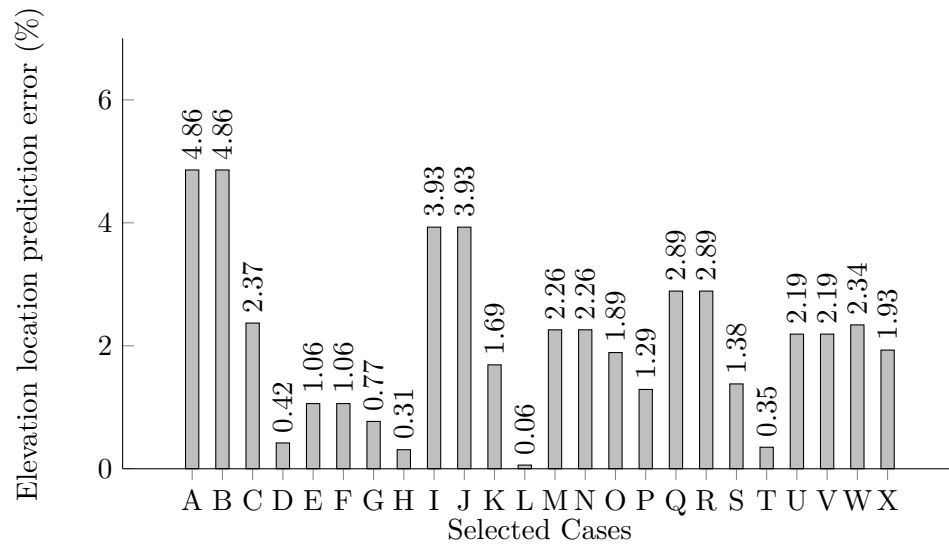


Figure 5.15: Error in the prediction of elevation location from several sampled cases within the plume, pre-optimized search shape
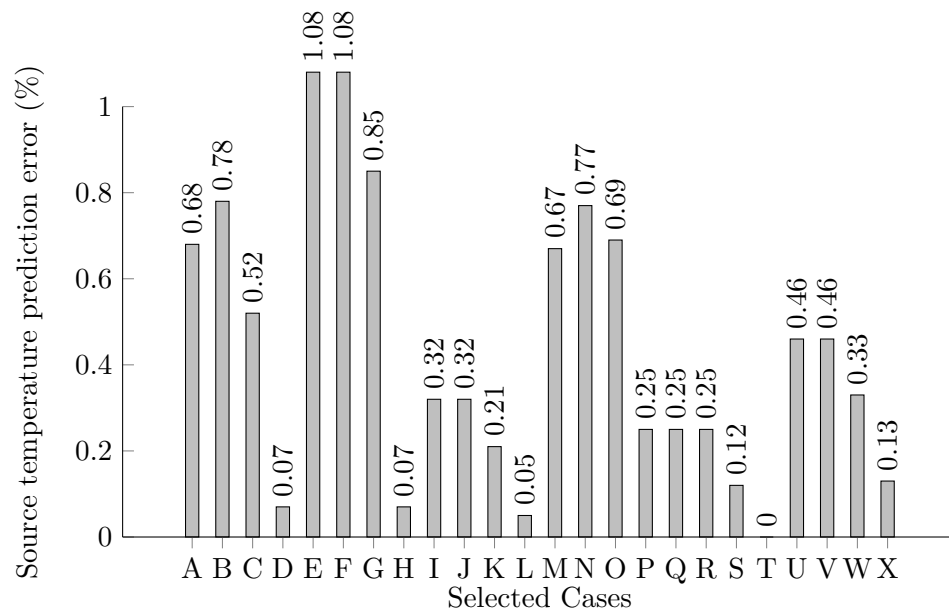
Figure 5.16: Error in the prediction of source strength from several sampled cases within the plume, pre-optimized search shape
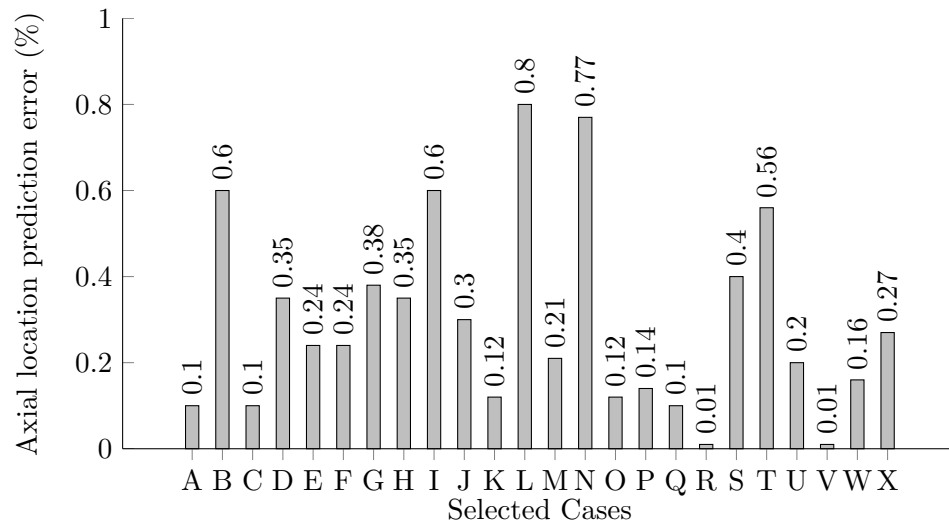


Figure 5.17: Error in the prediction of axial location from several sampled cases within the plume, optimized search shape

52
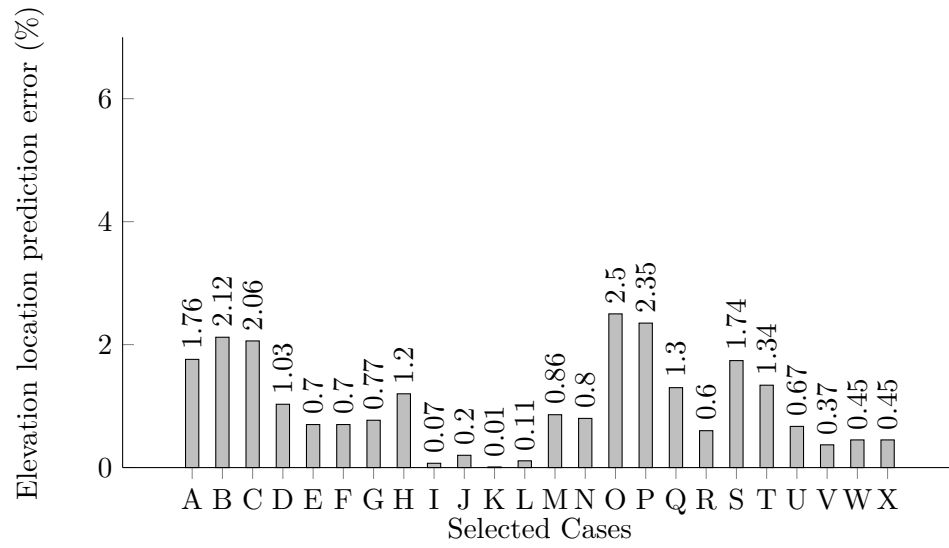


Figure 5.18: Error in the prediction of elevation location from several sampled cases within the plume, optimized search shape
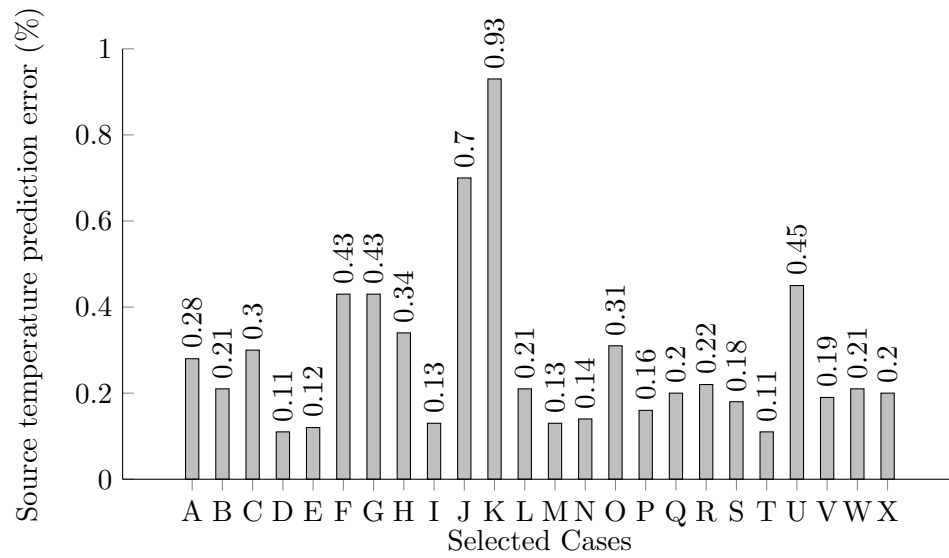


Figure 5.19: Error in the prediction of source strength from several sampled cases within the plume, optimized search shape
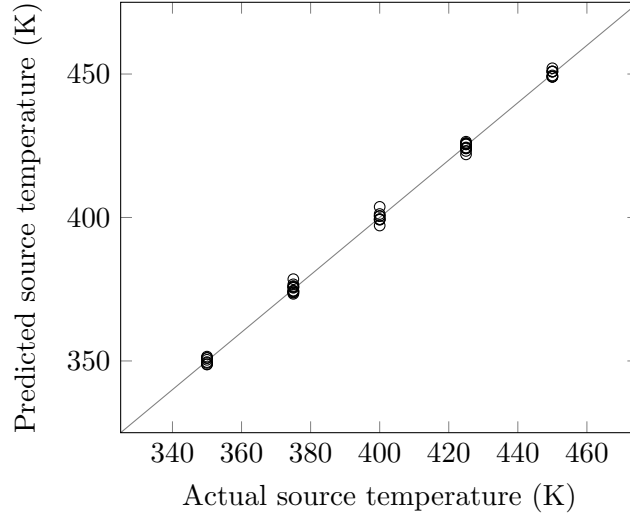
Figure 5.20: Actual vs predicted source temperature for several cases within the plume, optimized search shape

### 5.6.5 Experimental Results

The very last step on this step-by-step approach is solving the problem with experimental results. As in the previous situation, no previous knowledge is known and the cases follow those of table 5.5. Due to the severely increased error, the previously used bar plot was dispensed with, and a table of the information is used. Non-varying experimental parameters are listed in table 5.7. The larger error bounds are due to experimental sampling occurring over the course of two days. Table 5.8 consists of the error associated with the source location and source strength using experimental data and the pre-optimized search shape. The significant increase in error is explained by experimental error, and simulations not accurately portraying the experiment.

| Parameter | Value |
| --- | --- |
| $T_\infty\,(K)$ | $294.5 \pm 4.0$ |
| $P_\infty\,(kPa)$ | $101.6 \pm 0.8$ |

Table 5.7: Experimental test conditions

Table 5.9 is nearly identical to the previous table, except it was generated using

the experimental optimized search shape with five sample points(table 4.5). The errors are generally reduced, however, utilizing the optimized search shape did not adequately resolve the cases which previously had large errors.

Table 5.10 increases the sample point count to nine, utilizing all of the sample points determined in the optimization. Overall the error was decreased, except for a select few minor increases. The difficult to resolve cases were significantly improved, and again, not adequately. This leads credence to the possibility of experimental error in these cases.

Lastly, a plot of actual versus predicted source temperature is shown in figure 5.21. A line of zero error is shown for convenience. This plot contains more sets of data than shown in the previous plots.
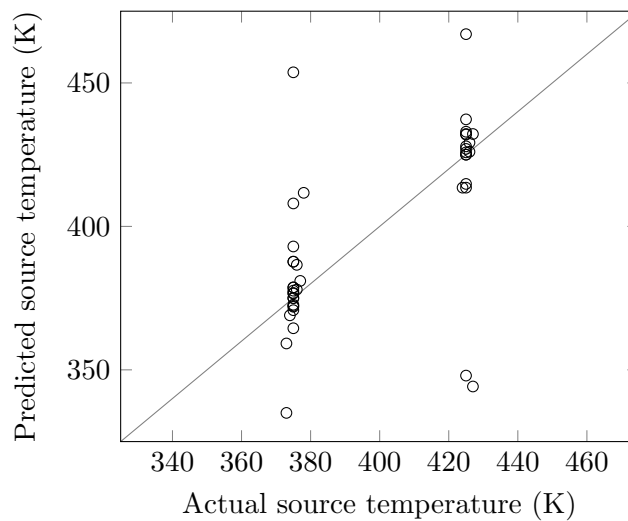


Figure 5.21: Actual vs predicted source temperature for several cases within the plume, optimized search shape, utilizing experimental data

### 5.6.6 Error Analysis

To perform the error analysis of the methodology, an artificial error was added to the sample points. This artificial error ranged from 0.1% to 10%. Figures 5.22 to 5.24 plot this error analysis for the axial location, elevation location, and source strength, respectively. These figures show the median error of the 24 cases used previously from

| $U_\infty$ (m/s) | | 0.6 | 0.6 | 1.0 | 1.0 |
|---|---|---|---|---|---|
| $T_S$ (K) | | 375 | 425 | 375 | 425 |
| Location (x,y) | | | | | |
| 40 mm, 1 mm | X | 0.0% | 2.5% | 5.0% | 0.0% |
| | Y | 0.0% | 10.% | 2.0% | 10.% |
| | T | 1.2% | 1.8% | 0.0% | 1.1% |
| 40 mm, 2 mm | X | 2.5% | 2.5% | 2.5% | 2.5% |
| | Y | 10.% | 10.% | 10.% | 5.0% |
| | T | 1.7% | 2.0% | 0.7% | 1.9% |
| 60 mm, 1 mm | X | 0.0% | 3.3% | 6.7% | 0.0% |
| | Y | 0.0% | 8.0% | 5.0% | 2.0% |
| | T | 1.1% | 4.2% | 3.3% | 4.9% |
| 60 mm, 2 mm | X | 6.7% | 6.7% | 3.7% | 3.3% |
| | Y | 10.% | 10.% | 10.% | 10.% |
| | T | 1.5% | 4.9% | 3.2% | 3.2% |
| 80 mm, 1 mm | X | 0.0% | 7.5% | 3.7% | 0.0% |
| | Y | 1.0% | 40.% | 10.% | 10.% |
| | T | 6.1% | 38.% | 54.% | 32.% |
| 80 mm, 2 mm | X | 5.0% | 12.% | 2.5% | 1.2% |
| | Y | 25.% | 35.% | 10.% | 5.0% |
| | T | 8.8% | 29.% | 41.% | 54.% |

Table 5.8: Error in predicting source location ($x_S$, $y_S$) and source strength($T_S$) from several sample cases within the plume, pre-optimized search shape, utilizing experimental data [44]

| $U_\infty$ $(m/s)$ | | 0.6 | 0.6 | 1.0 | 1.0 |
|---|---|---|---|---|---|
| $T_S$ $(K)$ | | 375 | 425 | 375 | 425 |
| Location (x,y) | | | | | |
| 40 mm, 1 mm | X | 0.0% | 1.2% | 5.0% | 0.8% |
| | Y | 0.0% | 4.2% | 1.2% | 1.3% |
| | T | 0.8% | 0.2% | 0.0% | 0.7% |
| 40 mm, 2 mm | X | 1.5% | 2.5% | 2.5% | 2.4% |
| | Y | 5.0% | 5.0% | 5.0% | 4.8% |
| | T | 1.6% | 0.0% | 0.6% | 1.7% |
| 60 mm, 1 mm | X | 0.1% | 1.0% | 6.3% | 0.0% |
| | Y | 0.3% | 4.0% | 2.0% | 1.0% |
| | T | 1.0% | 1.0% | 3.1% | 2.7% |
| 60 mm, 2 mm | X | 1.4% | 4.7% | 1.1% | 2.8% |
| | Y | 3.1% | 5.0% | 1.1% | 3.3% |
| | T | 1.1% | 2.9% | 0.7% | 2.4% |
| 80 mm, 1 mm | X | 0.0% | 2.5% | 1.8% | 0.2% |
| | Y | 1.1% | 15.% | 5.0% | 5.0% |
| | T | 4.2% | 20.% | 16.% | 19.% |
| 80 mm, 2 mm | X | 3.0% | 6.0% | 2.4% | 0.7% |
| | Y | 8.0% | 18.% | 5.0% | 4.0% |
| | T | 4.8% | 20.% | 21.% | 18.% |

Table 5.9: Error in predicting source location $(x_S, y_S)$ and source strength$(T_S)$ from several sample cases within the plume, optimized search shape with 5pts, utilizing experimental data

| $U_\infty$ $(m/s)$ | | 0.6 | 0.6 | 1.0 | 1.0 |
|---|---|---|---|---|---|
| $T_S$ $(K)$ | | 375 | 425 | 375 | 425 |
| Location (x,y) | | | | | |
| 40 mm, 1 mm | X | 0.0% | 0.8% | 3.0% | 0.7% |
| | Y | 0.0% | 4.1% | 1.1% | 1.2% |
| | T | 0.7% | 0.2% | 0.0% | 0.7% |
| 40 mm, 2 mm | X | 0.8% | 2.4% | 2.0% | 1.9% |
| | Y | 1.2% | 4.2% | 4.1% | 2.4% |
| | T | 1.6% | 0.0% | 0.6% | 1.7% |
| 60 mm, 1 mm | X | 0.1% | 0.9% | 0.7% | 0.2% |
| | Y | 0.3% | 3.1% | 1.1% | 0.8% |
| | T | 1.0% | 0.8% | 0.7% | 1.7% |
| 60 mm, 2 mm | X | 1.2% | 2.7% | 0.6% | 1.9% |
| | Y | 1.9% | 3.8% | 0.9% | 2.7% |
| | T | 0.8% | 1.7% | 0.5% | 2.1% |
| 80 mm, 1 mm | X | 0.2% | 2.4% | 1.6% | 0.7% |
| | Y | 1.0% | 8.8% | 3.7% | 3.0% |
| | T | 3.4% | 12.% | 8.9% | 13.% |
| 80 mm, 2 mm | X | 2.1% | 4.1% | 0.8% | 0.5% |
| | Y | 6.6% | 16.% | 2.2% | 2.3% |
| | T | 2.8% | 18.% | 9.8% | 10.% |

Table 5.10: Error in predicting source location $(x_S, y_S)$ and source strength$(T_S)$ from several sample cases within the plume, optimized search shape with 9pts, utilizing experimental data

table 5.5. The three sample point conditions do not fair particularly well, which is expected as the three sample points offer no error correction capability. That is to say, three sample points solve for three unknown parameters, there is no more information left to correct for errors.

The maximum error obtained for the axial location prediction was less than 0.5% (except for the three sample point condition). Similarly, the maximum error for elevation was less than 1.0%. The source strength prediction error seems to be of the same order as the artificial error. This is to be expected, as the source strength is linearly related to the temperature at a given location, as described previously in chapter 3.
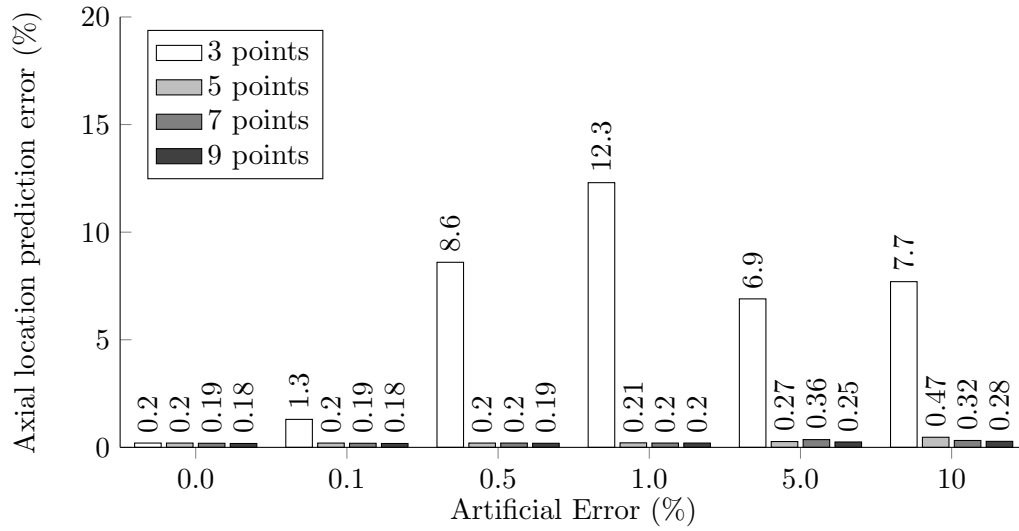


Figure 5.22: Axial location prediction error(%) produced from artificially adding error to sample points
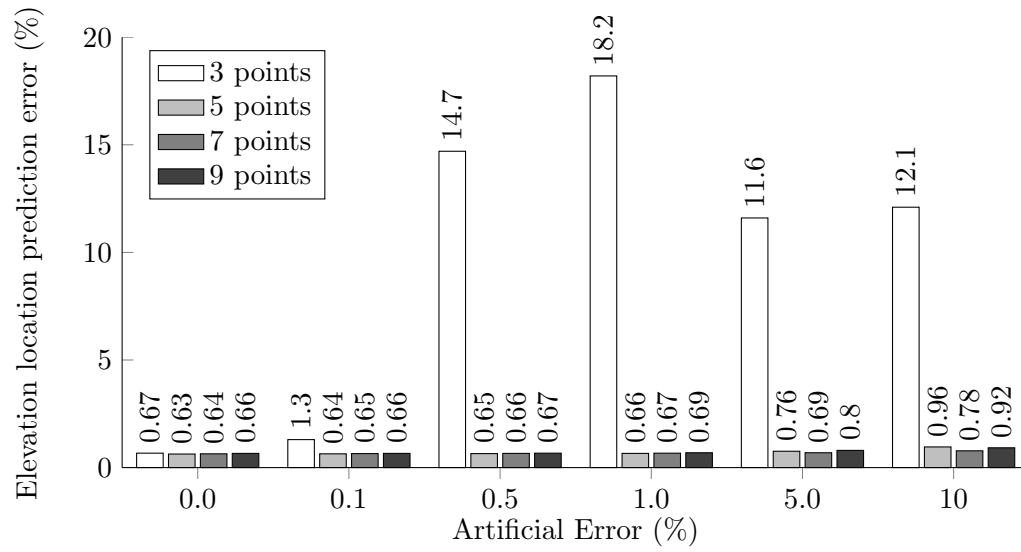
Figure 5.23: Elevation location prediction error(%) produced from artificially adding error to sample points
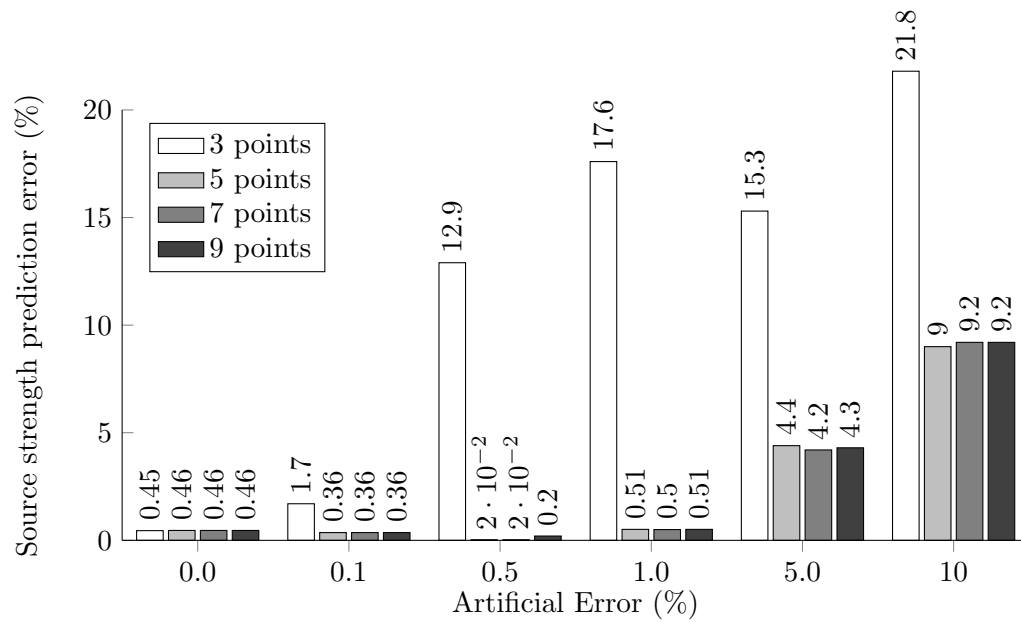


Figure 5.24: Source strength prediction error(%) produced from artificially adding error to sample points

# Chapter 6

# Example Problem: Jet in a Crossflow

## 6.1 Introduction

Similar to the plume in a crossflow, the jet in a crossflow problem includes a stream of air perpendicular to the free stream. This adds to the momentum of the thermal buoyancy driven plume. It also adds another parameter needing to be solved for $U_S$. Unlike the plume case, the jet can have a momentum of similar magnitude or greater than that of the crossflow.

The jet in a crossflow is probably best envisioned as a smoke stack, however, many other industrial applications exist. Another such application is a gas turbine burner[40]. The goal of this inverse problem is to solve for the location, strength, and velocity of the source.

### 6.1.1 Physics of the Forward Problem

The jet in a crossflow physics are nearly identical to those of the plume in a crossflow. A list of the important non-dimensional parameters is shown in table 6.1. A thorough explanation of the flow parameters is in appendix A.1. From this we can determine that the flow is usually in the turbulent regime, and that the flows are too slow to fall into the compressible regime. Viscous effects, again, must be modeled to allow turbulence to develop, propagate, and dissipate.

## 6.2 Experimental Apparatus

The experimental apparatus consists of the same wind tunnel and all accompanying hardware. The test section floor is removable and was replaced with a two-dimensional

| Non-Dimensional Parameter | Symbol | Range | Flow Regime |
|---|---|---|---|
| Grashoff number | $Gr$ | $\approx 10^5 - 10^6$ | ratio of buoyancy to viscous forces |
| Rayleigh number | $Ra$ | $\approx 10^7$ | plume stability |
| Reynolds number | $Re_j$ | $\approx 10^3 - 10^4$ | ratio of inertial to viscous forces (jet) |
| Reynolds number | $Re_\infty$ | $6 \times 10^3$ | ratio of inertial to viscous forces (free stream) |
| Richardson number | $Ri$ | $\approx 10^3 - 3$ | ratio of natural to forced convection |

Table 6.1: Non-dimensional parameters for jet in a crossflow

jet, which is diagrammed in figure 6.1. The new floor of the test section is made from a $25.4\,mm$ thick sheet of acrylic. The jet is produced via compressed air, which passes through two $700\,W$ cartridge heaters, model Omega AHP-7561. The jet has a maximum temperature of $425\,K$ due to material limitations. The maximum jet velocity is up to $5\,m/s$ due to air delivery restrictions.

The jet velocity is calculated from volumetric flow rates into the chamber and verified with a Pitot-static probe. The maximum error utilizing the volumetric flow rate method is $0.2\,m/s$. The error associated with the differential pressure sensor connected to the Pitot-static tube results in a maximum error of $0.018\,m/s$.

## 6.3 Methodology

Due to the extra parameter needing to be solved for, the jet in a crossflow methodology is slightly different from the plume methodology described in chapter 3. Knight et al. [25] used a quardratic response surface model to determine the source strength(temperature and velocity). This method, however, is not easily applied to the situation of unknown source location. The response surface model equation (6.1) (rewritten from [25], utilizing this works nomenclature) cannot be rewritten such that both $T_S$ and $U_S$ are on the
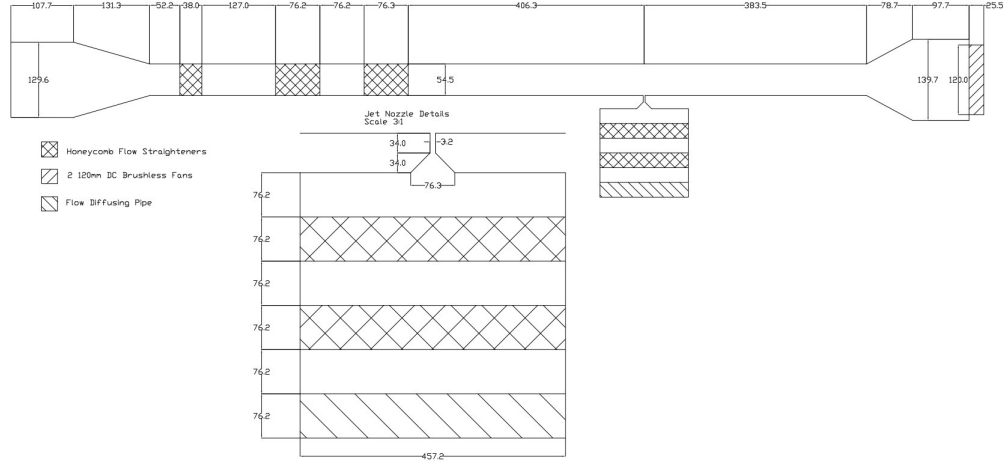
Figure 6.1: Schematics of the wind tunnel with the jet installed

left hand side of the equation. Therefore, a slightly different approach is needed: the complete separation of temperature and velocity.

$$T(\boldsymbol{r}) - T_\infty = (T_S - T_\infty) \left( \beta_0(\boldsymbol{r}) + \beta_1((\boldsymbol{r}) \left[ U_S/U_\infty \right] + \beta_2(\boldsymbol{r}) \left[ U_S/U_\infty \right]^2 \right) \qquad (6.1)$$

The method starts similar to that described previously, where $n$ samples of unknown source strength(temperature and velocity) and location are acquired, followed by simulating $d$ test domains spanning the thermal and velocity region of interest. This is where this new method deviates. A guess of the source velocity($U_S$) so $m(\boldsymbol{r})$ and $b(\boldsymbol{r})$ are not dependent upon an unknown $U_S$. Calculate $m(\boldsymbol{r})$ and $b(\boldsymbol{r})$ from equation (3.1). Find the minimization of $F(\boldsymbol{r})$ from equation (3.3) and calculate the source temperature $T_{SP}$ from equation (3.4).

If we neglect variations in density and thermal buoyancy effects, the local temperature should be a quadratic function of the jet velocity. After many samples and tests, this assumption is proven to be errant. Unfortunately, no other simply defined curve-fit follows the function with better accuracy than a quadratic curve-fit and thus, it will be used.

If we hold the source temperature constant, then equation (6.2) can be used to calculate the source velocity, but only if we can determine the coefficients $\alpha_0$, $\alpha_1$, and $\alpha_2$. Following the same logic used in developing $F(\boldsymbol{r})$, we can develop $G(\boldsymbol{r})$ in

equation (6.3) based upon equation (6.2). The minimization of $G(\boldsymbol{r})$ results in $r_{SP}$, which can then be used to calculate $U_{SP}$ from equation (6.4). This process is repeated until $\Delta U_{SP} < \epsilon_U$ and $\Delta T_{SP} < \epsilon_T$, where $\epsilon_U$ and $\epsilon_T$ are some small values such as $0.1K$ and $0.01m/s$ respectively. As an extra check, one can compare the values $\boldsymbol{r}_{SP}^*$ and $\boldsymbol{r}_{SP}$. These values should be in agreement with each other. A flowchart of this modified methodology is shown in figure 6.2.

$$U_S = \Gamma_2\left(\boldsymbol{r}\right)T\left(\boldsymbol{r}\right)^2 + \Gamma_1\left(\boldsymbol{r}\right)T\left(\boldsymbol{r}\right) + \Gamma_0\left(\boldsymbol{r}\right) \tag{6.2}$$

$$
\begin{aligned}
G\left(\boldsymbol{r}\right) = \sum_{i=a}^{n}[&\Gamma_2\left(\boldsymbol{r}+\boldsymbol{\Delta}_i\right)T\left(\boldsymbol{r}_i\right)^2 \\
&+\Gamma_1\left(\boldsymbol{r}+\boldsymbol{\Delta}_i\right)T\left(\boldsymbol{r}_i\right) \\
&+\Gamma_0\left(\boldsymbol{r}+\boldsymbol{\Delta}_i\right) \\
&-\Gamma_2\left(\boldsymbol{r}\right)T\left(\boldsymbol{r}_0\right)^2 \\
&-\Gamma_1\left(\boldsymbol{r}\right)T\left(\boldsymbol{r}_0\right) \\
&-\Gamma_0\left(\boldsymbol{r}\right)]^2
\end{aligned}
\tag{6.3}
$$

$$
\begin{aligned}
U_{SP} = \frac{1}{n-a}\{\sum_{i=a}^{n-a}[&\Gamma_2\left(\boldsymbol{r}_{SP}+\boldsymbol{\Delta}_i\right)T\left(\boldsymbol{r}_i\right)^2 \\
&+\Gamma_1\left(\boldsymbol{r}_{SP}+\boldsymbol{\Delta}_i\right)T\left(\boldsymbol{r}_i\right) \\
&+\Gamma_0\left(\boldsymbol{r}_{SP}+\boldsymbol{\Delta}_i\right)]\}
\end{aligned}
\tag{6.4}
$$

## 6.4   Simulation

The jet simulation settings and conditions are nearly identical to the plume simulations, but repeated here for completeness. The simulations were performed using the software package Ansys Fluent version 13 [2]. The Navier-Stokes equations were solved using a three-dimensional, steady-state, realizable $k-\epsilon$ model with enhanced wall effects. The exact governing equations solved are documented in appendix A.8.3. The three-dimensional model is employed due to a limitation of Fluent, which is solid-solid conduction is not modeled in two-dimensional conjugate heat transfer problems.

The origin is located at the upstream edge of the jet. The axial downstream direction is $+x$. Normal to the heated surface is $+y$. Gravity acts in the $-y$ direction.
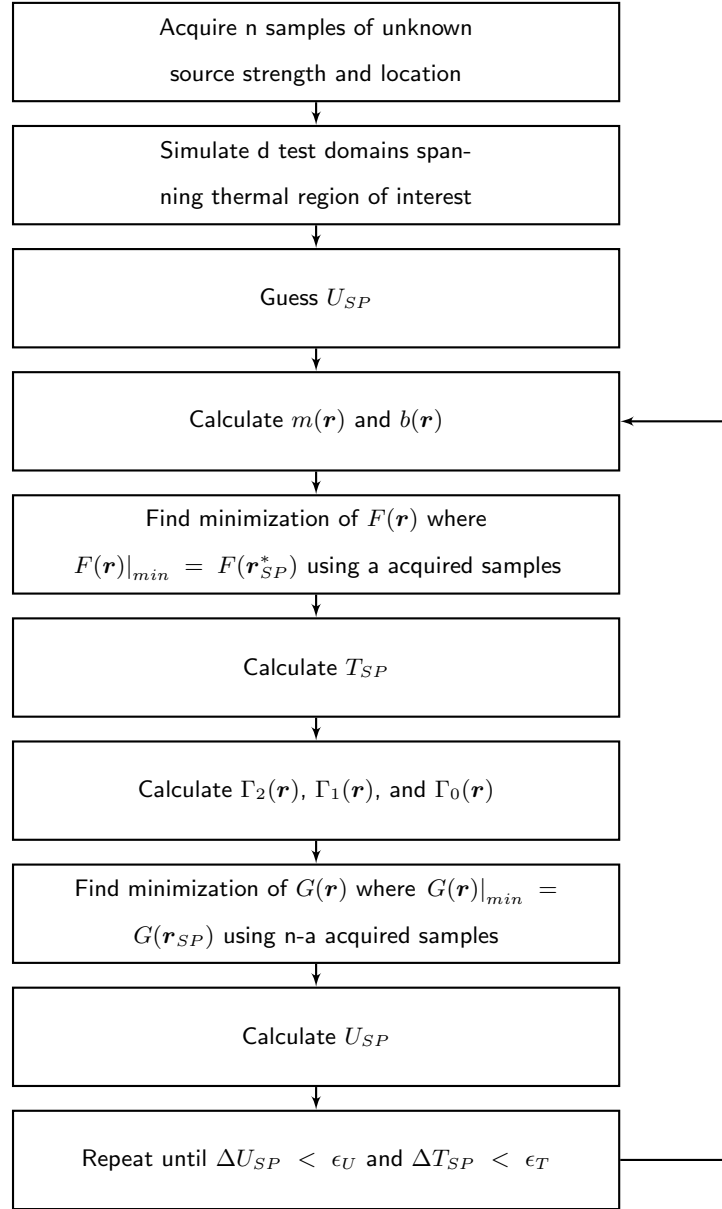
Figure 6.2: Flow chart of the predictor - corrector methodology for a jet in a crossflow

The working fluid is air and modeled as an ideal gas at atmospheric pressure. Fluid properties such as viscosity were calculated according to the model described in appendix A.5.

The boundary conditions at the free stream inlet are described as:

$$u = U_\infty, v = 0, T = T_\infty, P = P_\infty, l = 4mm, I = 5\% \tag{6.5a}$$

$$k = \frac{3}{2} (U_\infty I)^2 \tag{6.5b}$$

$$\epsilon = C_\mu^{3/4} \frac{k^{3/2}}{l} \tag{6.5c}$$

The jet is modeled as a velocity inlet with constant velocity at the bottom of a $25.4\,mm$ deep channel with a width of $3.2\,mm$. All of the parameters of the jet are listed below:

$$u = 0, v = U_S, T = T_S, P = P_\infty, l = 4mm, I = 5\% \tag{6.6a}$$

$$k = \frac{3}{2} (U_\infty I)^2 \tag{6.6b}$$

$$\epsilon = C_\mu^{3/4} \frac{k^{3/2}}{l} \tag{6.6c}$$

The upper boundary was chosen to be symmetric to reduce the possibility of errors introduced by the experimentally accurate no-slip condition. This is acceptable since the upper boundary is very far from the jet and thus, should have negligible effect on the numerical result. The exit boundary is a simple pressure outflow set to $P_\infty$.

The bottom boundary consists of wind tunnel flooring and test section flooring. The wind tunnel flooring is made from $12\,mm$ thick acrylic, while the test section flooring is $25.4\,mm$ thick acrylic. All external solid boundary conditions are iso-thermal with a temperature of $T_\infty$, except for the test section, which is iso-thermal with a temperature of $\frac{1}{2} (T_S + T_\infty)$.

## 6.5 Simulation Validation

A simulation validation study for the jet in a crossflow was performed covering the typical studies: flow model, grid independence, iterative convergence, and a comparison with experimental results. The conditions of the validation study are shown in table 6.2.

| Parameter | Value |
|-----------|-------|
| $U_\infty \, (m/s)$ | $2.0 \pm 0.02$ |
| $U_S \, (m/s)$ | $2.0 \pm 0.2$ |
| $T_\infty \, (K)$ | $305 \pm 0.5$ |
| $P_\infty \, (kPa)$ | $101.3 \pm 0.01$ |
| $T_S \, (K)$ | $350 \pm 2.0$ |

Table 6.2: Validation test conditions

### 6.5.1 Flow Model

Three flow models were used to validate the flow model selection: Spalart-Allmaras, $k - \epsilon$, and $k - \omega$. A complete description of each model is described in appendix A.8. The data is normalized using equation (6.7), where $D$ is the width of the jet. Two plots are used to demonstrate the differing flow models, figures 6.3 and 6.4. They are located at $X = 3.15$ and $X = 4.75$ respectively. Both plots have $k - \epsilon$ and $k - \omega$ in close agreement with Spalart-Allmaras varying greatly. The Spalart-Allmaras model does have a similar trend, but is incapable of properly modeling this particular type of problem. Since $k - \epsilon$ and $k - \omega$ are in such close agreement, we can say that the flow models most likely capture all of the relevant physics.

$$\phi = \frac{T - T_\infty}{T_S - T_\infty} \tag{6.7a}$$

$$X = \frac{x}{D} \tag{6.7b}$$

$$Y = \frac{y}{D} \tag{6.7c}$$

$$V = \frac{U}{U_\infty} \tag{6.7d}$$

$$V_S = \frac{U_S}{U_\infty} \tag{6.7e}$$

### 6.5.2 Grid Independence

As was done with the plume in a crossflow, the cell count will be varied and the temperature at a number of locations will be checked do demonstrate their values to
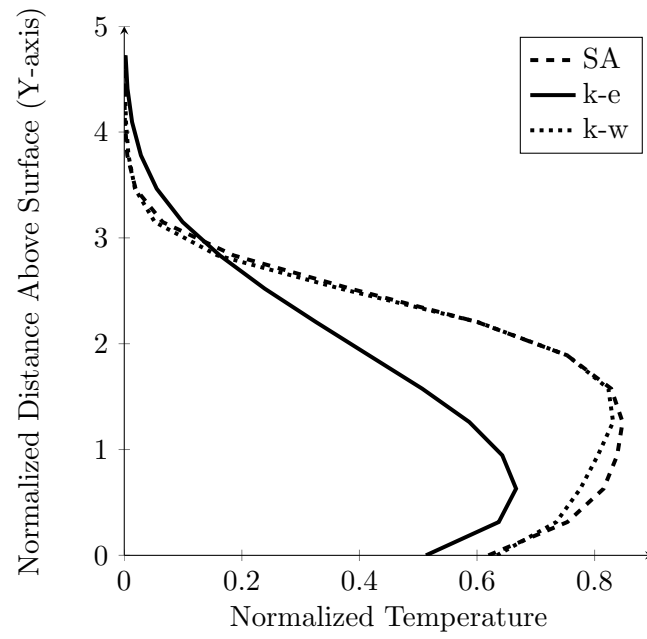
Figure 6.3: Validation of the simulation: local temperature using three flow models at $X = 3.15$
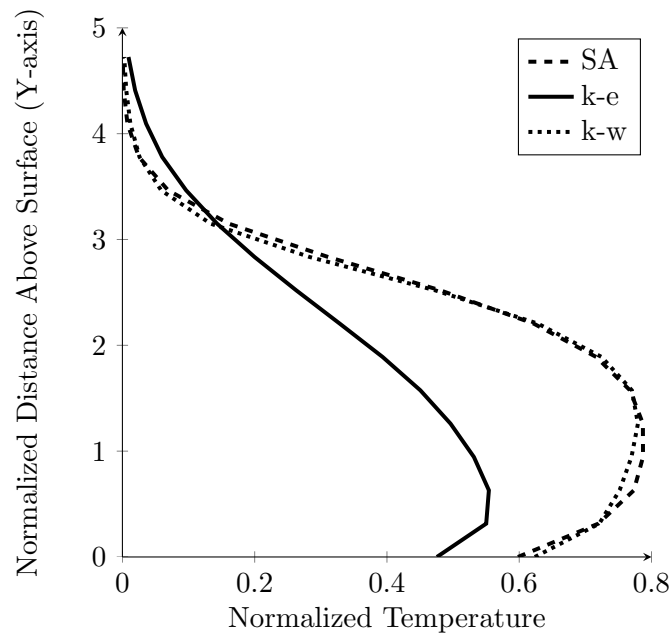


Figure 6.4: Validation of the simulation: local temperature using three flow models at $X = 4.75$

| Location (x,y) (mm) | 0,1 | 10,5 | 15,5 | 30,10 |
|---|---|---|---|---|
| Cell Count | | | | |
| 57660 | 337.7 | 323.3 | 321.6 | 310.1 |
| 83888 | 337.7 | 323.3 | 321.6 | 310.1 |
| 166352 | 337.7 | 323.2 | 321.5 | 310.1 |
| 366168 | 337.7 | 323.2 | 321.5 | 310.1 |

Table 6.3: Grid Independence Study, local static temperature (K)

not change. Table 6.3 shows four different cell counts at four different locations. The temperature varies no more than $0.1K$, and therefore, we can conclude the domain does not depend upon the grid. The grid is an unstructured, hexagonal mesh with a focus upon the area inside the jet entrance and downstream of the jet.

### 6.5.3  Iterative Convergence

The typical method of proving iterative convergence is to increase the residual requirements. In the case of the jet in a crosswind problem, large differences in grid sizing requires that limit to be at least $10^{-8}$ for all parameters. Figures 6.5 and 6.6 are two slices of the domain, located at $X = 3.15$ and $X = 4.75$. The slices are errors with respect to the $10^{-8}$ case. Due to issues with the extremely small elements inside the jet, the system does not adequately converge until $10^{-5}$ and probably should use $10^{-6}$ to be safe. If we use $10^{-6}$ residual requirements, it is safe to assume that the jet in a crossflow is likely to have converged iteratively.

### 6.5.4  Comparison to Experiment

As with the previous validation studies, two slices of the experiment versus simulation are used to validate the simulation. Again, both slices are at $X = 3.15$ and $X = 4.75$ for figures 6.7 and 6.8 respectively. Both slices give good agreement between the experiment and the simulation, although not as accurate as one would want. One area of concern is the trend near the wall in figure 6.8 where the experiment and the simulation diverge.
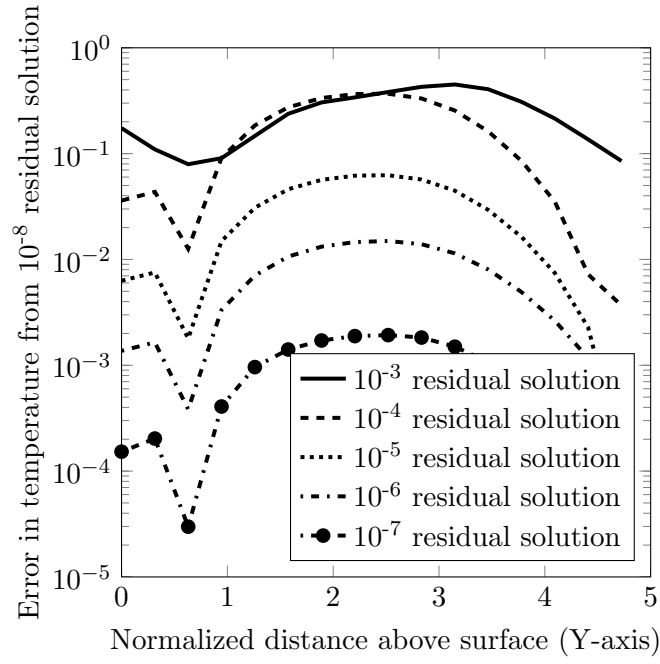
Figure 6.5: Validation of the simulation: local temperature error vs residuals set to $10^{-8}$ at $X = 3.15$
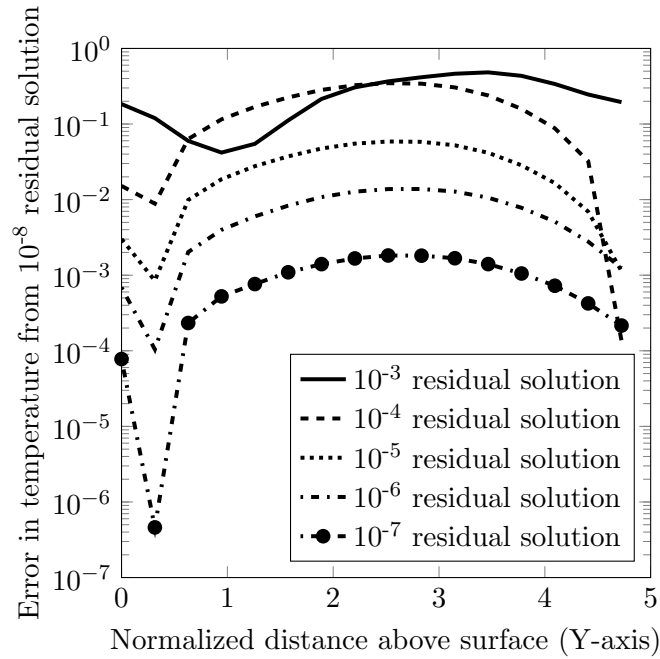


Figure 6.6: Validation of the simulation: local temperature error vs residuals set to $10^{-8}$ at $X = 4.75$
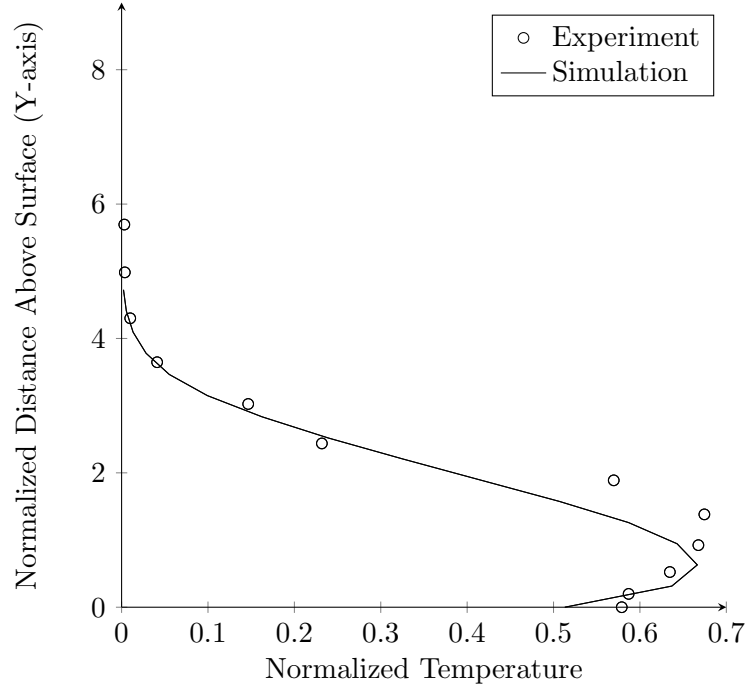
Figure 6.7: Validation of the simulation: local temperature - experiment versus simulation at $X = 3.15$

This issue is most likely due to the problems with resolving near wall fluid conditions within the models chosen.

Hot-wire anemometer data for the wind tunnel was already covered in section 5.5.4. Simulation data versus the hot-wire anemometer data for the jet is shown in figure 6.9, where $X = 0$ is the center of the jet. The simulation and experiment compare favorably and we can assume the simulation properly models the important jet physics. The jet velocity test conditions are in table 6.4. Due to the expansion of the compressed air, additional heat was needed to bring the jet temperature back up to ambient temperature.

## 6.6   Results

An incremental approach to solving the jet problem was used. Starting with the simplest cases working towards the most difficult, and finally adding in the complexity that is the experimental results. There are twenty-four selected cases used to demonstrate
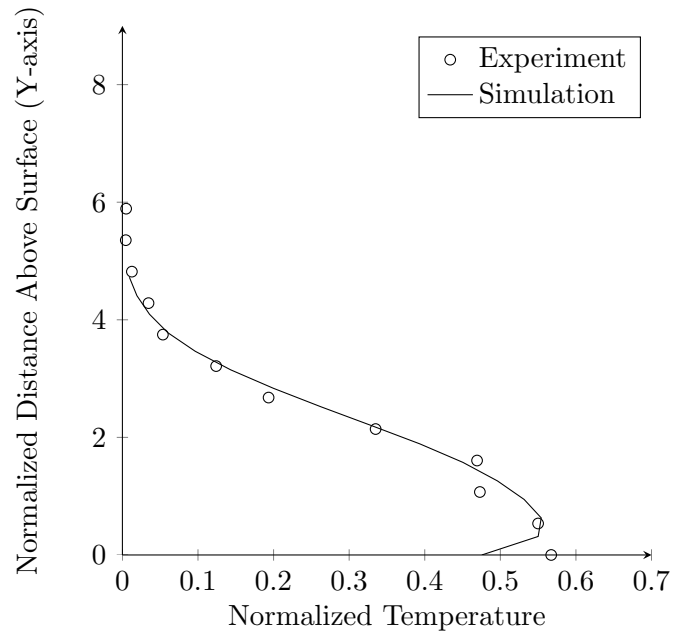
Figure 6.8: Validation of the simulation: local temperature - experiment versus simulation at $X = 4.75$
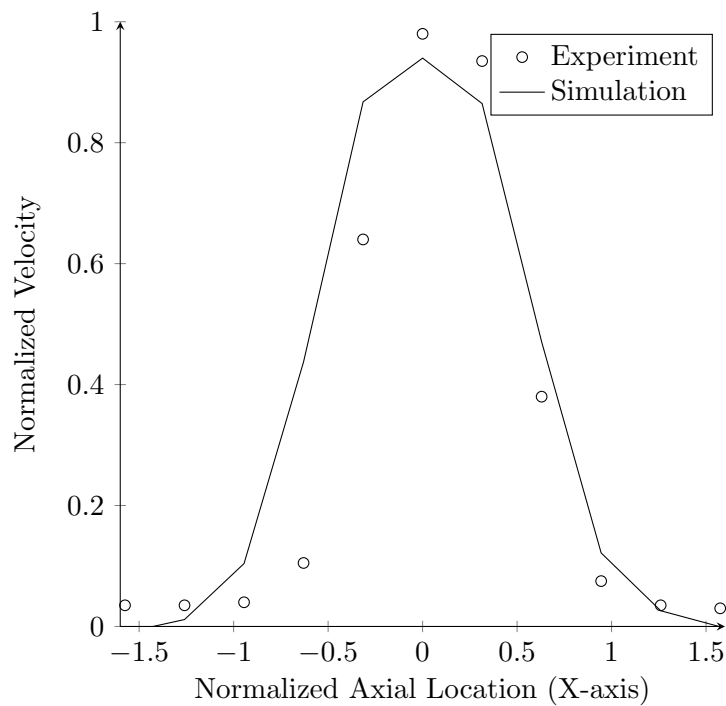


Figure 6.9: Validation of the simulation: jet velocity - experiment versus simulation, no crossflow, ambient jet temperature. Axial slice at $Y = 0.63$

| Parameter | Value |
|---|---|
| $U_\infty\ (m/s)$ | 0 |
| $U_S\ (m/s)$ | $2.0 \pm 0.05$ |
| $T_\infty\ (K)$ | $298.5 \pm 0.5$ |
| $P_\infty\ (kPa)$ | $102.6 \pm 0.01$ |
| $T_S\ (K)$ | $298.5 \pm 2.0$ |

Table 6.4: Jet velocity validation test conditions

| $U_S\ (m/s)$ | 1 | 1 | 2 | 2 | 4 | 4 |
|---|---|---|---|---|---|---|
| $T_S\ (K)$ | 375 | 425 | 375 | 425 | 375 | 425 |
| Location (x,y) | | | | | | |
| 10 mm, 1 mm | A | B | C | D | E | F |
| 10 mm, 3 mm | G | H | I | J | K | L |
| 20 mm, 1 mm | M | N | O | P | Q | R |
| 20 mm, 3 mm | S | T | U | V | W | X |

Table 6.5: Several sampled case parameters

the capabilities of the described methodology. The cases are labeled A-X, and the conditions are listed in table 6.5. Non-varying parameters are listed in table 6.6.

| Parameter | Value |
|---|---|
| $U_\infty\ (m/s)$ | 2 |
| $T_\infty\ (K)$ | 293 |
| $P_\infty\ (kPa)$ | 101.3 |

Table 6.6: Simulation test conditions

The next two steps utilize a single sample point, however, the rest use the nine sample points listed in table 4.5. The search shape used here is the optimized search shape for a plume with all nine sample points included. Utilizing a jet optimized search shape may yield better results.
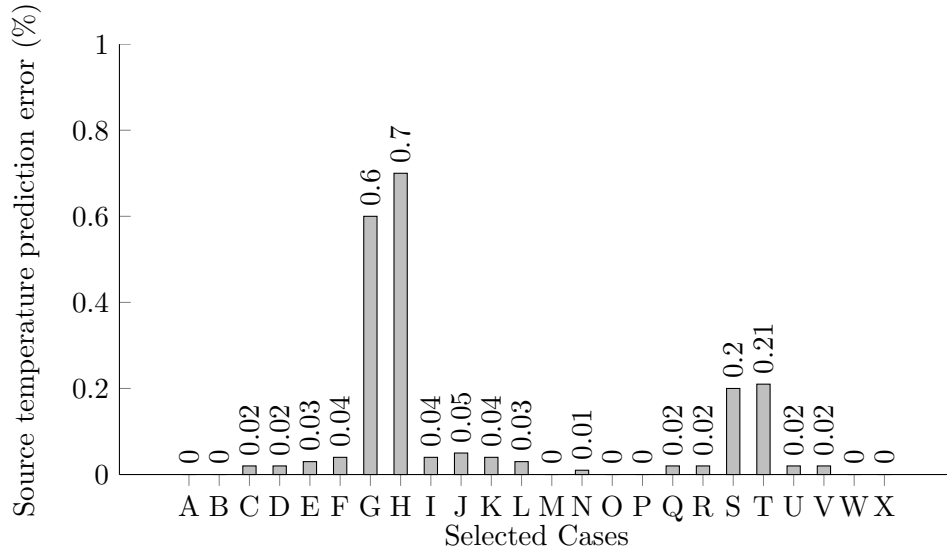
Figure 6.10: Error in the prediction of $T_S$ from several sampled cases within the jet with $\boldsymbol{r}_S$ and $U_S$ known

### 6.6.1 Source Location and Velocity Known

The first step is unknown source temperature, the methodology breaks down to a simple linear equation similar to that of the plume case. The linear equation allows the use of a single sample point to solve the inverse problem. The results of the selected cases are shown in figure 6.10. The error is typically less than 0.1%, except in four cases. The four cases with large error are located outside or near the edge of the jet. The temperature at these locations is near ambient and the Matlab polynomial curve fit has issues with the data points very similar to each other, often giving results of magnitude $10^{\pm 10}$ or worse. What this means is that the error for these four points is essentially caused by machine error.

### 6.6.2 Source Location and Temperature Known

Another simple case is that of the when the source velocity is not known. This step also breaks down to a relatively simple equation, but this time the equation is that of equation (6.2) and thus quadratic. This particular equation does not perfectly model the velocity profile, but as is seen in figure 6.11, it is still good. The error associated
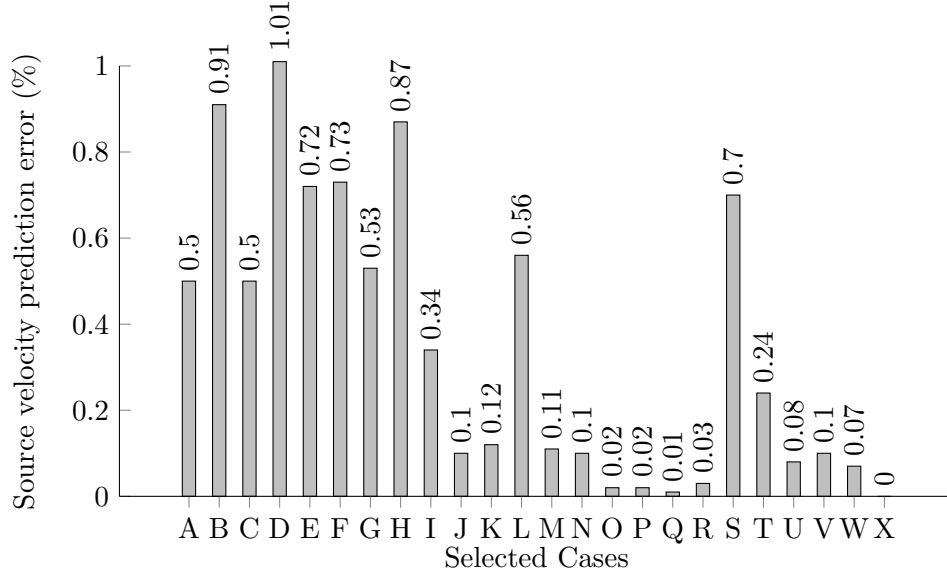
Figure 6.11: Error in the prediction of $U_S$ from several sampled cases within the jet with $\boldsymbol{r}_S$ and $T_S$ known

with this is never more than $\approx 1\%$, which is likely less than that of any experimental error. In this case, it is certainly less than the experimental error. Again, the simulation parameters are described in tables 6.5 and 6.6.

### 6.6.3 Source Location Known

Step three is a bit more complicated. The method would ideally breakdown to that of the response surface model of Knight et al. [25]. This however, cannot be the case as the methodology has the two equations separated and thus, they still need to be solved iteratively. The selected cases are shown in figures 6.12 and 6.13, and are of the error in predicting the source temperature and velocity. A few of the selected cases improved in accuracy due to the increase in the number of sample points.

### 6.6.4 Source Elevation Known

This is the next logical step, and only the source elevation is known a priori. Figures 6.14 to 6.16 are bar charts containing the error associated with predicting the source temperature, velocity, and axial location, respectively. The charts are of the
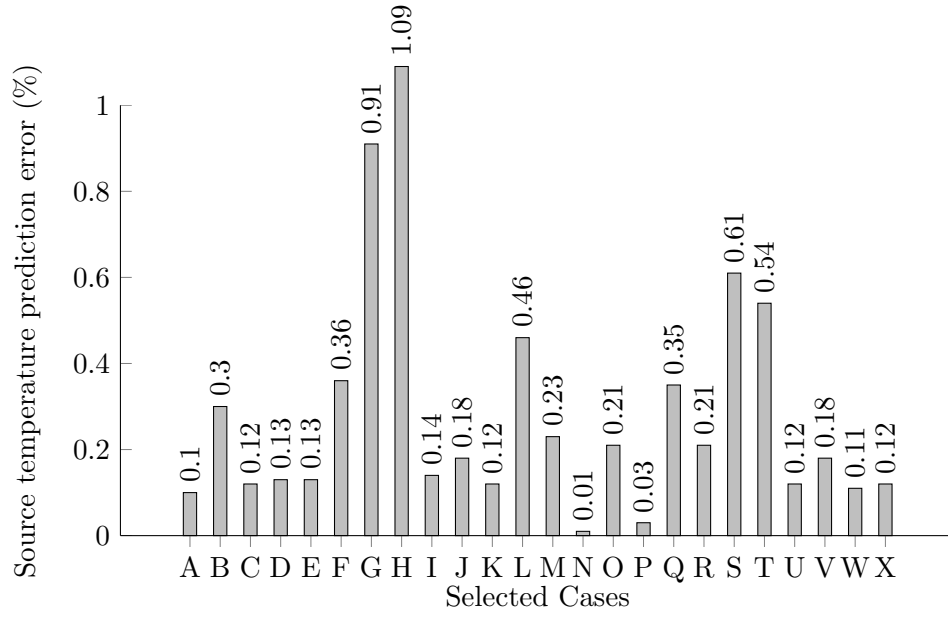
Figure 6.12: Error in the prediction of $T_S$ from several sampled cases within the jet with $\boldsymbol{r}_S$ known
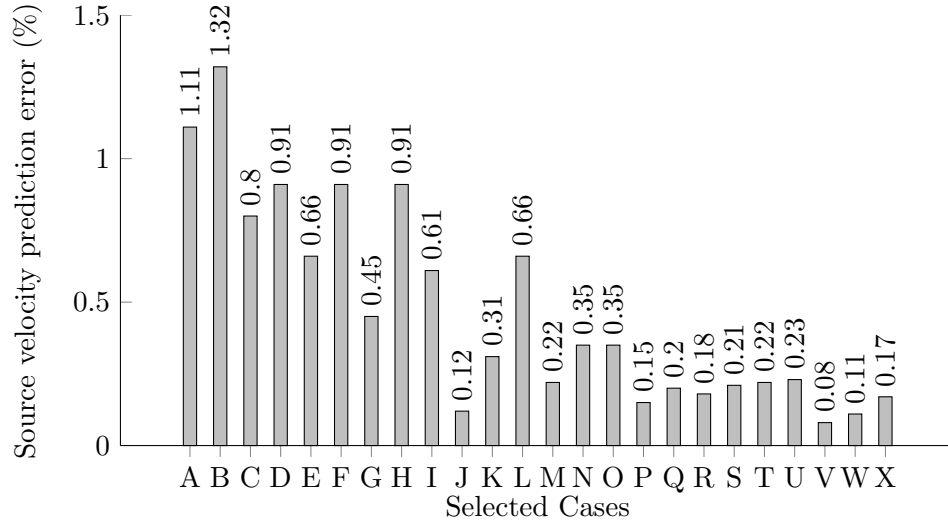


Figure 6.13: Error in the prediction of $U_S$ from several sampled cases within the jet with $\boldsymbol{r}_S$ known
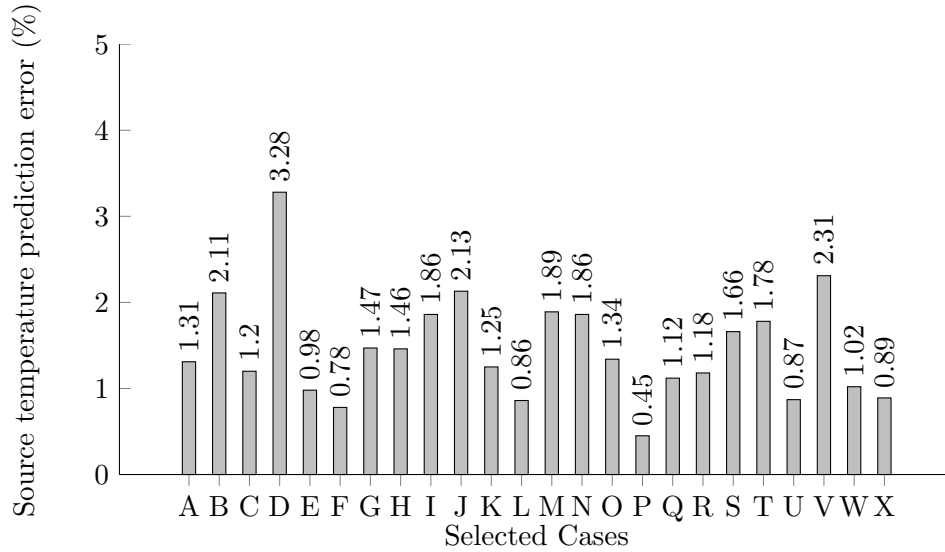
Figure 6.14: Error in the prediction of $T_S$ from several sampled cases within the jet with source elevation known

same selected cases of table 6.5. The error is significantly increased to higher than 9% for predicting the source velocity. Even an error of 9% is still reasonable, but the methodology does not seem to function as well for the jet in a crossflow problem. This is likely due to not utilizing an optimized search shape for the jet, even though nine sample points were used.

### 6.6.5 Source Location and Strength Unknown

The last step with source location and strength unknown is not possible with the current search shape and methodology. The issue in this case is the self-similar nature of a jet in a crossflow, where there are multiple solutions to the problem. That is to say that the nine point search shape can converge on multiple solutions.

This is similar to the problem with the plume in a crossflow prior to using the new optimized search shape. In that problem, the solutions all had the same predicted source temperature, with different locations with the same search shape. This problem has completely unique solutions with the same search shape.

When searching the domain for alternative solutions, a search space of $350 - 450\,K$
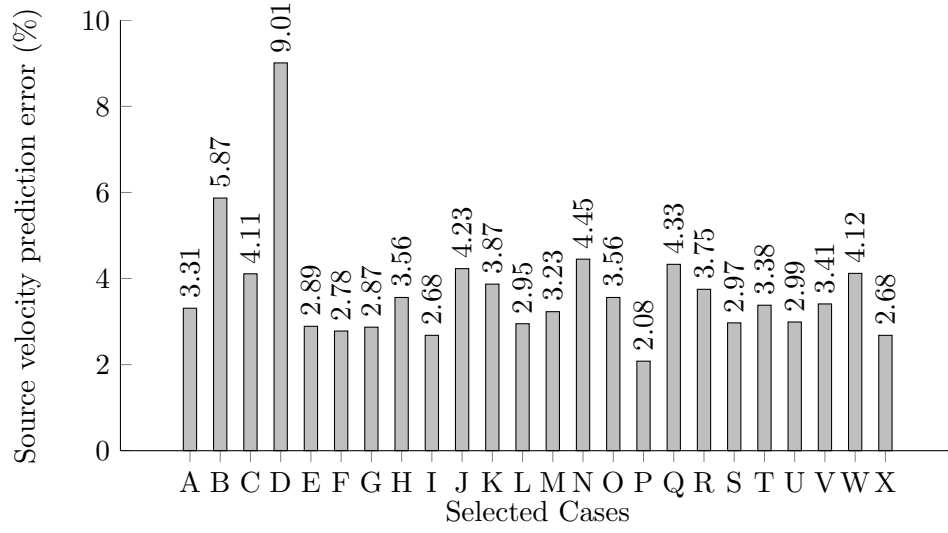
Figure 6.15: Error in the prediction of $U_S$ from several sampled cases within the jet with source elevation known
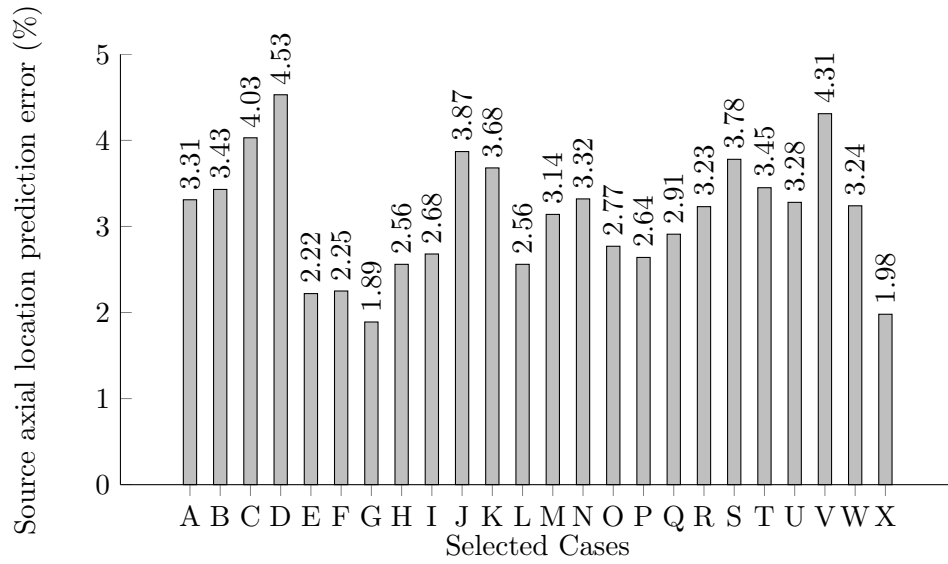


Figure 6.16: Error in the prediction of $x_S$ from several sampled cases within the jet with source elevation known

| Axial Loc. $(mm)$ | Elev. Loc. $(mm)$ | Jet Temp. $(K)$ | Jet Vel. $(m/s)$ | Search Shape Error (%) |
|---|---|---|---|---|
| 20.0 | 3.0 | 425 | 2.0 | 0.00 |
| 10.0 | 3.7 | 375 | 2.5 | 0.60 |
| 12.0 | 5.1 | 375 | 3.0 | 0.34 |
| 14.8 | 2.7 | 400 | 2.0 | 0.30 |
| 16.3 | 4.5 | 400 | 2.5 | 0.26 |
| 19.5 | 5.9 | 400 | 3.0 | 0.29 |
| 21.8 | 5.0 | 425 | 2.5 | 0.24 |
| 25.6 | 6.5 | 425 | 3.0 | 0.34 |
| 25.2 | 3.2 | 450 | 2.0 | 0.13 |
| 26.8 | 5.4 | 450 | 2.5 | 0.25 |

Table 6.7: Example alternative solutions

in $25\,K$ increments and $0-4\,m/s$ in $0.5\,m/s$ increments were used. Take the 'V' case for example, there are nine alternative solutions with less than 1% error difference between the search shape temperatures. Table 6.7 is a list of all of the alternatives, including the 'V' case at the top of the table. The alternatives seem to be discernible knowing the elevation, which is why the previous step was able to be resolved.

### 6.6.6 Experimental Results

Due to the issue in determining the four unknowns, the experimental results are limited to finding only axial location and source strength. The conditions of the experiments are shown in table 6.8. The results from a few select cases are shown in table 6.9. Due to the severe addition of error to the experimental results, the results are shown in a table format rather than the previously used bar graphs.

The error predicting the axial location is as high as 18.7%. The error in predicting source velocity is as high as 21.8%. The error for source temperature is as high as 13.7%. These high error rates should be expected, as there are many contributing factors. The

| Parameter | Value |
|---|---|
| $T_\infty\,(K)$ | $297.6 \pm 8.0$ |
| $P_\infty\,(kPa)$ | $100.6 \pm 0.6$ |
| $U_\infty\,(m/s)$ | $2.0 \pm 0.02$ |

Table 6.8: Experimental test conditions

search shape is not optimized for the jet, the number of sample points may not be enough, and the simulations do not exactly follow the experiment. Even with these issues, the methodology was able to predict close to, if not within, experimental error. Realize that 20% of $1.0\,m/s$ is the accuracy of the experimental jet velocity.

| $U_S\,(m/s)$ | | 1.0 | 1.0 | 4.0 | 4.0 |
|---|---|---|---|---|---|
| $T_S\,(K)$ | | 375 | 425 | 375 | 425 |
| Location (x,y) | | | | | |
| 10 mm, 0 mm | X | 10.9% | 11.7% | 11.1% | 13.8% |
| | U | 21.8% | 18.6% | 10.4% | 11.9% |
| | T | 8.70% | 9.87% | 10.7% | 12.9% |
| 20 mm, 0 mm | X | 8.65% | 7.65% | 5.40% | 9.81% |
| | U | 18.7% | 19.8% | 11.5% | 12.1% |
| | T | 8.81% | 10.7% | 9.65% | 10.2% |
| 30 mm, 0 mm | X | 10.6% | 10.4% | 18.7% | 9.78% |
| | U | 15.8% | 17.9% | 12.3% | 13.7% |
| | T | 9.61% | 8.64% | 13.7% | 10.1% |

Table 6.9: Error in predicting source axial location $(x_S)$, source strength$(U_S$ and $T_S)$ from a few sample cases within the jet, search shape with 9pts, utilizing experimental data
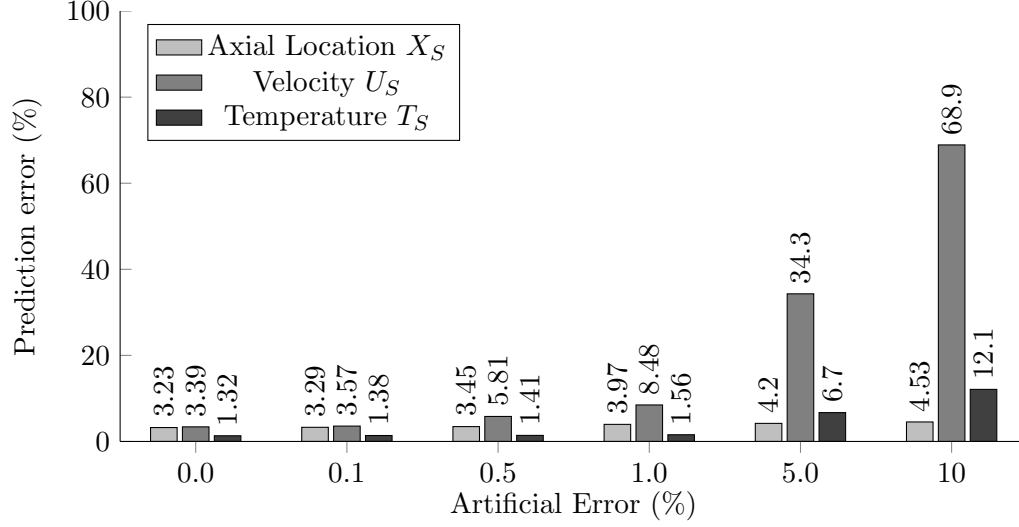
Figure 6.17: Source prediction error(%) produced from artificially adding error to sample points

### 6.6.7 Error Analysis

The error analysis was performed similarly to that of the plume error analysis. An artificial error was added to the sample points and the median error of the twenty-four selected cases was taken. For the jet in a crossflow, only the condition of nine sample points was used. The results are graphed in figure 6.17. The axial direction prediction error is affected similarly to that of the plume case, that is, very little. The source temperature prediction error also follows similarly, the error follows the same order of magnitude of that of the added error.

The error analysis applied to the source velocity is expected, as the interpolation function is quadratic and thus, any error should propagate in such a fashion. Indeed, the error for the source velocity is of similar magnitude as the square of the additive error. In all three of the error analysis source unknowns, the methodology seems to be remarkably stable in the sense that the error does not significantly affect the results.

# Chapter 7

# Example Problem: Natural Convection from a Finite Heat Source in an Enclosure

## 7.1 Introduction

The plume in a sealed cavity is taking a step back in complexity from the plume in a crossflow. Essentially, this is the special case of a plume with no crossflow, which is achieved through isolation of the plume. This special case arises most often via fires in closed rooms.

If the goal is for eventual use for determining the strength and location of fires in a sealed room, then the sample data must come from the boundaries only. The heat source and the entire domain is off limits and the only access is through a small "sensor wall". This could be a door or a window.

### 7.1.1 Physics of the Forward Problem

The physics of the plume in a sealed cavity is relatively straight forward. The only non-dimensional number having an important impact on the flow is the Rayleigh number. The Rayleigh number's range is between $10^5$ and $10^8$. Thus, the problem would likely be laminar.

## 7.2 Experiment

The experimental apparatus is a sealed cavity of variable dimensions, with $50\,mm$ thick extruded polystyrene(XPS) walls, which has a thermal conductivity of $0.03\,W/m - K$. The cavity can vary in size from $50\,mm$ to $250\,mm$ on any given side. The cavity dimensions are kept such that it is always a cube in shape. The size is allowed to
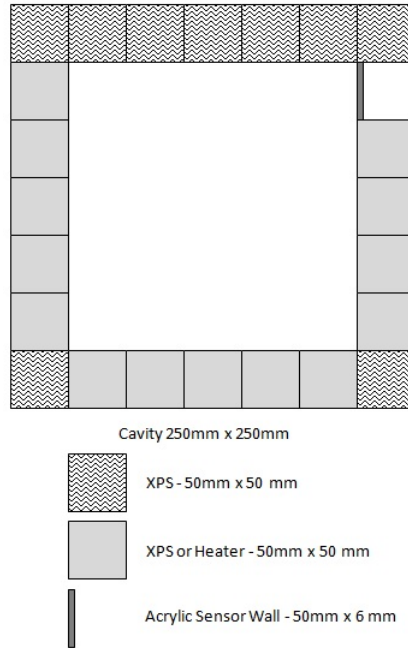
Figure 7.1: Diagram of the sealed cavity

vary to increase the range of Rayleigh numbers capable of being produced, due to the material thermal limitations of approximately $400\,K$. A diagram of the sealed cavity is shown in figure 7.1. The individual blocks are movable such that the heater can be placed in a number of indicated locations. The blocks are also removable to allow for the variable size, one to five blocks wide and high.

The heater consists of a resistance type heater mounted to the bottom of a $12\,mm$ copper block. The copper block is flush mounted inside the same ceramic material used in the plume heater. The heater is rated for a maximum of $50\,W/in^2$. As previously said, the XPS material limits the temperature to $400\,K$.

A heat flux sensor was placed between the heater and the copper to determine exactly how much energy was entering the copper block. The heat flux sensor is Omega model HFS-3, with an error of less than 1% of indicated heat flux.

The aforementioned "sensor wall" is $6\,mm$ acrylic window, with ports for a thermocouple to be mounted. The thinner material, and much higher thermal conductivity, result in a substantial amount of the input heat leaving through the acrylic wall. The

thermocouple probe is a K-type thermocouple, the same one used in the plume and jet experiments. Its calibration is shown in appendix B.

## 7.3    Methodology

Starting from the methodology for the plume, we need to determine if there is any relationship between temperature at a boundary and location of the heat source. As it turns out, the function relating wall temperature and source location is not constant, but very close to constant. So close in fact, that the function will not be useful while utilizing experimental data. Figure 7.2 is a sensitivity analysis of source location versus local temperature. The variation of local temperature to source location is less than $1\,K$ as the heater moves from one side to the other of the enclosure. The sensitivity analysis is based upon experimental data.
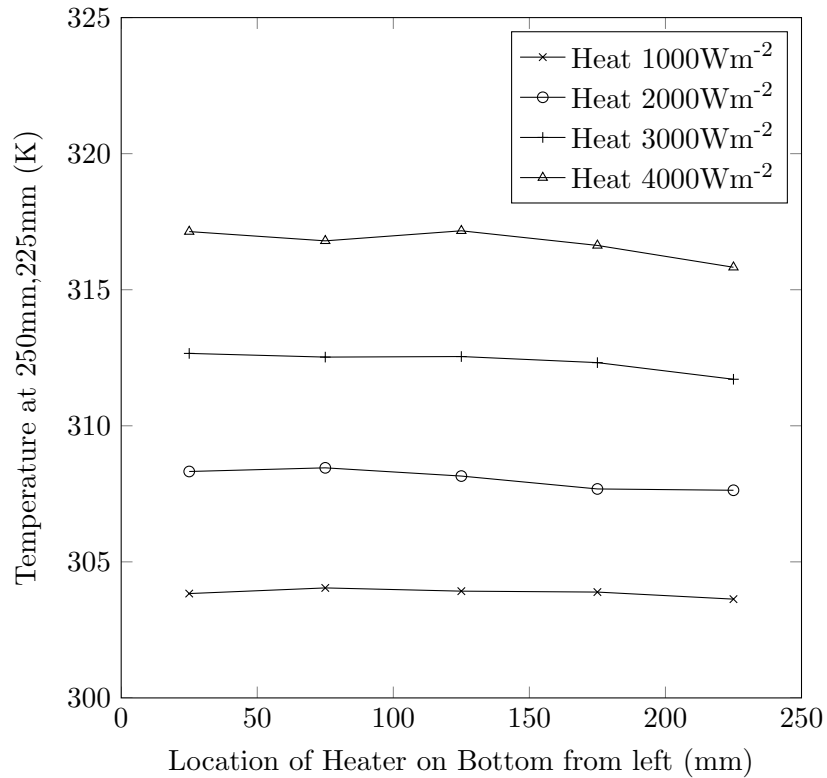


Figure 7.2:   Sensitivity analysis:   source location vs local temperature at $x = 250\,mm$, $y = 225\,mm$

If the location of the source is known, using the same logic used in the plume, the source strength can be calculated. If we neglect the changes in density and buoyancy effects upon the energy equation, then the internal boundary temperature is a linear function of source temperature. This was previously discussed in chapter 3 and the equations are rewritten here, equation (7.1).

$$T_S = m\left(\boldsymbol{r}\right) T\left(\boldsymbol{r}\right) + b\left(\boldsymbol{r}\right) \tag{7.1a}$$

$$m\left(\boldsymbol{r}\right) = \frac{T_{SA} - T_{SB}}{T_A\left(\boldsymbol{r}\right) - T_B\left(\boldsymbol{r}\right)} \tag{7.1b}$$

$$b\left(\boldsymbol{r}\right) = T_{SA} - m\left(\boldsymbol{r}\right) T_A\left(\boldsymbol{r}\right) \tag{7.1c}$$

## 7.4 Simulation

Unfortunately, after many attempts, the simulation and the experiment would not agree enough to justify the simulation-experiment comparison. It is unclear exactly why the simulations don't match the experiment. That being said, one key issue identified is that the convection losses to the walls is much higher in the experiment than they are in the simulations. This is possibly to do with the surface of the XPS material. It is not perfectly smooth and slightly porous, although, it is a closed cell foam. Due to the issues described, all of the data must be generated by the experiment.

## 7.5 Results

The results for the inverse plume in a cavity is overly simple. All of the data needed is contained within figure 7.2. From that figure, $m$ and $b$ can be calculated and thus only the local temperature is needed. A list of $m$ and $b$ is shown in table 7.1.

The error associated with solving the inverse problem becomes just the error associated with the linearity of the function. The results are listed in table 7.2. The error is at a maximum of 4.62%, but typically much less than that, as would be expected.

| Heater Location ($mm$) | $m$ | $b$ |
|---|---|---|
| 25 | 245.8 | $-7.365 \times 10^4$ |
| 75 | 232.9 | $-6.976 \times 10^4$ |
| 125 | 226.6 | $-6.784 \times 10^4$ |
| 175 | 236.2 | $-7.082 \times 10^4$ |
| 225 | 226.0 | $-6.767 \times 10^4$ |

Table 7.1: Inverse parameters for the sealed cavity

| Heater Location ($mm$) | $1000\,W/m^2$ | $2000\,W/m^2$ | $3000\,W/m^2$ | $4000\,W/m^2$ |
|---|---|---|---|---|
| 25 | 0.76% | 0.43% | 0.18% | 0.16% |
| 75 | 4.62% | 3.55% | 0.36% | 0.35% |
| 125 | 2.20% | 0.99% | 0.82% | 0.56% |
| 175 | 1.44% | 1.39% | 0.37% | 0.05% |
| 225 | 0.36% | 0.51% | 0.31% | 0.07% |

Table 7.2: Inverse results for the sealed cavity

# Chapter 8

# Conclusions

A technique combining many aspects of several inverse solution methodologies was developed for the specific use for inverse convection problems. The methodology was applied to and tested against a simple plume in a crossflow. The goal was to predict both the strength and location of the source. It originally used an intuition based search shape, which while proving accurate, required seven sample points to achieve the desired accuracy. The source strength prediction error was better than 1.1% for twenty-four selected cases.

To increase the capabilities, decrease the required sample points, and possibly increase accuracy, a search shape optimization was performed. This optimization reduced the required number of sample points to three. Three sample points proved to be accurate with simulated data to better than 1% for source strength prediction. The number of sample points needed to be increased, from three, to properly handle the error associated with experimental data, to at least five. Utilizing five points, the maximum prediction error was 21%, and for nine sample points, the maximum prediction error dropped to 18%. Although, the median prediction error for the source strength is substantially better at 1.65%, the median prediction error for the axial location and elevation is 0.85% and 2.35%. Error analysis demonstrated that adding 10% error to five sample points would result in a marginal increase in error for location prediction and a source strength error of similar magnitude to the additive error.

The same methodology was applied to another problem, the jet in a crossflow. The goal in this example problem was to predict the velocity, temperature and location of the source jet. In this particular case, the plume in a crosswind optimized search shape was utilized. After some checking, the methodology with this search shape is

incapable of distinguishing all four of the goals. It was determined that the source elevation needed to be known to solve for the other three. The source velocity was predicted to within 1.5% error and source temperature within 3.5% error for selected cases. Utilizing experimental data, the median source velocity was predicted at 14.75% and median source temperature was 9.98%. The median axial location error was 10.5%. Even with a non-optimized search shape, the methodology performed acceptably. Error analysis again demonstrated the stability of the methodology.

The methodology was attempted to be applied to a plume in a sealed cavity. Due to how plumes rise in a chamber, the location prediction was determined not to be possible, at least with this method. Determining the plume source strength breaks down to the simplest of cases of solving an equation. Using a single sample point, the source strength was determined within 5%, utilizing only experimental data. While the methodology is technically being applied, the heart of the methodology is not being tested in this example problem.

There are many paths of continuation of this work. Two of the most important and yet most difficult avenues are three-dimensional and transient capabilities. The third dimension adds complexity in determining where to place the sample points, while increasing the cost of computation significantly. If the third dimension is capable of being added, then it also opens up the possibility of differentiating multiple sources.

Transient analysis requires considerable redesign of the methodology. The sample points would need to be spread across time and thus, adding significant overhead to the algorithm.

A more simple but worthwhile task is to find the optimal search shape for the jet in a crossflow. It would significantly decrease the error associated with that example. Determining an accurate interpolation function for the jet velocity would also decrease the error.

A slightly more daunting task is to find the spatial limiting factors. The methodology applied to the plume in a crossflow functioned so well that the methodology was able to accurately resolve problems at the limits of the simulation. A significant redesign in the experiment and simulation domain is required to continue this work.

The methodology proposed in this work has demonstrated itself to be capable and extremely robust. It has also shown that it is sensitive to the experiment-simulation agreement. A potential drawback of the methodology is that to benefit fully, an optimized search shape must be used, which requires significant computation time. It is possible that this technique could be extended to many applied areas such as environmental flows, room fires, and thermal management systems.

# Appendix A

# Computational Fluid Dynamics

Computational fluid dynamics, or CFD, covers a wide variety of methodologies to solve fluid flow domains. Currently there aren't any all encompassing algorithms which may be used to solve for every domain in every situation. This is mostly due to the limited computational resources available. Direct numerical simulation (DNS) could be an all encompassing algorithm, but requires vast computational resources[5].

This chapter is meant to be a rough introduction to CFD and it covers the exact governing equations used throughout the text. Flow classifications will be covered first, followed by convergence criteria, solution convergence, equation of state, fluid properties, pressure-velocity coupling, discretization, and flow models.

## A.1 Flow classifications

Flow classification can become a chore in of itself. However, there are a few flow classifications which are of most importance to CFD. The flow classifications are laminar-turbulent, viscous-inviscid, and compressible-incompressible. Each of these classifications have a significant bearing on the methods used to solve for the fluid domain. Other more specialty classifications exist, such as single-multiphase flows, which need not be considered in this brief introduction.

### A.1.1 Laminar - turbulent

Turbulent flows are characterized by three-dimensional transient chaotic motions, as opposed to laminar flows which are characterized by smooth laminae fluid bundles, with the Reynolds number being the typical determining factor for laminar or turbulent flows. The Reynolds number is defined as a ratio of inertial forces to viscous forces,

mathematically described in equation A.1.

$$Re = \frac{\rho V^2 L^2}{\mu V L} = \frac{\rho V L}{\mu}$$ (A.1)

If a fully developed flow has a Reynolds number below 2300, it is typically laminar, and above 4000 is typically turbulent[11]. The Reynolds number is more a rule of thumb than a law, however, other factors may come into play such as buoyancy described by the Richardson number.

The Richardson number is a ratio of the Grashof number and Reynolds number. The Grashof number is itself a ratio of buoyancy to viscous forces. Therefore, the Richardson number is actually a ratio of buoyancy forces to inertial forces, i.e. natural convection versus forced convection. The Grashof number is defined in equation A.2.

$$Gr = \frac{g\beta \left(T_s - T_\infty\right) L^3}{\nu^2}$$ (A.2)

The Richardson number is similarly defined in equation A.3.

$$Ri = \frac{Gr}{Re^2} = \frac{g\beta \left(T_s - T_\infty\right) L}{V^2}$$ (A.3)

If the Richardson number is much less than 1, then natural convection may be neglected. If the Richardson number is much larger than 1, then forced convection may be neglected [21]. Even with a Richardson number appropriate such that natural convection cannot be neglected, the buoyancy may not generate any instabilities. For that we need the Rayleigh number to be approximately $10^9$ or higher[12, 21] for a vertical flat plate, but will vary for other conditions.

$$Ra = Gr_x Pr = \frac{g\beta \left(T_s - T_\infty\right) x^3}{\nu\alpha}$$ (A.4)

Most of the problems dealt with in this text have a Reynolds number of order $2 \times 10^3$ and thus turbulence is generated by the plume/jet. Therefore, the entire domain must be modeled as a turbulent problem. Typical ranges of these dimensionless parameters are listed in table A.1.

## A.1.2   Viscous - inviscid

Being inviscid means that the internal frictional forces are zero, that is $\mu = 0$. This is a simplification of the physics, to make solving for the domain much easier. In

|        | Plume                      | Jet                   | Sealed Cavity         |
|--------|----------------------------|-----------------------|-----------------------|
| $Re_\infty$ | $\approx 10^3 - 3 \times 10^3$ | $6 \times 10^3$ | — |
| $Re_j$ | — | $\approx 10^3 - 10^4$ | — |
| $Gr$ | $\approx 10^5 - 10^7$ | $\approx 10^5 - 10^7$ | $\approx 10^5 - 10^8$ |
| $Ri$ | — | $\approx 10^3 - 3$ | — |
| $Ra$ | $\approx 10^5 - 10^7$ | $\approx 10^5 - 10^7$ | $\approx 10^5 - 10^8$ |

Table A.1: Typical range of dimensionless parameters in this text

the case of inviscid cfd, the convergence of the solution is usually much quicker. This simplification has repercussions. In most cases the simplifications make the problem too simple and the mathematical model no longer follows the underlying physics. Inviscid flows cannot impart shear forces upon the boundaries and vice-versa. Without shearing forces, turbulence cannot exist, therefore all inviscid flows are also laminar[11].

Inviscid flow solvers should be used with care and typically only within a preliminary design stage. There are typically only two special cases when it is acceptable to consider using an inviscid flow. The first case is for extremely high Reynolds number flows, which is when the inertial forces are significantly higher than the viscous forces so they may be neglected to some degree. The second case is when the flow is so overly complicated and time consuming to solve with more robust solvers, that it is impractical to solve otherwise. Even with these cases, the final solution to the design should be processed with viscous forces included [3].

### A.1.3   Compressible - incompressible

Incompressible-compressible flows are only marginally more complicated by terminology. Often, what is inferred by the term "incompressible flow" is constant density. Technically speaking, this is an incompressible material. An incompressible flow is one in which equation (A.5) holds true [27]. Any flow which does not satisfy the conditions of incompressibility is considered compressible flow. High velocity fluids are possibly the most common need-to-handle compressibility effects, but not the only reason. Large

thermal gradients, rarefied gases, etc., may also necessitate the inclusion of compressibility effects. This text consists of only incompressible flows.

$$u_i \frac{\partial \rho}{\partial x_i} << \rho \frac{\partial u_i}{\partial x_i} \tag{A.5}$$

## A.2  Convergence Criteria

The convergence of the simulations are based upon a scaled residual value. A residual is defined as the difference between a properties value and its value from the previous iteration. The residuals for each property in each cell are divided by the residuals from the first iteration. A typical means of determining convergence is when residuals drop by three orders of magnitude for all parameters. This is the criterion used, except that the turbulence parameters(e.g. $k$ or $\epsilon$) were increased to four orders of magnitude, due to iteration convergence tests failing.

## A.3  Solution Convergence

Probably the most important aspect of computational fluid dynamics is the question "is the solution a numerically correct solution". There are several ways to test the numerical accuracy, and the best way is to test as many as practical. Typically there are grid independence, iterative convergence, benchmark solutions, and experimental results.

Selecting an appropriate grid generation method is critical to accurate results. That being said, proving that the result is independent of the grid is more important. All computational models must be independent of their grid, as the underlying physics cannot be a function of an imaginary construct[47].

Like grid independence, ensuring iterative convergence occurred is necessary in using results from simulations. As many cfd methods require many iterations, knowing when to stop is important. The simplest method for guaranteeing iterative convergence is by comparing against a solution with very tough convergence criteria. If the two simulations are similar, than the results have probably converged[47].

Benchmark solution tests are the de facto standard for testing simulation results. The simulation results are compared to a known good solution. Benchmark solutions are often of simpler problems, and finding benchmark solutions of more complicated cases may be difficult.

Having experimental results of the exact numerical problem being simulated has its benefits. The experimental results are correct and the model must fit the experiment, or the model is wrong. If there is a difference (there always will be), the difference must be explained as to why it exists, such as not modeling radiation.

## A.4   Equation of State

There are many equations of state developed for use in CFD. The two of primary interest are the incompressible ideal gas law and the Boussinesq model. The incompressible ideal gas law is the familiar ideal gas law shown in equation (A.6). The Boussinesq model was developed to simplify the governing equations when used to calculate natural convection problems to allow for buoyancy[3]. Modern computers seem to have made the approximation a moot point, at least in this case. Several tests were performed and all indicated insignificant processing time and insignificant result differences. In an effort to reduce the possibility of error from the Boussinesq approximations in the later stages of research, all of simulations used the full incompressible ideal gas law.

$$\rho = \frac{PM_W}{RT} \tag{A.6}$$

## A.5   Fluid Properties

Besides density, there are several other fluid properties of interest. Those are the specific heat at constant pressure, thermal conductivity, and viscosity. There are several methods that may be used, such as Sutherland viscosity law. As with the density calculations, effort to keep the results as close to the experimental properties was attempted and the kinetic theory of gases was used to calculate these properties. In this case, the computer run time was negligible between kinetic theory and alternatives, thus it was chosen to utilize kinetic theory for all simulations.

Kinetic theory calculations are very straight forward for specific heat of air near the temperatures of interest. That is specific heat at constant pressure is a constant $C_P = 1006.43 \, J/(kg - K)$.

Dynamic viscosity and thermal conductivity are not so simple and were modeled using equation (A.7). $\mu$ is the dynamic viscosity and $\lambda$ is the thermal conductivity. The Lennard-Jones parameters are constant at $\sigma = 3.711 \, \text{Å}$ and $\frac{\epsilon}{k_B} = 78.6 \, K$. $\Omega_\mu$ is the collision integral for viscosity. For more information regarding the Lennard-Jones parameters, see Ansys [3], Vincenti and Kruger [46].

$$\mu = 2.67 \times 10^{-6} \frac{\sqrt{M_W T}}{\sigma^2 \Omega_\mu \left( \frac{T}{\epsilon/k_B} \right)} \tag{A.7a}$$

$$\lambda = \mu \left( \frac{5}{4} \frac{R}{M_W} + C_P \right) \tag{A.7b}$$

## A.6 Pressure-Velocity Coupling

Ansys Fluent software package offers only four possible coupling options: SIMPLE, SIMPLEC, PISO, coupled. The coupled algorithm is the best for accuracy(typically) and could offer significant convergence speed improvements. For as yet to be determined reasons, the solutions would often diverge when utilized. PISO, due to its inter-step pressure update would be the next choice. For slow plume velocity cases, PISO would also diverge. This limits the options to SIMPLE and SIMPLEC, and since SIMPLEC only modifies SIMPLE to assist in odd shaped cells it was deemed not worth the minuscule extra computational time. While the computation does take longer than coupled or PISO could do, SIMPLE does converge for all cases of interest and thus it was used.

The easiest way to explain SIMPLE is it makes a guess at the pressure field, which then does not satisfy the continuity equation. Later, a correction factor is added back in to satisfy the continuity equation[3].

## A.7   Discretization

Discretization of space and time may be performed in a number of manners. There are a few more prolific schemes used. The first order upwind scheme is by far the simplest scheme. It is derived from the Taylor series approximation. The second order upwind scheme is a direct consequence of the desire to have more accuracy from the first order upwind scheme. In Fluent it is calculated using equation (A.8).

$$\phi_f = \phi + \nabla\phi \cdot \boldsymbol{r} \tag{A.8}$$

$\phi_f$ is the cell face value, where as $\phi$ is the cell centered value and $\boldsymbol{r}$, in this case, is the vector distance to the upstream cell center to the face[3]. This scheme is primarily used to discretize pressure.

The central - differencing scheme is effectively a phase shift of the second order upwind. In Fluent it is calculated using equation (A.9). The $\phi_0$ and $\phi_1$ are the cell centered values down and up stream respectively of the face, while $\boldsymbol{r}_0$ and $\boldsymbol{r}_1$ are the distances to the cell centered values from the face[3].

$$\phi_f = \frac{1}{2}\left(\phi_0 + \phi_1\right) + \frac{1}{2}\left(\nabla\phi_0 \cdot \boldsymbol{r}_0 + \nabla\phi_1 \cdot \boldsymbol{r}_1\right) \tag{A.9}$$

The last discretization scheme to be discussed is a combination of both the second order upwind scheme and the central differencing scheme. It is the third order monotone upstream centered scheme for conservation laws(MUSCL). The Ansys version is shown below in equation (A.10). $\phi_{central}$ is the equation for $\phi_f$ from the central differencing scheme, and similarly for $\phi_{second}$ is the $\phi_f$ from the second order upwind. $\theta$ is a blending argument, which is spatially based [3]. MUSCL is used for all other discretizations. These discretizations were chosen because they are the highest order accuracy available in the Fluent package.

$$\phi_f = \theta\phi_{central} + \left(1 - \theta\right)\phi_{second} \tag{A.10}$$

## A.8    Flow Models

Each of the flow classifications change which flow models should be used. The category compressible - incompressible determines whether one should use a pressure based formulation or a density based formulation of the flow models. The pressure based model is generally used for incompressible domains, while the density based solver is typically used for compressible flows. The pressure based solver calculates density from an equation of state, in this case, the ideal gas law. The flows discussed here are entirely assumed to be entirely incompressible, and thus the density based solver will not be discussed further.

The flow classification of laminar-turbulent flows determines whether to use the laminar solver or one of a variety of turbulent flow models. The laminar flow model is based upon basic flow equations, mass and momentum.

Multiple turbulence flow models have been developed, each having its own strengths and weaknesses. Therefore, when testing a new simulation, it is paramount to try many turbulence models and compare the simulated results against experimental results.

There are several flow models with this research utilizing primarily the Reynolds averaged Navier-Stokes (RANS) type. The RANS models assume the properties of the flow may be broken into a steady component and a transient component, such as velocity shown in equation (A.11). The models discussed are the Spalart-Allmaras, $k - \epsilon$, and $k - \omega$ models. The equations are solved using Ansys Fluent[2] and thus the equations here are the equations Fluent uses to solve each model.

$$u_i = \bar{u}_i + u_i' \tag{A.11}$$

The physics governing equations are simplified via the assumption of incompressible flow. This assumption may be shown to be accurate due to the near negligible Mach number. It is useful to note that the equations are not simplified to an incompressible fluid, which allows for density changes due to thermal effects, and therefore buoyancy effects.

Applying equation A.11 to the conservation of mass equation (equation A.12) results

in few changes (equation A.13).

$$\frac{\partial \rho}{\partial t} + \frac{\partial}{\partial x_i} (\rho u_i) = 0 \tag{A.12}$$

$$\frac{\partial \rho}{\partial t} + \frac{\partial}{\partial x_i} (\rho \bar{u}_i) = 0 \tag{A.13}$$

Application of Reynolds averaging to the conservation of momentum equation, equation A.14 is before A.15 and is after. Equation (A.15) is generally referred as the *Reynolds averaged Navier-Stokes equation* (RANS).

$$\frac{\partial}{\partial t} (\rho u_i) + \frac{\partial}{\partial x_j} (\rho u_i u_j) = -\frac{\partial P}{\partial x_i} + \frac{\partial}{\partial x_j} \left[ \mu \left( 2S_{ij} - \frac{2}{3} \delta_{ij} \frac{\partial u_k}{\partial x_k} \right) \right] \tag{A.14}$$

$$\frac{\partial}{\partial t} (\rho \bar{u}_i) + \frac{\partial}{\partial x_j} (\rho \bar{u}_i \bar{u}_j) = -\frac{\partial \bar{P}}{\partial x_i} + \frac{\partial}{\partial x_j} \left[ \mu \left( 2\bar{S}_{ij} - \frac{2}{3} \delta_{ij} \frac{\partial \bar{u}_k}{\partial x_k} \right) - \rho \overline{u_i' u_j'} \right] \tag{A.15}$$

$S_{ij}$ is the strain rate tensor and is defined by equation (A.16). $\delta_{ij}$ is the Kronecker delta function.

$$S_{ij} = \frac{1}{2} \left( \frac{\partial u_i}{\partial x_j} + \frac{\partial u_j}{\partial x_i} \right) \tag{A.16}$$

Similarly, for the conservation of energy equation, equation A.17 is before and A.18 is after.

$$\frac{\partial}{\partial t} (\rho E) + \frac{\partial}{\partial x_i} [u_i (\rho E + P)] = \frac{\partial}{\partial x_i} \left[ \left( \lambda + \frac{C_p \mu_t}{P_{rt}} \right) \frac{\partial T}{\partial x_i} \right] \tag{A.17}$$

$$\frac{\partial}{\partial t} (\rho \bar{E}) + \frac{\partial}{\partial x_i} [\bar{u}_i (\rho \bar{E} + \bar{P})] = \frac{\partial}{\partial x_i} \left[ \left( \lambda + \frac{C_p \mu_t}{P_{rt}} \right) \frac{\partial \bar{T}}{\partial x_i} \right] \tag{A.18}$$

The only major change for each of these equations is the addition of the Reynolds stress tensor, $-\rho \overline{u_i' u_j'}$. The tensor is the cause of a multitude of difficulties when solving for turbulent flows. Determining these six terms have been denoted the "closure problem".

### A.8.1 Laminar Flow Model

The laminar flow model does not require any special handling of the turbulence because by definition there is no turbulence. Therefore, the laminar flow model solves the continuity and Navier-Stokes equations without modifications.

Laminar flow problems in Ansys Fluent solve the governing equations already discussed. The continuity equation is shown in equation (A.12). The momentum equation

is shown in equation (A.14). Lastly, the energy equation is shown in equation (A.17). The only slight modification is that the eddy viscosity is zero in the energy equation and thus, that term is neglected.

## A.8.2   Spalart-Allmaras 1-equation Model

The Spalart-Allmaras model is a relatively simple one-equation model. That is that the turbulence model only adds one more transport equation to the original set: mass, momentum, and energy. Being a RANS model, it uses the Reynolds averaged transport equations already discussed, equations (A.13), (A.15) and (A.18). Due to the original intent of solving aerodynamic flows and the simplicity of the model, it has difficulty solving general fluid problems. Spalart-Allmaras has a particular difficulty solving free shear flows and jet flows [3].

The transport equation added may be either based upon the kinetic energy or the eddy viscosity. Ansys Fluent utilizes the eddy viscosity version and therefore, that is the version to be described here[3].

$$\frac{\partial}{\partial t}\left(\rho\tilde{\nu}\right) + \frac{\partial}{\partial x_i}\left(\rho\tilde{\nu}u_i\right) = G_\nu + \frac{1}{\sigma_{\tilde{\nu}}}\left[\frac{\partial}{\partial x_j}\left\{\left(\mu + \rho\tilde{\nu}\right)\frac{\partial\tilde{\nu}}{\partial x_j}\right\} + C_{b2\rho}\left(\frac{\partial\tilde{\nu}}{\partial x_j}\right)^2\right] - Y_\nu \quad \text{(A.19)}$$

The Reynolds stress is:

$$\overline{u_i'u_j'} = \mu_t S_{ij} \tag{A.20}$$

The eddy viscosity $\mu_t$ is calculated via equation (A.21) [3].

$$\mu_t = \rho\tilde{\nu}f_{\nu 1} \tag{A.21a}$$

$$f_{\nu 1} = \frac{\chi^3}{\chi^3 + C_{\nu 1}^3} \tag{A.21b}$$

$$\chi = \frac{\tilde{\nu}}{\nu} \tag{A.21c}$$

The turbulent production term in the transport equation is $G_\nu$ and the turbulent destruction term is $Y_\nu$. The former of which is detailed in equation (A.22), and the

latter in equation (A.23) [3].

$$G_\nu = C_{b1}\rho\tilde{S}\tilde{\nu} \tag{A.22a}$$

$$\tilde{S} = S + \frac{\tilde{\nu}}{\kappa^2 d^2}f_{\nu 2} \tag{A.22b}$$

$$f_{\nu 2} = 1 - \frac{\chi}{1 + \chi f_{\nu 1}} \tag{A.22c}$$

$$S = \sqrt{2\Omega_{ij}\Omega_{ij}} \tag{A.22d}$$

$$\Omega_{ij} = \frac{1}{2}\left(\frac{\partial u_i}{\partial x_j} - \frac{\partial u_j}{\partial x_i}\right) \tag{A.22e}$$

$$\tag{A.22f}$$

$$Y_\nu = C_{w1}\rho f_w\left(\frac{\tilde{\nu}}{d}\right)^2 \tag{A.23a}$$

$$f_w = g\left[\frac{1 + C_{w3}^6}{g^6 + C_{w3}^6}\right]^{1/6} \tag{A.23b}$$

$$g = r + C_{w2}\left(r^6 - r\right) \tag{A.23c}$$

$$r = \frac{\tilde{\nu}}{\tilde{S}\kappa^2 d^2} \tag{A.23d}$$

There are several model constants yet to be defined, equation (A.24) [3].

$$C_{b1} = 0.1355, C_{b2} = 0.622, \sigma_{\tilde{\nu}} = \frac{2}{3}, C_{\nu 1} = 7.1, \kappa = 0.4187 \tag{A.24a}$$

$$C_{w1} = \frac{C_{b1}}{\kappa^2} + \frac{(1 + C_{b2})}{\sigma_{\tilde{\nu}}}, C_{w2} = 0.3, C_{w3} = 2.0 \tag{A.24b}$$

### A.8.3 $K - \epsilon$ 2-equation model

The $k - \epsilon$ model is the first of two, two equation models used. The two equation model adds two new transport equations needing to be solved. The mass, momentum and energy equations are the same from the previous model, equations (A.13), (A.15) and (A.18). The two transport equations solve for the turbulent kinetic energy $k$ and the turbulence dissipation rate $\epsilon$, described in equation (A.25) and equation (A.26) respectively. Equation (A.27) is the Reynolds stress equation.

$$\frac{\partial}{\partial t}(\rho k) + \frac{\partial}{\partial x_j}(\rho k u_j) =$$

$$\frac{\partial}{\partial x_j}\left[\left(\mu + \frac{\mu_t}{\sigma_k}\right)\frac{\partial k}{\partial x_j}\right] + \frac{\partial u_j}{\partial x_i}\left(-\rho\overline{u_i' u_j'}\right) \tag{A.25}$$

$$- g_i \frac{\mu_t}{\rho P_{rt}}\frac{\partial \rho}{\partial x_i} + \rho\epsilon$$

$$\frac{\partial}{\partial t}(\rho\epsilon) + \frac{\partial}{\partial x_j}(\rho\epsilon u_j) =$$

$$\frac{\partial}{\partial x_j}\left[\left(\mu + \frac{\mu_t}{\sigma_\epsilon}\right)\frac{\partial \epsilon}{\partial x_j}\right] + \rho C_1 S\epsilon - \rho C_2 \frac{\epsilon^2}{k + \sqrt{\nu\epsilon}} \tag{A.26}$$

$$- C_{1\epsilon}\frac{\epsilon}{k}C_{3\epsilon}g_i\frac{\mu_t}{\rho P_{rt}}\frac{\partial \rho}{\partial x_i}$$

$$- \rho\overline{u_i' u_j'} = 2\mu_t S_{ij} - \frac{2}{3}\delta_{ij}\left(\rho k + \mu_t \frac{\partial u_k}{\partial x_k}\right) \tag{A.27}$$

The constants for this turbulence model are [18] :

$$C_{1\epsilon} = 1.44, C_2 = 1.9, \sigma_k = 1.0, \sigma_\epsilon = 1.2, P_{rt} = 0.85 \tag{A.28}$$

The coefficients of the model are [3]:

$$C_1 = max\left[0.43, \frac{Sk/\epsilon}{Sk/\epsilon + 5}\right], S = \sqrt{2S_{ij}S_{ji}}, C_{3\epsilon} = tanh\left(\frac{u_g}{u_p}\right) \tag{A.29}$$

Where $u_g$ is the velocity component parallel to gravity, while $u_p$ is the velocity perpendicular to gravity.

The realizable $k-\epsilon$ model varies from the traditional model by using a non-constant coefficient $C_\mu$ of the eddy viscosity equation $\mu_t$. Which is defined as follows [3, 18]

$$\mu_t = \frac{\rho C_\mu k^2}{\epsilon} \tag{A.30a}$$

$$C_\mu = \frac{1}{A_0 + \frac{A_1 k U^*}{\epsilon}} \tag{A.30b}$$

$$U^* \equiv \sqrt{S_{ij}S_{ji} + \Omega_{ij}\Omega_{ji}} \tag{A.30c}$$

$$A_0 = 4.04 \tag{A.30d}$$

$$A_1 = \sqrt{6}cos\left[\frac{1}{3}cos^{-1}\left(\sqrt{6}\frac{S_{ij}S_{jk}S_{ki}}{(S_{ij}S_{ji})^{\frac{3}{2}}}\right)\right] \tag{A.30e}$$

$$S_{ij} = \frac{1}{2}\left(\frac{\partial u_i}{\partial x_j} + \frac{\partial u_j}{\partial x_i}\right) \tag{A.30f}$$

$$\Omega_{ij} = \frac{1}{2}\left(\frac{\partial u_i}{\partial x_j} - \frac{\partial u_j}{\partial x_i}\right) \tag{A.30g}$$

### A.8.4  $K - \omega$ **2-equation model**

The $k - \omega$ model is similar to the $k - \epsilon$ model. The two new transport equations are the turbulent kinetic energy and specific dissipation rate. Those transport equations are equation (A.31) and equation (A.32).

$$\frac{\partial}{\partial t}(\rho k) + \frac{\partial}{\partial x_j}(\rho k u_j) =$$
$$\frac{\partial}{\partial x_j}\left[\left(\mu + \frac{\mu_t}{\sigma_k}\right)\frac{\partial k}{\partial x_j}\right] + \frac{\partial u_j}{\partial x_i}\left(-\rho\overline{u_i' u_j'}\right) - Y_k \tag{A.31}$$

$$\frac{\partial}{\partial t}(\rho \omega) + \frac{\partial}{\partial x_j}(\rho \omega u_j) =$$
$$\frac{\partial}{\partial x_j}\left[\left(\mu + \frac{\mu_t}{\sigma_\omega}\right)\frac{\partial \omega}{\partial x_j}\right] + \alpha\frac{\omega}{k}\frac{\partial u_j}{\partial x_i}\left(-\rho\overline{u_i' u_j'}\right) - Y_\omega \tag{A.32}$$

The eddy viscosity is calculated by equation (A.33).

$$\mu_t = \alpha^* \frac{\rho k}{\omega} \tag{A.33a}$$

$$\alpha^* = \alpha_\infty^* \left(\frac{\alpha_0^* + Re_t/R_k}{1 + Re_t/Rk}\right) \tag{A.33b}$$

$$Re_t = \frac{\rho k}{\mu\omega} \tag{A.33c}$$

$$\alpha_0^* = \frac{\beta_i}{3} \tag{A.33d}$$

$$\alpha = \frac{\alpha_\infty}{\alpha^*}\left(\frac{\alpha_0 + Re_t/R_\omega}{1 + Re_t/R_\omega}\right) \tag{A.33e}$$

The dissipation of turbulent kinetic energy is $Y_k$ and is defined in equation (A.34), while the dissipation of $\omega$ is $Y_\omega$ and is defined in equation (A.35). It should be noted that these equations are for Mach numbers less than 0.25 [3].

$$Y_k = \rho\beta^* f_{\beta^*} k\omega \tag{A.34a}$$

$$f_{\beta^*} = \begin{cases} 1 & \text{if } \chi_k \leq 0 \\ \frac{1+680\chi_k^2}{1+400\chi_k^2} & \text{if } \chi_k > 0 \end{cases} \tag{A.34b}$$

$$\chi_k = \frac{1}{\omega^3}\frac{\partial k}{\partial x_j}\frac{\partial \omega}{\partial x_j} \tag{A.34c}$$

$$\beta^* = \beta_i^* \tag{A.34d}$$

$$\beta_i^* = \beta_\infty^*\left(\frac{4/15 + (Re_t/R_\beta)^4}{1 + (Re_t/R_\beta)^4}\right) \tag{A.34e}$$

$$Y_\omega = \rho \beta f_\beta \omega^2 \tag{A.35a}$$

$$f_\beta = \frac{1 + 70\chi_\omega}{1 + 80\chi_\omega} \tag{A.35b}$$

$$\chi_\omega = |\frac{\Omega_{ij}\Omega_{jk}S_{ki}}{(\beta_\infty^* \omega)^3}| \tag{A.35c}$$

$$\Omega_{ij} = \frac{1}{2}\left(\frac{\partial u_i}{\partial x_j} - \frac{\partial u_j}{\partial x_i}\right) \tag{A.35d}$$

$$\tag{A.35e}$$

Lastly, there are several model constants needing to be set

$$\alpha_\infty^* = 1, \alpha_\infty = 0.52, \alpha_0 = \frac{1}{9}, \beta_\infty^* = 0.09, \beta_i = 0.072, R_\beta = 8 \tag{A.36a}$$

$$R_k = 6, R_\omega = 2.95, \xi^* = 1.5, \sigma_k = 2.0, \sigma_\omega = 2.0 \tag{A.36b}$$

# Appendix B

# Calibration

Equipment calibration is essential to acquiring proper results from scientific studies. Calibration tests were performed on the thermocouples(K-type), motion controller and the hot-wire anemometer. The pressure transducer (Omega model PX653-0.1D5V) was factory calibrated and checked against a U-tube manometer.

## B.1 Thermocouple

The thermocouples were individually checked against the freezing and boiling points of distilled water. Only two points are needed, as K-type thermocouples (the only type used) have a linear voltage response in the temperature range of interest. Since the voltage response is linear, the calibration is also linear and may be applied after another linear response. A table of all the thermocouple calibration parameters used throughout the experiments is shown in table B.1. The table shows the reading of the thermocouples when tested in a $0 \deg C$ and $100 \deg C$ environment. The data is used to convert measured temperature into actual temperature using equation (B.1).

$$T_{Actual} = \frac{-100}{T_0 - T_{100}} T_{Measured} + \frac{100}{T_0 - T_{100}} T_0 \tag{B.1}$$

## B.2 Motion Controller

The axial and perpendicular motion controllers send signals to stepper motors. If $1\,mm$ motion is asked of the motion controller, it needs to know how many steps is required to move that amount. It turns out that for the axial direction, it is 202.4 steps/mm, and for the perpendicular direction, it is 155.6 steps/mm.

These numbers were determined via a Mitutoyo certified 6 inch caliper mounted

| Thermocouple | $0 \deg C$ | $100 \deg C$ |
| --- | --- | --- |
| Probe | 3.26 | 100.9 |
| Ambient | 1.66 | 99.8 |
| Plume heater 1 | -0.05 | 99.8 |
| Plume heater 2 | 1.88 | 99.8 |
| Jet | 1.70 | 99.9 |
| Jet air pre-heat | 2.19 | 99.9 |
| Jet air heater | 1.30 | 99.8 |
| Cavity heater | 1.73 | 100.2 |

Table B.1: Thermocouple calibration

against each stage to determine how much motion occurs for each step and series of steps. The caliper is accurate to $50\,\mu m$ and thus, motion of each linear stage is also accurate to $50\,\mu m$ since the step size is approximately an order of magnitude smaller than the accuracy of the calibration.

Unfortunately, the linear stages suffer from backlash even with backlash eliminating feed nuts. Therefore, motion for both stages followed strict backlash compensation procedures (i.e. approach locations from one and only one direction). The backlash is approximately $1.3\,mm$ and $0.8\,mm$ for axial and perpendicular directions respectively.

## B.3   Hot-wire Anemometer

The hot-wire anemometer was calibrated against a Pitot-static tube connected to the aforementioned pressure transducer. The procedure is simple and entails sampling several velocities and checking the resultant voltage. A fourth order least squares curve fit is then used to convert voltage to velocity, equation (B.2). A plot of the calibrations and curve fit are shown in figure B.1.

$$U = -26.78V^4 + 210.89V^3 - 597.91V^2 + 736.74V - 335.92 \qquad \text{(B.2)}$$

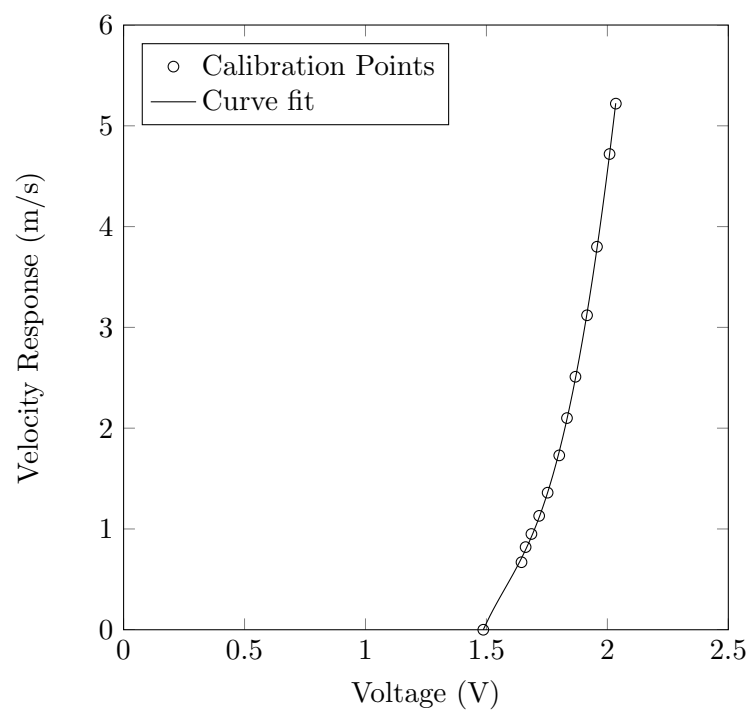| Velocity ($m/s$) | Voltage ($V$) |
|---:|:---|
| 0 | 1.487 |
| 0.67 | 1.645 |
| 0.82 | 1.662 |
| 0.95 | 1.686 |
| 1.13 | 1.718 |
| 1.36 | 1.753 |
| 1.73 | 1.801 |
| 2.10 | 1.833 |
| 2.51 | 1.868 |
| 3.12 | 1.916 |
| 3.80 | 1.957 |
| 4.72 | 2.009 |
| 5.22 | 2.035 |

Table B.2: Hot-wire anemometer calibration



Figure B.1: Hot-wire calibration curve

# Appendix C

# Data Acquisition

Data acquisition is a significant portion of the experimental apparatus. A significant number of experimental parameters were recorded. Some of the typical parameters are listed in table C.1. Parameters listed as "constant" are kept as constant as practical. However, some variation occurs, especially throughout the course of a day.

| Experimental Parameter | |
|---|---|
| $T_\infty$ | constant |
| $U_\infty$ | constant |
| $T_S$ | constant |
| $T_{jet}$ | constant |
| $U_{jet}$ | constant |
| $T\left(\boldsymbol{r}\right)$ | time varying |
| $U\left(\boldsymbol{r}\right)$ | time varying |
| $r_{axial}$ | synchronized variation |
| $r_{perp}$ | synchronized variation |

Table C.1: Recorded experimental parameters

## C.1   Hardware

Any experimental parameter requiring time varied sampling cannot have sampling limitations and thus, will be acquired using a high speed data acquisition device. Unfortunately, this hardware has limits to how many samples it can record simultaneously

and therefore, a multiplexed data acquisition device is used to sample the relatively constant parameters. Lastly, to move the sampling probe in the domain, a motion controller is required. These devices are all add-on electronic cards for a modern computer. A diagram of the hardware configuration is shown in figure C.1
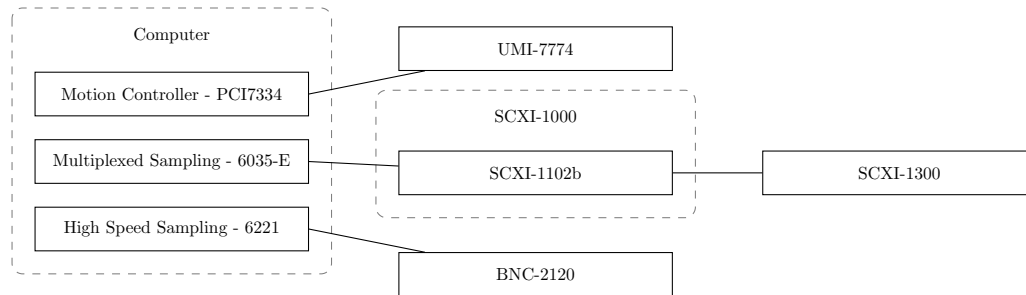


Figure C.1: Diagram of hardware configuration

### C.1.1    High Speed Data Acquisition

The high speed data acquisition is handled using a National Instruments add-on card, model 6221, connected to a breakout board, model BNC-2120. This card is capable of recording at 250,000 samples per second at 16-bit and 16 simultaneous channels. The breakout board, BNC-2120, only has one thermocouple input, and therefore, only one thermocouple will be recorded at high speed. That would be the local static temperature probe. Since the hotwire-anemometer does not need the thermocouple input and is not used simultaneously with the temperature probe, it is also connected to the high speed device. The actual sample rate was set at 20kHz. The rate is fast enough to perform a frequency analysis, which ultimately proved fruitless. The rate is slow enough to keep total data at a reasonable level (total experiment recorded information totaled over 50GB). For reference the response time of the thermocouple is approximately $0.04\,s$ according to [1].

### C.1.2    Multiplexed Data Acquisition

The bulk of all of the sampling is done through a 32-channel multiplexer. The device is a National Instruments add-on card, model 6035-E, capable of 200,000 samples per

second at 16-bit connected to a SCXI-1000 low noise signal chassis. Inside the SCXI-1000 chassis is a single SCXI-1102b 32-channel multiplexer, with a 2Hz low pass filter. Lastly, a SCXI-1300 breakout board is connected to the SCXI-1102b. Just prior to each high speed acquisition, 10 samples were recorded at 2Hz of the relatively constant data. These samples were averaged later to get more accurate experimental conditions for each high speed acquisition.

### C.1.3    Motion Controller

The local static thermocouple probe is traversed across the domain using a two axis stepper motor stage. The stepper motors are controlled via a National Instruments pci7334 connected to a UMI-7774 breakout board. The stepper motors, in combination of the linear slides, are capable of moving in increments as small as $50\mu m$ for both axial and perpendicular directions.

### C.2    Software

The hardware was controlled via National Instruments Labview software[22]. A special labview program was written to accomplish all data acquisition and motion control. The program was designed to sample an entire plane of the domain at specific sample points without user interaction. The user interface to the program is displayed in figure C.2. Labview programmed in what National Instruments calls block diagrams, and the block diagram for this program is shown in figure C.3. Labview block diagrams have sub-blocks (labeled "BOX A", "BOX B"), each having their own figure. Box A is a true-false box where the true case is shown in figure C.3, while the false case is shown in figure C.4. Box B is a switch box where many numbered cases are possible, the '0' case is shown in figure C.3. The subsequent numbered cases 1-3 are shown in figures C.5 to C.7. Figure C.7 also contains a true-false box. The true case is shown in figure C.8. Similarly, Box C is a switch box and cases 1-4 are shown in figures C.9 to C.12. Figure C.12 has a true-false box and its true case is in figure C.13. There are several alternative cases not shown here, such as 'Box B case 4' or 'Box D case

false' these alternative cases do nothing and are left blank, and thus have nothing to contribute.
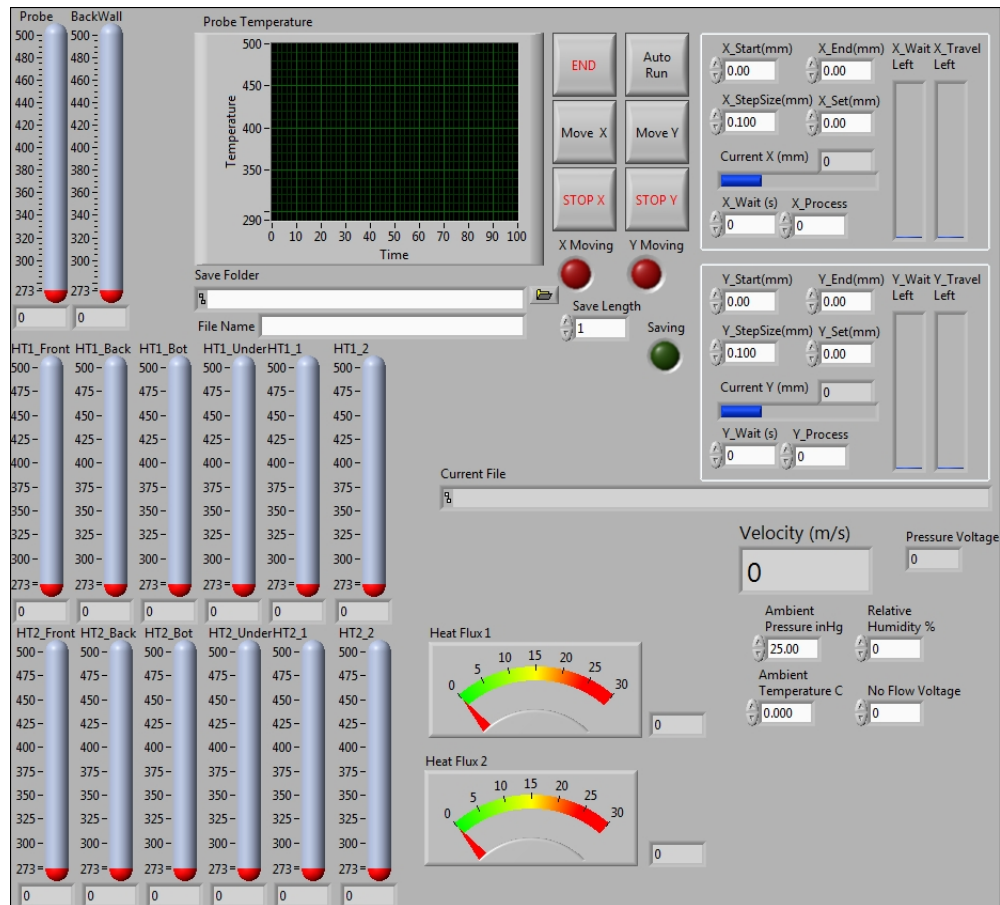


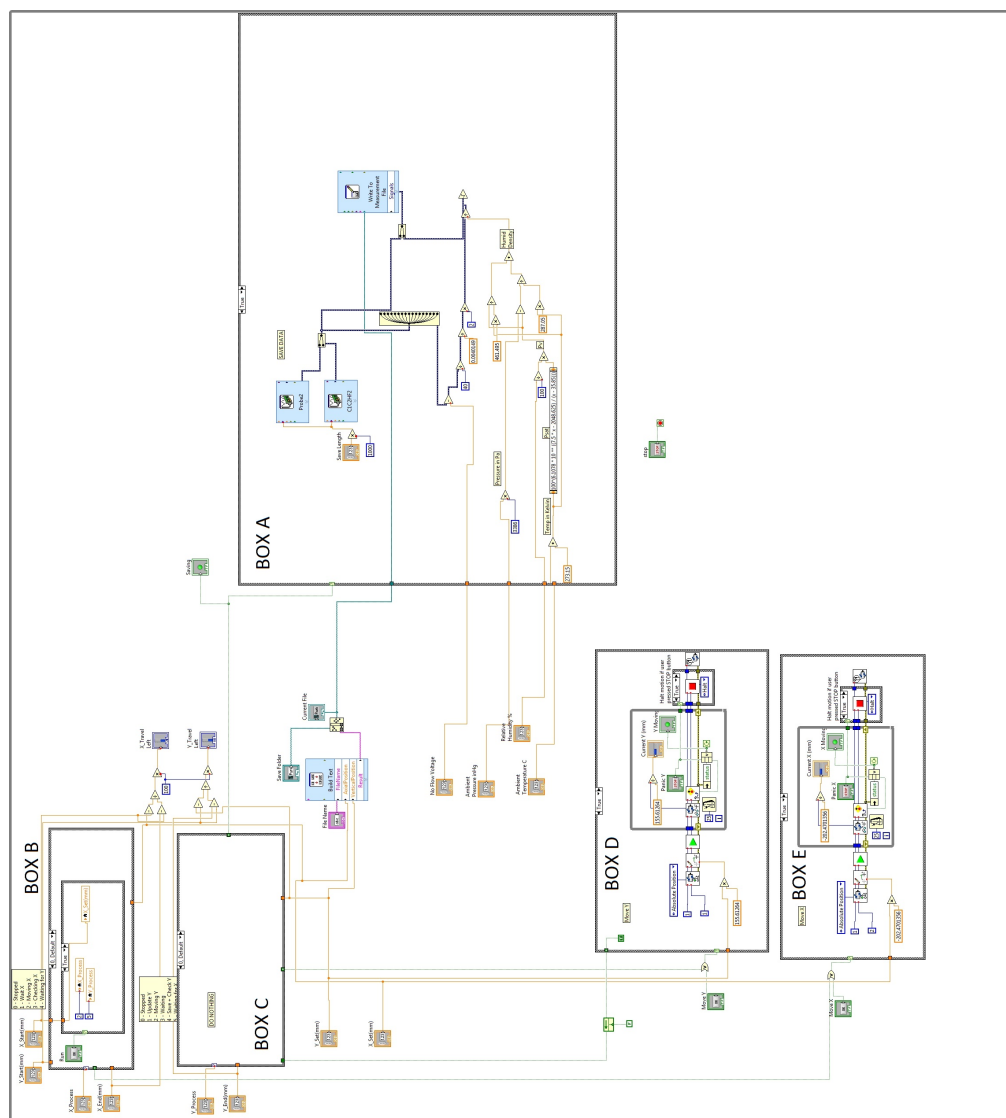Figure C.2: Labview program user interface
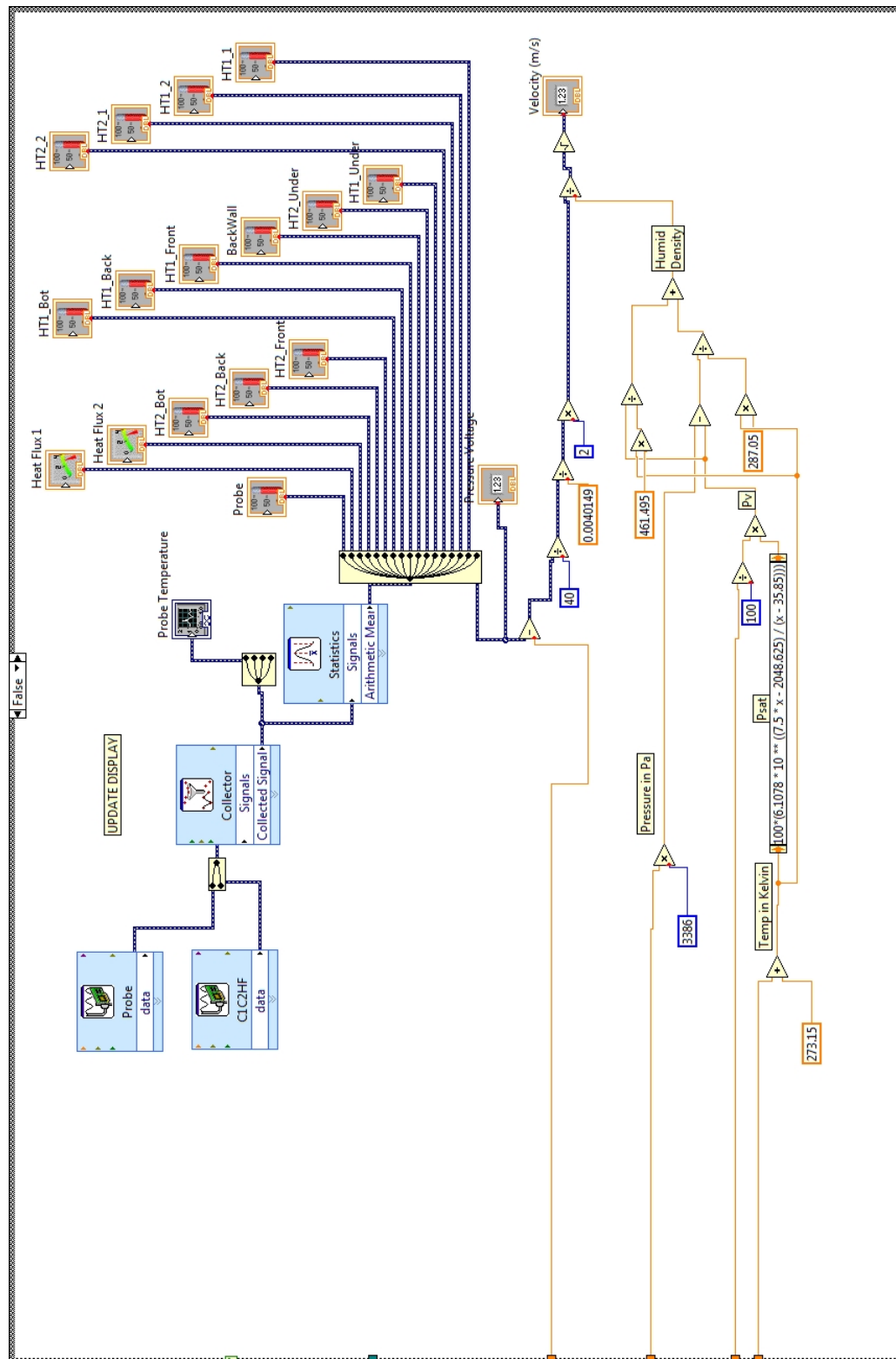
Figure C.3: Labview program block diagram

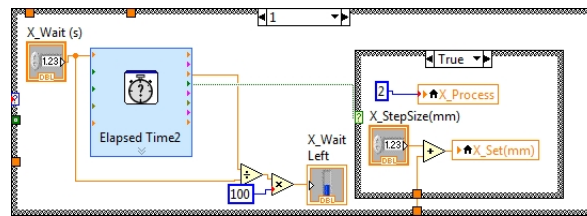Figure C.4: Labview program block diagram - box A - false

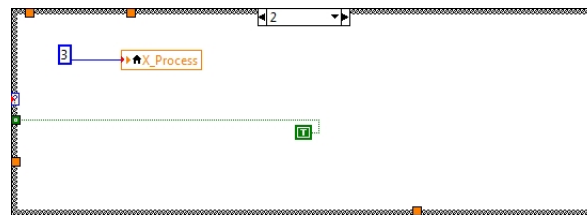Figure C.5: Labview program block diagram - box B - 1



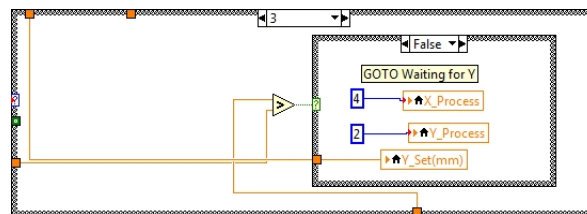Figure C.6: Labview program block diagram - box B - 2



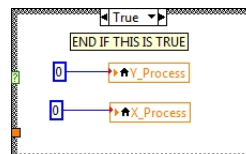Figure C.7: Labview program block diagram - box B - 3



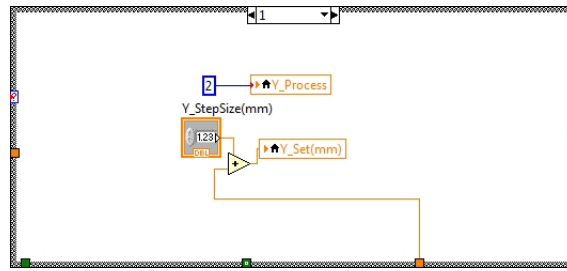Figure C.8: Labview program block diagram - box B - 3 true

Figure C.9: Labview program block diagram - box C - 1
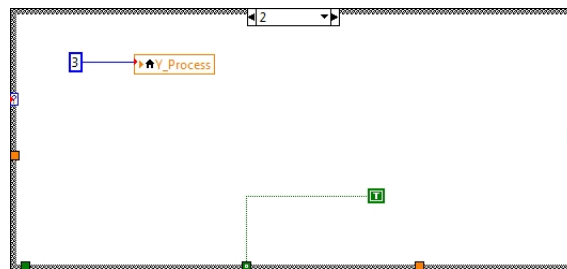


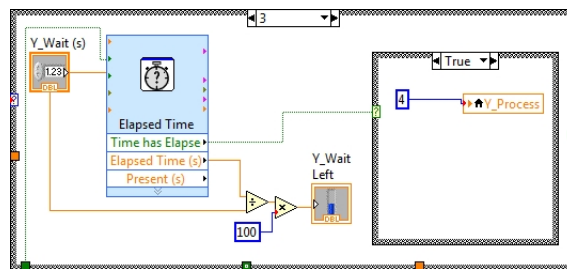Figure C.10: Labview program block diagram - box C - 2
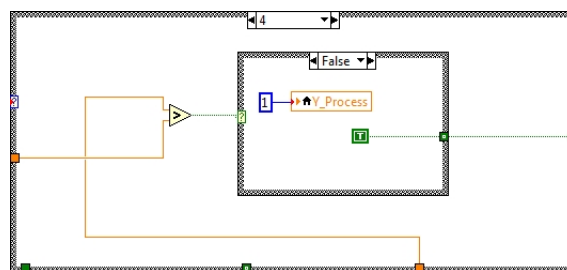


Figure C.11: Labview program block diagram - box C - 3



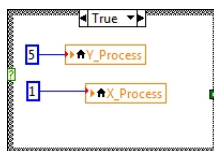Figure C.12: Labview program block diagram - box C - 4

Figure C.13: Labview program block diagram - box C - 4 true

# Appendix D

# Matlab Software

The Mathworks Matlab[32] software was used extensively in all aspects of the solution methodology. Collating of experimental and numerical data, methodology, optimization, analysis, and reporting were all performed using Matlab.

## D.1 Genetic Algorithm

The Mathworks Matlab[32] global optimization toolbox is used in both the inverse methodology and optimization of the search shape. The toolbox contains a plethora of methods for solving for global minimums. One such example is the genetic algorithm, which is used here. The genetic algorithm, or GA, was specifically developed to have significant robustness. That is to say that the method is designed to solve a wide range of problems with a complex mixture of constraints. GA was not developed overnight from one grand paper, but was started from several papers by Barricelli in the mid 1950's through mid 1960's. This culminated with what is widely accepted as the first document on what we now call the genetic algorithm, a book by Holland [16].

The GA is fundamentally bio-mimetic method, which loosely follows evolution. Many possible sets of design variables or chromosomes are evaluated, and the best chromosomes are selected to mate and create the next generation of chromosomes. This process is repeated until no further "best" solution is found[35].

Matlab's version of the GA follows six steps: creation, fitness scaling, selection, crossover, and mutation. Creation is the initialization step, the creation of the "species" if you will. Fitness scaling is the way each chromosome is fairly scored against the other chromosomes, without one group dominating the population. Selection is the method in which parents are selected, often partially stochastic. Crossover is the GA's terminology

for mating; chromosomes are paired and design parameters are swapped in an attempt to make a better chromosome. The mutation step adds a bit of randomness to the chromosome pool to reduce design parameter stagnation. For more details about the Matlab GA or GA in general refer to either [31] or [35].

There are many parameters available to the Matlab GA function, of which the most important for this work is displayed in table D.1.

| Parameter | Meaning | default |
|---|---|---|
| population size | no. of chromosomes in pool | no. of parameters |
| generations | maximum no. of generations before a forced exit | 100 |
| tolerance | smallest difference between chromosome rankings considered unique | $10^{-6}$ when ranking is normalized to 1 |
| stall limit | number of generations to proceed with no changes in the best unique solution | none |
| number of elites | number of chromosomes kept between iterations | 2 |
| crossover fraction | percentage of population used in the next generation | 0.8 |
| creation method | how the initial chromosome population is generated | Gaussian |
| fitness method | method on ranking of chromosomes | top 40% |
| selection method | method on selecting mating pairs of chromosomes | stochastic |
| crossover method | method for making new new chromosomes | intermediate |
| mutation method | how mutations occur during the mating process | Gaussian |
| hybrid function | an option to switch to a traditional linear solver | none |
| parallel | utilizes all parallel resources available | never |

Table D.1: Genetic algorithm parameters[31]

# Appendix E

# Sampled Data

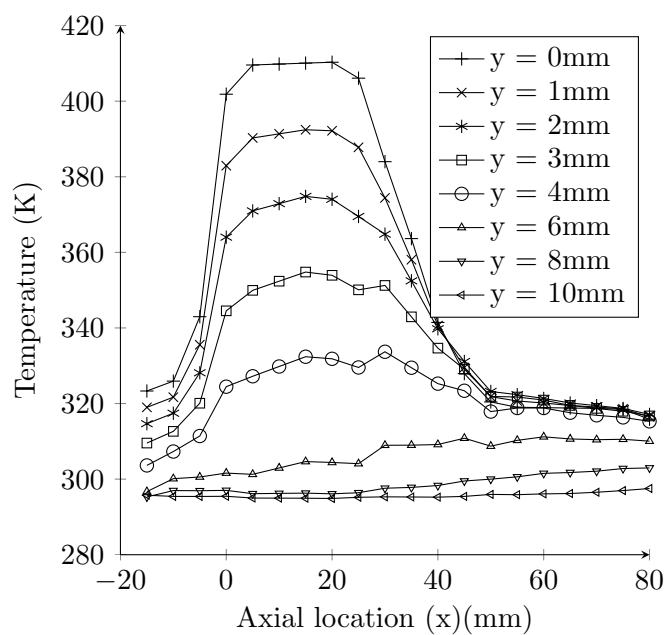The following is plots of the experimental plume data.



Figure E.1: Experimental Data $U_\infty = 0.4\,m/s$, $T_S = 410K$

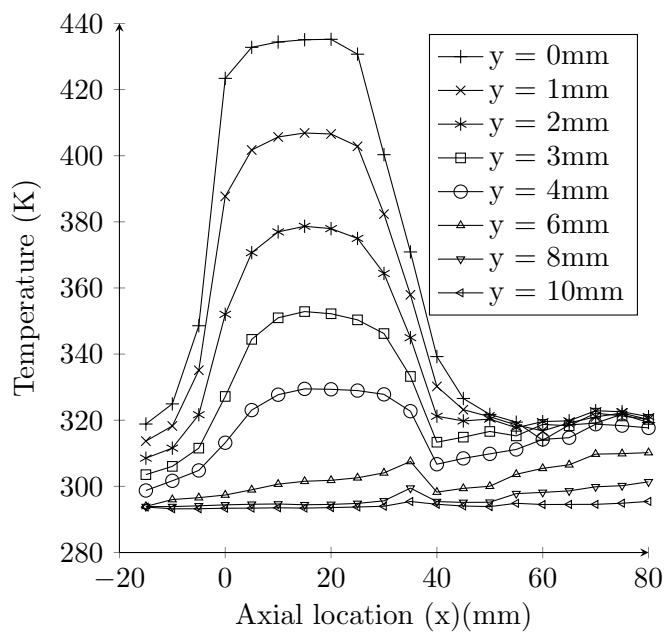Figure E.2: Experimental Data $U_\infty = 0.4\,m/s$, $T_S = 435K$

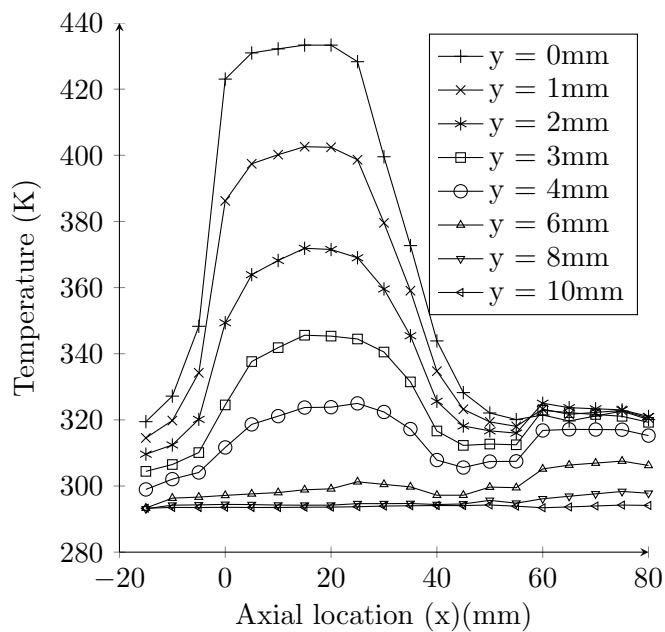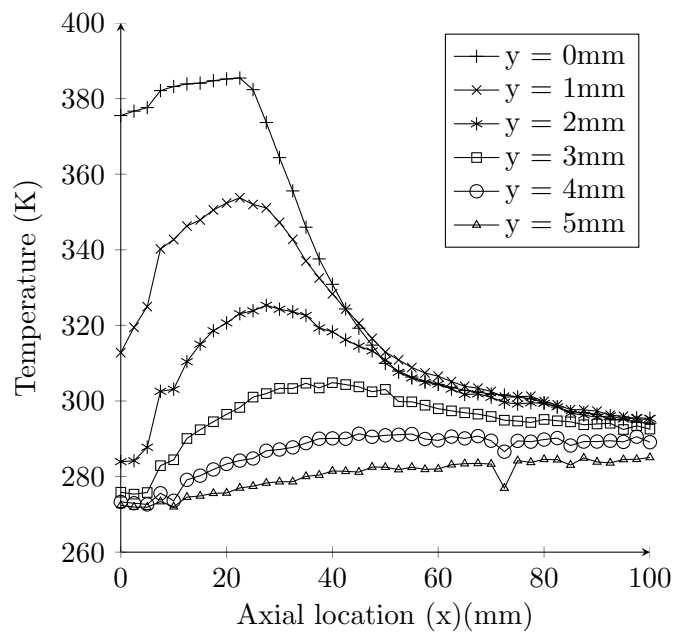

Figure E.3: Experimental Data $U_\infty = 0.5\,m/s$, $T_S = 435K$

Figure E.4: Experimental Data $U_\infty = 0.6\,m/s$, $T_S = 446K$
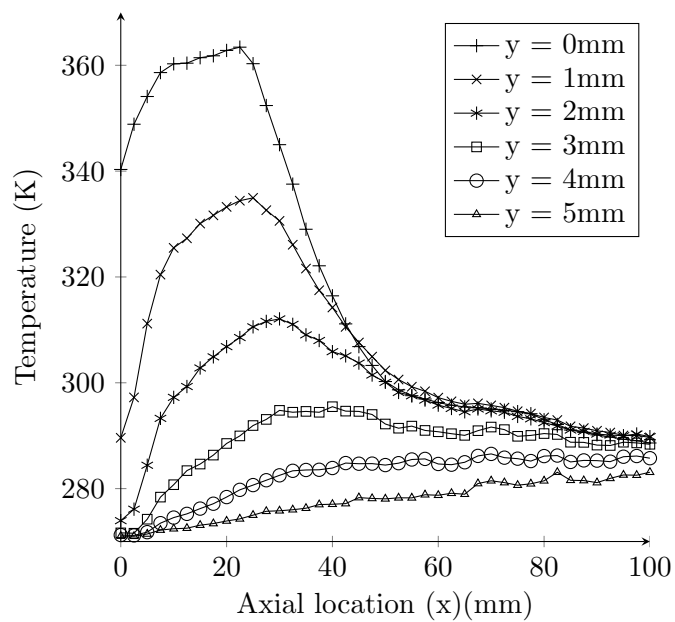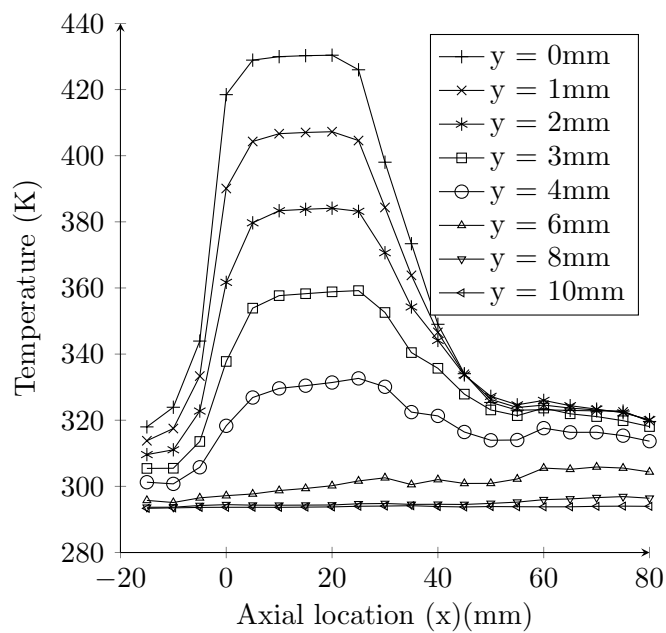


Figure E.5: Experimental Data $U_\infty = 0.6\,m/s$, $T_S = 410K$
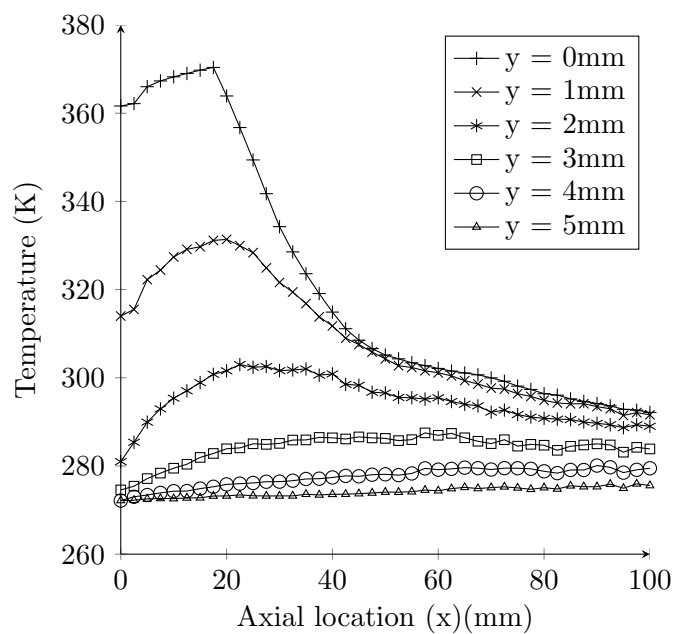
Figure E.6: Experimental Data $U_\infty = 0.7\,m/s$, $T_S = 430K$



Figure E.7: Experimental Data $U_\infty = 1.0\,m/s$, $T_S = 446K$
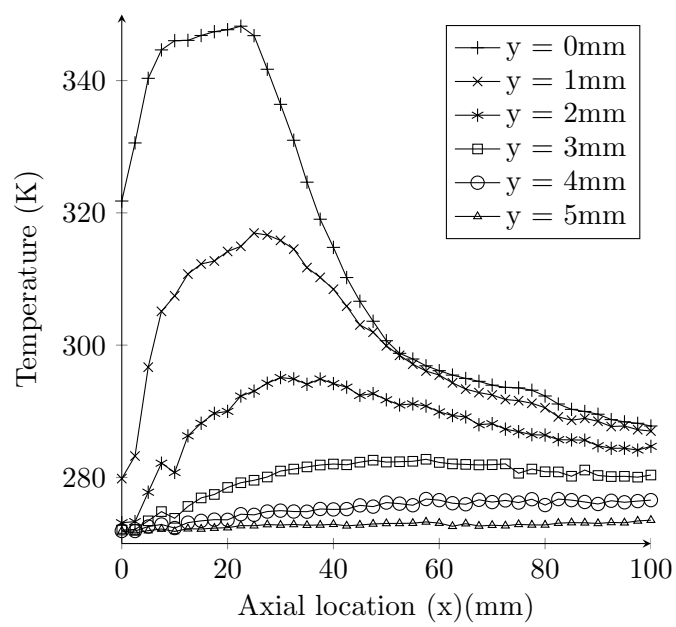
Figure E.8: Experimental Data $U_\infty = 1.0\,m/s$, $T_S = 410K$

# Bibliography

[1] Thermocouple technical reference. Technical report, Omega, 2000.

[2] Ansys. Fluent (version 13), 2010.

[3] Ansys. Fluent technical documents v14.0. Technical report, Ansys, 2011.

[4] J. Beck, B. Blackwell, and A. Haji-Sheikh. Comparison of some inverse heat conduction methods using experimental data. *International Journal of Heat Mass Transfer*, vol 39:3649–3657, 1996.

[5] P. S. Bernard and J. M. Wallace. *Turbulent Flow: Analysis, Measurement, and Predicition.* John Wiley and Sons, Inc, Hoboken, NJ, 2002. ISBN 0-471-33219-4.

[6] E. Blanchard, P. Boulet, S. Desanghere, E. Cesmat, R. Meyrand, J. Garo, and J. Vantelon. Experimental and numerical study of fire in a midscale test tunnel. *Fire Safety Journal*, vol 47:18–31, 2012.

[7] D. Contini and A. Robins. Experiments on the rise and mixing in neutral crossflow of plumes from two identical sources for different wind directions. *Atmospheric Environment*, vol 38:3573–3583, 2004.

[8] K. Daun and J. Howell. Inverse design methods for radiative transfer systems. *Journal of Quantitative Spectroscopy and Radiative Transfer*, vol 93:43–60, 2005.

[9] H. Erturk, O. A. Ezekoye, and J. R. Howell. Comparison of three regularized solution techniques in a three-dimensional inverse radiation problem. *Journal of Quantitative Spectroscopy and Radiative Transfer*, vol 73, 2002.

[10] H. Erturk, M. Gamba, O. A. Ezekoye, and J. R. Howell. Validation of inverse boundary condition design in a thermometry test bed. *Journal of Quantitative Spectroscopy and Radiative Transfer*, vol 109:317–326, 2008.

[11] R. Fox and A. McDonald. *Introduction to Fluid Mechanics 5th ed.* John Wiley and Sons, Inc, New York, NY, 1998. ISBN 0-471-12464-8.

[12] B. Gebhart, Y. Jaluria, R. Mahajan, and B. Sammakia. *Buoyancy-Induced Flows and Transport.* Hemisphere Publishing Corporation, New York, NY, 1988. ISBN 0-89116-402-2.

[13] S. Ghosh, D. Pratihar, B. Maiti, and P. Das. Inverse estimation of location of internal heat source in conduction. *Inverse Problems in Science and Engineering*, vol19:337–361, 2011.

[14] J. Hadamard. *Sur les problmes aux drives partielles et leur signification physique.* Princeton University Bulletin, 1902.

[15] M. R. Hestenes and E. Stiefel. Methods of conjugate gradients for solving linear systems. *Journal of Research of the National Bureau of Standards*, vol49:409–436, 1952.

[16] J. H. Holland. *Adaptation in Natural and Artificial Systems: an Introductory Analysis with Application to Biology, Control, and Artificial Intelligence.* University of Michigan Press, MI, 1975.

[17] Y. K. Hong, S. W. Baek, and M. Y. Kim. Inverse natural convection problem with radiation in rectangular enclosure. *Numerical Heat Transfer*, vol57:315–330, 2010.

[18] T. hsing Shih, W. Liou, A. Shabbir, Z. Yang, and J. Zhu. A new $k - \epsilon$ eddy viscosity model for high reynolds number turbulent flows. *Computer Fluids*, vol 24:227–238, 1995.

[19] L. H. Hu and D. Yang. Large eddy simulation of fire-induced buoyancy driven plume dispersion in an urban street canyon under perpendicular wind flow. *Journal of Hazardous Materials*, vol 166:394–406, 2009.

[20] T. Icoz and Y. Jaluria. Design of cooling systems for electronic equipment using both experimental and numerical inputs. *Journal of Electronic Packaging*, vol 126: 465–471, 2004.

[21] F. Incropera, D. Dewitt, T. Bergman, and A. Lavine. *Fundamentals of Heat and Mass Transfer 6th ed.* John Wiley and Sons, Inc, New York, NY, 2006. ISBN 0-471-45728-0.

[22] N. Instruments. Labview, 2012.

[23] J. Issa, Z. Yin, C. E. Polymeropoulos, and Y. Jaluria. Temperature distribution in an optical fiber draw tower furnace. *Journal of Materials Processing and Manufacturing Science*, vol 4:221–232, 1996.

[24] M. Jansons, S. Lin, and K. Rhee. Infrared spectral analysis of engine preflame emission. *International Journal of Engine Research*, vol 9:215–238, 2008.

[25] D. Knight, Q. Ma, T. Rossmann, and Y. Jaluria. Evaluation of fluid-thermal systems by dynamic data driven application systems - part ii. In *International Conference on Modeling and Optimization of Structures, Processes and Systems*, University of Kwazulu-Natal, South Africa, January 2007. Springer-Verlag.

[26] A. Kumar and C. Balaji. A principle component analysis and neural network based non-iterative method for inverse conjugate natural convection. *International Journal of Heat and Mass Transfer*, vol53:4684–4695, 2010.

[27] P. Kundu and I. Cohen. *Fluid Mechanics 3rd ed.* Elsevier Inc., New York, NY, 2004. ISBN 0-12-178253-0.

[28] D. Liu, F.-Y. Zhao, H.-Q. Wang, E. Rank, and G.-X. Kou. Inverse determination of building heating profiles from the knowledge of measurements within the turbulent slot-vented enclosure. *International Journal of Heat and Mass Transfer*, vol 55: 4597–4612, 2012.

[29] Q. Ma, Y. Luo, T. Rossmann, D. Knight, and Y. Jaluria. Diode laser measurements for dddas: Flowfield reconstruction using dynamic experimental and numerical data. In *25th AIAA Aerodynamic Measurement Technology and Ground Testing Conference*, San Francisco, CA, June 2006. American Institute of Aeronautics and Astronautics, Inc.

[30] R. A. Maronna, R. D. Martin, and V. J. Yohai. *Robust Statistics Theory and Methods*. John Wiley and Sons, Inc, Hoboken, NJ, 2006. ISBN 0-470-01092-4.

[31] Mathworks. Matlab 2013b documentation, 2013.

[32] Mathworks. Matlab 2013b, 2013.

[33] M. R. Mokhtarzadeh-Dehghan, C. S. Knig, and A. G. Robins. Numerical study of single and two interacting turbulent plumes in atmospheric cross flow. *Atmospheric Environment*, vol 40:3909–3923, 2006.

[34] A. Mossi, H. Vielmo, F. Franca, and J. Howell. Inverse design involving combined radiative and turbulent convective heat transfer. *International Journal of Heat and Mass Transfer*, vol 51:3217–3226, 2008.

[35] C. Onwubiko. *Introduction to Engineering Design Optimization*. Prentice Hall, Inc, Upper Saddle River, NJ, 2000. ISBN 978-0201476736.

[36] H. R. Orlande, O. Fudym, D. Maillet, and R. M. Cotta. *Thermal Measurements and Inverse Techniques*. Taylor and Francis Group, CRC Press, Boca Raton, Fl, 2011. ISBN 978-1-4398-4555-4.

[37] M. N. Ozisik and H. R. Orlande. *Inverse Heat Transfer: Fundamentals and Applications*. Taylor and Francis Group, CRC Press, New York, NY, 2000. ISBN 1-56032-838-X.

[38] H. Park and O. Chung. An inverse natural convection problem of estimating the strength of a heat source. *International Journal of Heat and Mass Transfer*, vol42: 4259–4273, 1999.

[39] A. P. Sasmitoa, E. Birgerssona, and A. S. Mujumdara. Numerical evaluation of various thermal management strategies for polymer electrolyte fuel cell stacks. *International Journal of Hydrogen Energy*, 36:12991–13007, 2011.

[40] J. Schluter and T. Schonfeld. Les of jets in cross flow and its application to a gas turbine burner. *Flow, Turbulence, and Combustion*, 65:177–203, 2000.

[41] A. N. Tikhonov and V. Y. Arsenin. *Solutions of Ill-Posed Problems*. V.H. Winston and Sons, Washington, D.C., 1977. ISBN 0-470-99124-0.

[42] A. N. Tikhonov, A. Goncharsky, V. Stepanov, and A. Yagola. *Numerical Methods for the Solution of Ill-Posed Problems*. Kluwer Academic Publishers, Boston, Ma, 1995. ISBN 0-7923-3583-X.

[43] J. VanderVeer and Y. Jaluria. Hybrid experimental-numerical approach to solve inverse convection problems. In *Proceedings of Computational Heat Transfer-2012, International Symposium on Advances in Computational Heat Transfer*, Middle East Technical University, Ankara, Turkey, July 2012. International Center for Heat and Mass Transfer.

[44] J. VanderVeer and Y. Jaluria. Solution of an inverse convection problem by a predictor-corrector approach. *International Journal of Heat and Mass Transfer*, vol65:123–130, 2013.

[45] J. VanderVeer and Y. Jaluria. Optimization of an inverse convection solutions strategy. *International Journal of Heat and Mass Transfer*, 73:664–670, 2014.

[46] W. G. Vincenti and C. H. Kruger. *Introduction to Physical Gas Dynamics*. Krieger Publishing Company, Malabar, Fl, 2002. ISBN 0-88275-309-6.

[47] D. C. Wilcox. *Turbulence Modeling for CFD*. DCW Industries, Inc, La Canada, CA, 1994.

[48] Z. Zhang. Parameter estimation techniques: A tutorial with application to conic fitting. *Image and Vision Computing*, vol15:59–76, 1997.

[49] F.-Y. Zhao, D. Liu, L. Tang, Y.-L. Ding, and G.-F. Tang. Direct and inverse mixed convections in an enclosure with ventilation ports. *International Journal of Heat and Mass Transfer*, vol52:4400–4412, 2009.